UNIVERSITY OF CALIFORNIA

Santa Barbara

Characterizing the relationships between micro- and nano-scale structure and the interfacial and mechanical properties of biological and bio-inspired materials

A dissertation submitted in partial satisfaction of the

requirements for the degree Doctor of Philosophy

in Materials

by

Thomas Rocco Cristiani

Committee in charge:

Professor Jacob N. Israelachvili, Co-Chair, *in memoriam*

Professor Omar Saleh, Co-Chair

Professor J. Herbert Waite

Professor Craig Hawker

June 2019

The dissertation of Thomas Rocco Cristiani is approved.

_____

J. Herbert Waite

_____

Craig Hawker

_____

Omar Saleh, Committee Chair

December 2018

Characterizing the relationships between micro- and nano-scale structure and the interfacial and mechanical properties of biological and bio-inspired materials

by

Thomas R. Cristiani

ACKNOWLEDGEMENTS

While toiling away to assemble the figures and arguments which best sum up my graduate work, I knew that this brief section, saved for last, would be the most challenging and personally fulfilling. As cliché as it may seem, it is exceptionally difficult to put into words how overwhelmingly grateful I am to have known and leaned from my advisor and friend, the late Professor Jacob Israelachvili. His gleeful brilliance and stubborn pursuit of the truth were unparalleled and inspire me, and so many others within his academic family, to approach my own research with equal passion and dedication. For the tremendous impact that he has had on my life over the past five years, I would like to dedicate this dissertation to Jacob, in his memory. Of course, Jacob would not want me to dwell on the past, and he knew, as well as I do, that there are plenty more people to acknowledge!

I would like to start by thanking the remaining members of my committee, Professors J. Herbert Waite, Craig Hawker, and Omar Saleh, whose support and intellectual guidance have been extremely valuable, especially during the home stretch. Along these lines, I would also like to thank Professor Martin Moskovits, a dear friend and colleague of Jacob's who helped maintain stability at the lab after Jacob's passing. Graduate school would also not have been anywhere near as enjoyable or entertaining without my friends and fellow Interfacial Science Lab contemporaries, Dr. Yair Kaufman, Dr. Himanshu Mishra, Dr. Dong-Woog Lee, Dr. Stephen Donaldson, Dr. Nadine Sterling, Dr. Saurabh Daas, Dr. Mike Rapp, Dr. Matt Gebbie, Dr. Alex Schrader, Dr. Nick Cadirov, Dr. Sandy Chen, Dr. Howie Dobbs, Dr. Zach Berkson, Dr. Kai Kristiansen, Dr. Roberto Andresen Eguiluz, Jeff Scott, George Degen, and Garrett

Lindsey – thank you. I am also grateful for the generous help and advice I have received from Nancy Emerson over the years while she was still Jacob's right-hand woman.

I would also like to thank my exceptional collaborators at UCSB outside of Jacob's lab, namely Dr. Emmanouela Filippidi, Dr. Kollbe Ahn, Dr. Megan Valentine, Dr. Claus Eisenbach, Dr. Keila Kunha, Dr. Joan-Emma Shea, and Billy Wonderly, for their stimulating discussions, hard work, and fruitful insights. I also thank the Procter and Gamble Company for their financial support and the collaborative efforts of Peter Koenig, Knut Meinert, Andrei Bureiko, Matt Ehrman, Sumanth Jamadagni, Zhiwei Shi, and Zhanping Zhang.

My girlfriend Erika has also spent the last four years loving and supporting me despite my haphazard, tenuously-balanced, over-committed lifestyle at the intersection of science, singing, and drumming, and has graciously endured late nights, unknown futures, the deepest of ruts, and the most inspiring "Eureka!" moments. She is my rock and my muse, and I am so lucky to have met and held on to her during my Ph. D.

And finally, an enormous thank you to my siblings, Andrea, Alicia, Peter, and Ted, and my parents, Susanna and Thomas, for their unwavering support, even as I traveled across the country to pursue my dreams of earning my doctorate. My family has always encouraged me to take risks and seize whichever opportunities would ultimately lead towards the most happiness in my life. As I start my next chapter, I would like them to know that their love will always be lingering among the pages.

VITAE OF THOMAS ROCCO CRISTIANI

December 2018

EDUCATION

University of California, Santa Barbara (UCSB): 2013-2018

Ph.D., Materials Science

Specialization: Interfacial phenomena, surface forces, friction, biomolecular adhesion, polymer networks and gels

University of Delaware: 2009-2013

B.Ch.E., Chemical Engineering

RESEARCH EXPERIENCE

Doctoral Research: Materials Department, UCSB, 2014-2018

Advisor: Jacob N. Israelachvili

- Developed and characterized biologically-inspired advanced polymer materials with energy dissipation and protective coating applications.

- Studied the molecular-scale interactions of peptide and peptoid model adhesives at inorganic surfaces.

- Managed collaborations with The Procter & Gamble Company to study and model the frictional and adhesive properties of skincare, cosmetics, and hair care products. Designed and developed custom instruments and complementary computer software to automate data collection, logging, and analysis for high-throughput adhesion and friction measurements.

Undergraduate Researcher: Dept. of Chemical Engineering, University of Delaware, 2013

Advisor: Christopher J. Kloxin

- Developed novel quaternary-phosphonium-functionalized vinyl BPA monomers for use in thiol-ene hydroxide exchange membranes.

Undergraduate Research: Dept. of Materials Science and Engineering, University of Delaware, 2009-2012

Advisor: Joshua M. O. Zide

- Modeled thermodynamic equilibria and strain-induced concentration gradients in doped III-V semiconductor nanoparticles.

PRESENTATIONS AT CONFERENCES/SYMPOSIUMS

- Oral Presentation 2018 American Institute for Chemical Engineers (AIChE) annual meeting, Pittsburg, PA, *Studying the Toughening Mechanism of Mussel-Inspired Iron-Catechol Complexes in Epoxy Networks*.

- Oral Presentation 2018 American Institute for Chemical Engineers (AIChE) annual meeting, Pittsburg, PA, *Mussel-Inspired Peptoids: The Backbone's Role in Adhesive Properties*.

- Oral Presentation 2016 American Institute for Chemical Engineers (AIChE) annual meeting, San Francisco, CA, *Enhancing Epoxy Network Toughness and Recoverability with Mussel-Inspired Catechol-Iron Crosslinks*.

- Speaker, MRL IRG-1 Seminar (MRSEC-funded seminar on wet adhesion); University of California, Santa Barbara; 3 talks during 2015-2017.

PUBLICATIONS

(1) *Characterizing dynamic, high-frequency friction in lubricating complex-fluid thin films between viscoelastic surfaces.* **Cristiani, TR* (co-1st author)**; Cadirov, NA; Ehrman, M; Kristiansen, K; Scott, J; Jamadagni, S; Israelachvili, JN. (2018) ***Tribology Letters***, 66 (4):149

(2) *Rates of cavity filling by liquids.* Seo, D; Chen, SY; Kaufman, Y; **Cristiani, TR**; Page, SH; Koenig, PH; Gizaw, Y; Lee, DW; Israelachvili, JN. (2018) ***Proc. Natl. Acad. Sci. USA***, 115 (32):8070-8075.

(3) *Toughening elastomers using mussel-inspired iron-catechol complexes.* Filippidi, E*; **Cristiani, TR* (co-1st author)**; Eisenbach, CD; Waite, JH; Israelachvili, NJ; Ahn, BK; Valentine, MT. (2017) ***Science***, 358 (6362):502-505.

(4) *Tuning underwater adhesion with cation-π interactions.* Gebbie, MA; Wei, W; Schrader, AM; **Cristiani, TR**; Dobbs, HA; Idso, M; Chmelka, BF; Waite, JH; Israelachvili, JN. (2017) ***Nature Chemistry***, 2017, 9 (5):473-479.

(5) *Observation of self-assembled core-shell structures in epitaxially embedded TbErAs Nanoparticles.* Dongmo, P; Harthshorne, M; **Cristiani, TR**; Jablonski, ML; Bomberger, C; Isheim, D; Seidman, DN; Taheri, ML; Zide, JMO. (2014) ***Small***, 10 (23):4920-4925.

(6) *A simple thermodynamic model for the doping and alloying of nanoparticles.* Petropoulos, JP; **Cristiani, TR**; Dongmo, PB; Zide, JMO. (2011) ***Nanotechnology***, 22 (24):245704

PUBLICATIONS IN PREPARATION

(7) Mussel-inspired peptoids: Studying the effect of backbone chemistry and structure on intrinsically-disordered biomolecular adhesives. **Cristiani, TR* (co-1st author)**; Wonderly, B*; Cunha e Silva, K*; Degen, GD.; Shea, JE; Waite, JH; Israelachvili, JN. (2018) ***In preparation***

(8) *Automated measurement of hair-hair single-fiber adhesion.* **Cristiani, TR* (co-1st author)**; Cadirov, NA*; Zhang, Z; Shi, Z; Bureiko, A; Andresen Eguiluz, RC;

Kristiansen, K; Scott, J; Meinert, K; Koenig, PH; Israelachvili, JN. (2018) ***In preparation***

(9) *Adhesion hysteresis of polystyrene thin films.* Degen, GD; **Cristiani, TR**; Cadirov, NA; Israelachvili, JN. (2018) ***In preparation***

NEWS & PRESS

(1) *Designing tougher elastomers with ionomers.* Winey, KI. ***Science***, 358 (6362):449-450

(2) *Material inspired by ocean mussels could lead to self-healing plastics*. Service, RS. (Oct. 26, 2017) ***Science News.*** (www.sciencemag.org/news/2017/10/material-inspired-ocean-mussels-could-lead-self-healing-plastics)

(3) *Mussels' iron grip inspires strong and stretchy polymer.* Sanderson, K. (2017) ***Chemical & Engineering News***, 95 (44):8 (cen.acs.org/articles/95/i44/Mussels-iron-grip-inspires-strong-stretchy-polymer.html)

(4) *Mussel power for building better elastomers.* Bradley, D. (Nov. 23, 2017) ***Materials Today.*** (www.materialstoday.com/polymers-soft-materials/news/mussel-power-for-building-better-elastomers/)

(5) *Learning from Mussels*. Cohen, J. (Oct. 26, 2017) ***The UC-Santa Barbara Current***. (www.news.ucsb.edu/2017/018460/learning-mussels). Republished by: ***Phys.org, EurekaAlert!, Futurity, LongRoom News, CienciaPlus Europa Press, Le Scienze.***

(6) *Mussel-inspired plastic could make self-repairing body armour*. Crane, L. (Oct. 26, 2017) ***NewsScientist*** (www.newscientist.com/article/2151532-mussel-inspired-plastic-could-make-self-repairing-body-armour/?utm_campaign=RSS%7CNSNS&utm_source=NSNS&utm_medium=RSS&campaign_id=RSS%7CNSNS-)

(7) *Mussel-inspired plastic may lead to self-repairing body armour*. (Oct. 27, 2017) ***Business Standard.*** (www.business-standard.com/article/pti-stories/mussel-inspired-plastic-may-lead-to-self-repairing-body-armour-117102700777_1.html)

(8) *Mussel inspires development of stronger and stretchier polymers.* (Oct. 30, 2017) ***The Engineer.*** (www.theengineer.co.uk/mussel-strong-stretchy-polymers/)

(9) *Mimicking mussel mechanics.* Birkendal, H. (2017) ***Nature Chemistry***, 9 (5):408-409.

(10) *Mussel glues rely on cation-aromatic attraction.* Torrice, M. (2017) ***Chemical & Engineering News***, 95 (8):7. (cen.acs.org/articles/95/i8/Mussel-glues-rely-cation-aromatic.html)

TEACHING EXPERIENCE

Teaching Assistant:

Colloids and Interfaces I, UCSB, 2016

Introduction to the Structure and Properties of Materials, UCSB, 2014

OUTREACH

ScienceLine "Ask a Scientist": Materials Research Lab, UCSB, 2014-2018

ABSTRACT

Characterizing the relationships between micro- and nano-scale structure and the interfacial and mechanical properties of biological and bio-inspired materials

by

Thomas Rocco Cristiani

Interfacial phenomena and materials properties are not only influenced by the chemical makeup, and therefore the highly localized intermolecular forces, between surface and bulk molecules, but also can heavily depend on geometry, self-assembly, dynamic/transient interactions, and the development of specific micro- and nano-structure. This general principle can be applied to a variety of systems including inorganic materials, polymeric materials, complex fluids and colloidal systems, and biological and bio-inspired materials. This dissertation explores how micro-/nano-structure and dynamic phenomena influence the macroscopic properties and performance of two broad classes of materials: (i) mussel-mimetic polymer materials and adhesives and (ii) consumer skincare and hair care products.

In Part 1 (Chapters 2 and 3) of this dissertation, two different materials systems inspired by *Mytilus* mussels have been synthesized. Chapter 2 presents nanoscale adhesion and cohesion force measurements of a mussel-mimetic adhesive peptoid between mica surfaces to further elucidate the mechanisms mussels employ to achieve robust wet adhesion. Comparing these results to those measured using peptide molecules

of identical sequence, we determine that nano-scale aggregation and the formation of transient secondary structure, driven by backbone hydrogen bonding, exists only in the peptide molecules, causing differences in the nano-structure and hydration of solution-deposited films in each system, and therefore influencing the intermolecular interactions available between opposing surfaces. Chapter 3 focuses on translating strong but reversible iron-catechol coordination chemistry found in the mussel's byssal threads to dry epoxy networks in order to achieve enhanced mechanical strength and toughness through reversible energy dissipation. We find that there exists a critical iron-catechol complex concentration above which the materials develop an ionomeric nano-structure, which provides an additional mode of stress translation, thereby further increasing the material's mechanical properties.

Part 2 (Chapters 4 and 5) shifts focus from mussel-mimetic materials to measuring the friction and adhesion of consumer skincare and hair care products. Chapter 4 explores the friction dynamics of model skin creams using a high-speed friction attachment to the surfaces forces apparatus. We demonstrate that analysis of the time-varying frequency components of friction signals can unambiguously differentiate between different modes of sliding, giving insights into how surface and fluid properties impact tribological properties. Finally, Chapter 5 details the development of a custom instrument designed to measure the exceedingly weak adhesion forces between human hair fibers both clean and coated with consumer hair care products. Calibrating the native elasticity of the hair fibers, we can use their own mechanical properties to measure forces as low as ~1 nN using a simple optical microscope. We find that the micro-/nano-structure on the hair surface causes broad, spatially-variant distributions in the adhesion force between fibers

and necessitates large numbers of replicate experiments, which have been automated. A model which uses topographical measurements of the hairs' surfaces has also been developed which can predict the magnitude, breadth, and shape of the complex, multimodal adhesion force distributions from the differential surface geometry.

TABLE OF CONTENTS

LIST OF FIGURES

1 Introduction, motivation, and background

Many biologically relevant materials are governed by meso-scale interactions between amorphous polymeric molecules which are often arranged through self-assembly and aggregation into specific structures on the nanometer to micron length scales. These length scales are larger than the precise atomic ordering of crystalline solids, making them difficult to measure precisely with typical scattering and diffraction techniques, but small enough to not be measurable with simpler techniques such as optical microcopy and macroscopic force measurements. Therefore, to determine the important intermolecular interactions in such materials systems and gain insights into the mechanisms by which their structures determine their function requires a combination of both reductionist approaches, such as synthesizing model systems which incorporate and distil key molecular motifs found in the natural systems, as well as constructionist approaches which employ careful experimental and instrument design to directly measure interactions in ways which closely mimic the native biological systems. This thesis explores the relationships between micro- and nano-scale structure and macroscopic properties in a variety of biological and bio-inspired materials using nanoscale force measurements, polymer synthesis and characterization, tribological experiments, and custom instrument control and data analysis algorithms.

1.1 Part 1: Mussel-inspired materials

The marine mussel's ability to use durable byssal threads and plaques to adhere to various rocky surfaces and remain steadfast in raging ocean tides has inspired the research and development of many advanced synthetic materials, including underwater adhesives [1–6], self-healing materials [7–12], tough and extensible hydrogels [11, 13–16], functional

coatings [3, 17–19], and even battery materials [20]. Sequencing of the proteins the mussel produces to form its plaques and threads [3] has revealed a high concentration of the cationic amino acid lysine (Lys) and the post-translationally-modified amino acid 3,4-dihydroxyphenylalanine (Dopa), both at the plaque-substrate interface and within the byssal threads. Dopa's main functional feature is a catechol terminated side-chain which is chemically diverse and can participate in mono-/bidentate hydrogen bonding, metal-ligand coordination bonding, and oxidative covalent coupling.

In Chapter 3, using nano-scale adhesion and cohesion force measurements, we study the effects of Dopa ring hydroxylation and backbone chemistry/structure in mussel-mimetic model peptides and peptoids to learn more about the molecular-scale details of the adhesive/cohesive mechanism in the mussel's interfacial proteins. We find that trends in adhesion/cohesion force with varying ring hydroxylation heavily depend on the backbone chemistry and its effect on intermolecular aggregation.

This study is followed in Chapter 3 by the presentation of a dry, high-modulus, energy dissipating epoxy network, inspired by the byssal thread's cuticle, which contains reversible iron-catechol coordination bonds. We demonstrate that the addition of iron-complexes causes orders-of-magnitude increases in the mechanical properties of the network, which can be explained not only by the complexes themselves, but also by the nano-scale iron clusters which they form.

Both studies reinforce the notion that molecular- and nano-scale interactions drive macro-scale function within biological and bio-inspired materials and should always be considered in materials design.

1.2 Part 2: Tribological and adhesive properties of consumer products

Consumer skincare, hair care, and cosmetic products must achieve their desired functions (moisturization, lubrication, coloration, cleaning, disinfection, etc.) while also being pleasing to the individual using them. At a simple level, changing a product's color or scent can make it more desirable to the target audience. However, more subtle phenomena, such as how the product *feels* and *behaves* are more difficult to engineer. Often, consumer products companies will formulate large numbers of prototypes and employ panels of experts or general consumers to provide feedback on the prototypes' *feeling* and *behavior* using surveys. These methods are time consuming, expensive, and can be limited by selection bias. It is more efficient, therefore, to determine how consumer perception of a product correlates with not only the product's formulation, but perhaps the physical properties of the product as well.

In Part 2 of this dissertation, we present two methods for measuring the frictional and adhesive properties of consumer skincare products between polymer surfaces (Chapter 4) and hair care products between individual hair fibers (Chapter 5). Unique instrumentation was developed for each study and is discussed in their respective chapters.

1.3 Background

1.3.1 Intermolecular interactions

Surfaces and molecules attract and repel at a distance according the specific and non-specific interactions governed by their constituent atoms which are exclusively electromagnetic in nature. The simplest representation of these interactions when considering just two interacting atoms/molecules is a pair potential, $w(r)$, which encapsulates the

energetic requirements associated with bringing the two molecules from infinite separation to some separation distance, r [21]. The force of this interaction, f, can be obtained by computing the negative derivative of the pair potential with respect to the separation distance.

This pair potential and the forces derived from it can be complex, even for simple molecules interacting across a single-component medium, because the overall pair potential involves contributions from each atom within the molecules interacting with themselves and with the atoms from the molecules in the medium. Explicitly determining this pair potential from first principles would therefore require full quantum mechanical treatment of each constituent atom in the system, which, even with some of the world's most powerful supercomputers, is not feasible for systems containing more than 100s of atoms.

Therefore, for practical reasons, the types of electromagnetic interactions that contribute to these pair potentials have be categorized by their unique functional forms and can be simplified into four main categories: (i) van der Waals interactions, which arise from permanent and induced dipoles, dispersion forces, and polarizability between atoms, (ii) electrostatic interactions between permanently charged species, (iii) hydrogen bonding, arising from specific dipolar and charge-transfer-mediated interactions which involve electronegative species (such as F, Cl, Br, I, O, S, Se, N, P, or C) covalently bound to H, and (iv) solvation interactions, which, in water, include both (a) highly-attractive hydrophobic interactions arising from the depletion of water and the disruption of water's hydrogen bonding network near hydrophobic surfaces, and (b) repulsive hydrophilic interactions which arise from the osmotic pressure needed to dehydrate hydrophilic surface groups and remove hydration layers from solutes. The distance dependence of the van der Waals and electrostatic interactions, when considered for extended surfaces interacting across a liquid

medium, can be combined and described by the Derjaguin-Landau-Verwey-Overbeek (DLVO) theory [21–23]. Hydrogen bonding and solvation forces are less understood and do not have a well established interaction potential, though recent progress has been made on developing a combined, empirical hydrophobic/hydrophilic interaction potential [24]. Knowing the interaction potentials allows for extrapolation of these interactions to extended surfaces and more complicated geometries to compute the full force-distance profile for two interacting bodies, $F(D)$.

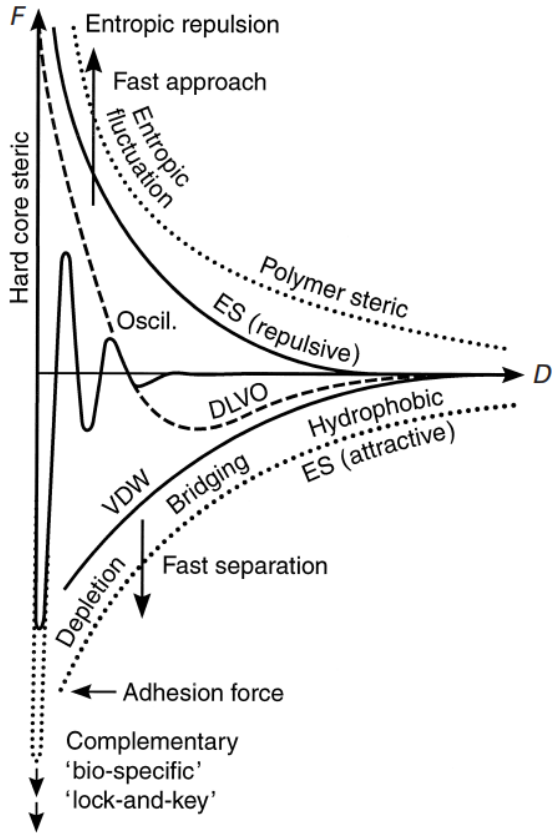

Figure 1.1 – Interaction potentials in biological and colloidal systems. Depiction of the varied interaction potentials which may exist between two complex macromolecules, biomembrane surfaces, or surfaces interacting across complex fluids. No one system is likely to display all of these interactions at the same time. However, biological molecules and surfaces often interact via four or more of these forces either simultaneously or following on one another. Reproduced from [21].

These simpler fundamental interactions become even more complicated in colloidal systems, which involve larger molecules, polymers, self-assembled membranes, and proteins.

To describe such colloidal systems, one must also consider steric repulsions, polymer bridging, complementary ‘lock-and-key’ interactions, entropic fluctuations, depletion attractions, and other potentially oscillatory structural forces. These mesoscopic interactions are also often non-equilibrium in nature and depend heavily on the rate of approach and separation or whether or not interacting molecules/surfaces have been sheared.

1.3.2 Friction

Friction is inherently different from the interaction forces described above because it is defined as a reactionary force, which responds to the motion between two surfaces. If two surfaces were molecularly smooth and interacting in intimate contact (in air or vacuum), and their atoms were in perfect register with those making up the opposing surface, the friction force would be related to the force required to laterally move the surfaces one atomic distance, or one lattice site. This process involves both the dilation of the two surfaces to accommodate the rearrangement of surface atoms as well as the force required to break the physical adhesive bonds between the atoms. The force required to complete these processes is the frictional force [25]. For less regular geometries, the same principles apply, but effects originating from the momentum and elasticity of surface asperities can further complicate the friction response.

Finally, if two surfaces are interacting across an intervening medium, like a lubricant or complex fluid, molecular ordering, such as polymer alignment and shear-induced crystallization/melting, can change the resistance to shear by changing the fluid viscosity or jamming the component molecules in place [26]. This change in the system’s resistance to sliding can have varied dependencies on the applied normal load and shearing velocity between the surfaces, and, in combination with surface structure, can lead to friction

dynamics such as regular and intermittent stick-slip sliding [27–30] and mechanical resonances.

Chapters 4 and 5 explore the frictional behavior of complex fluids between polymer surfaces and hair fibers. Structural and lubricant-induced friction dynamics, including stick-slip friction, are observed in both systems.

1.4 Experimental techniques

1.4.1 The Surface Forces Apparatus (SFA)

The surface forces apparatus (SFA, schematically represented in Figure 1.2A, full-scale drawing in) is used in Chapters 2 and 4 to measure the attractive and repulsive forces between interacting surfaces. Classically, the SFA uses multiple-beam interferometry (MBI) [21, 31, 32] to measure the absolute distance, to < 1 Å resolution, between atomically smooth pieces of back-silvered mica which are configured in a cross-cylinder geometry (Figure 1.2). This is achieved first by sending columnated white light through the surfaces, which, due to the silver layers, are typically only 1% transmissive. The light then constructively and destructively interferes between the silver layers and is passed through a spectrometer where it is split into its component wavelengths, forming fringes of equal chromatic order (FECO, Figure 1.2B). The wavelength of the center of an 'odd' order fringe when the mica surfaces are in intimate contact in dry nitrogen, λ_n^0, can then be compared to the wavelength, λ_n^D, of the same order fringe when the surfaces are separated by some unknown distance, *D*, in order to compute the distance. The details of the MBI equations can be found in [31, 32].

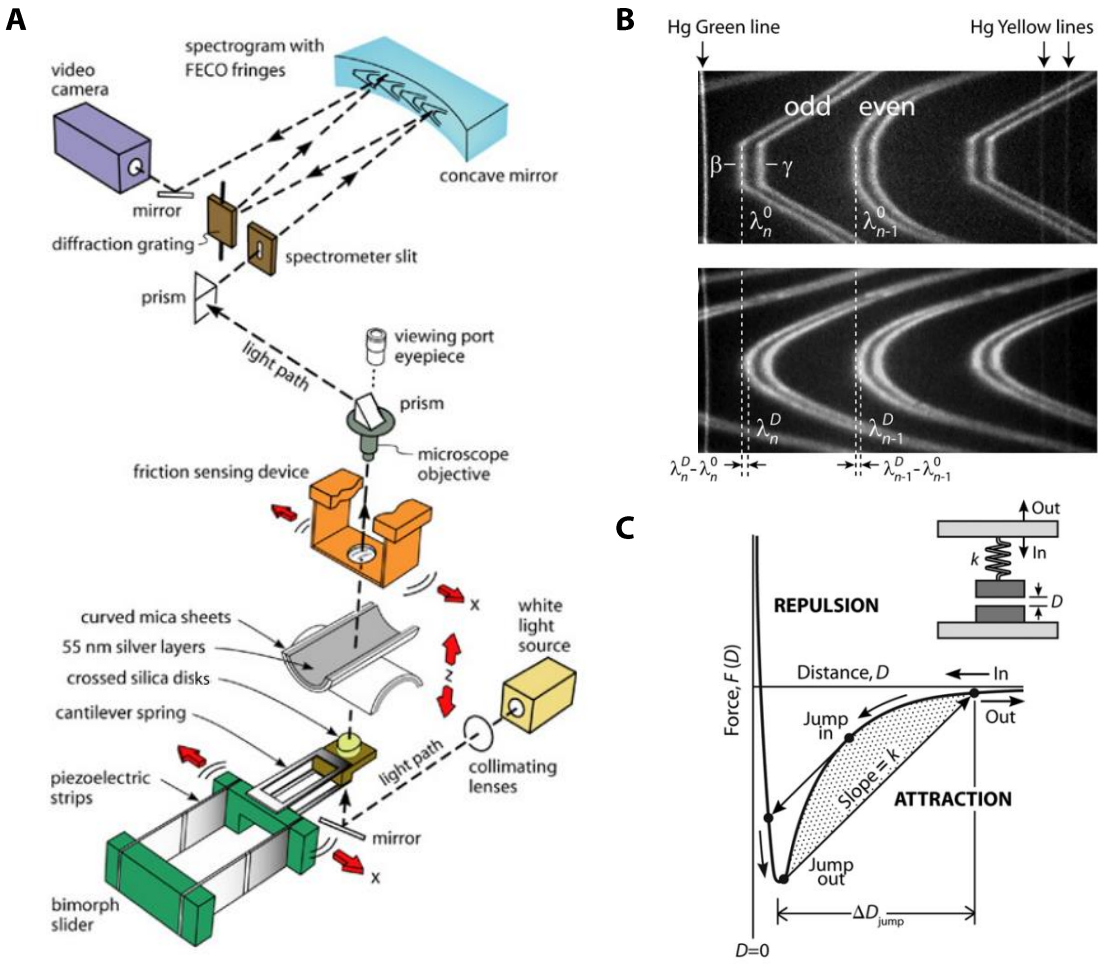

Figure 1.2 – The principles of the SFA. (A) Schematic of SFA setup depicting the full optical path. This illustration also includes representations of the bimorph slider and friction sensing devices, tribological attachments used to translate the bottom surface and measure parallel forces, respectively. (B) Representation of FECO fringes produced by the SFA from mica surfaces which are in hard contact in air (top, $D = 0$) and separated by $D \approx 9.9$ nm (bottom). The fringes appear as β and γ doublets due to the birefringence of mica. Also represented are the green and yellow Hg calibration lines. Finally, the flatting of the fringes in hard contact is due to elastic deformations in the mica and supporting glue layers. (C) Generic force vs. distance profile showing the instabilities, which can occur at the positions indicated. The surfaces will jump together on approach and apart on separation when the slope of $F(D)$ is equal to the measuring spring constant. The adhesion force is equivalent to the jump out distance multiplied by the spring constant. An infinitely stiff spring would therefore not have any instabilities and therefore experience no jumps. There are no equilibrium positions between the jump in and jump out points. (All panels adapted from [31]).

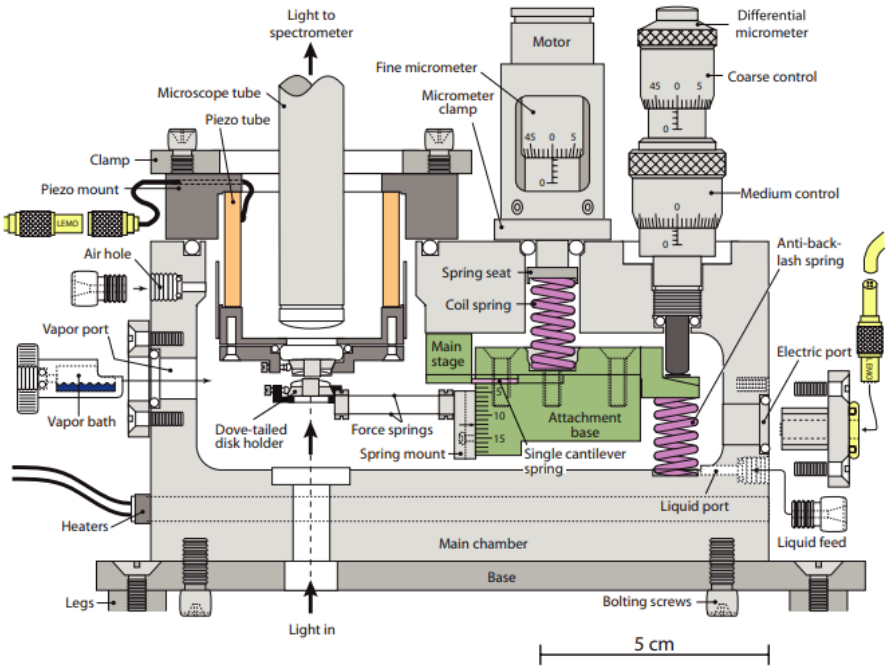

Figure 1.3 – Scale drawing of an SFA 2000, SurForce LLC. (Adapted from [31]). This front view of the SFA shows its major components, including the different coarse, fine, and ultra-fine motion controls, force-measuring and anti-backlash springs, optical ports and electrical ports. Also shown are ports allowing for control of the temperature, humidity, and gas content within the main SFA chamber.

The distance between the surfaces far from contact can be controlled precisely and linearly by moving the bottom surface, mounted on a double cantilever spring of constant, k, up and down using a linear motor or by moving the top surface up and down using a piezo electric crystal (Figure 1.3). When the surfaces interact, the bottom surface will deflect positively (repulsive) or negatively (attractive) with respect to the expected position. Therefore, the measured distance between the surfaces, D, can be compared to the expected distance from calibrating the motion of the piezo or motor, D_{expected}, and used to calculate the force between the surfaces, $F = k(D - D_{expected})$.

For strongly adhering surfaces, there may be jump in and jump out instabilities which arise from the slope of the interaction potential exceeding the spring constant of the force-measuring spring. The minimum force measured before jump out is equivalent to the force of adhesion, F_{ad}, and can be computed by multiplying the jump out distance, D_{jump}, by the

cantilever spring constant. This method is used to measure the adhesive/cohesive forces of peptoid molecules between mica surfaces in Chapter 2.

1.4.2 Uniaxial tensile testing

Figure 1.4 is a schematic representation of a material under uniaxial tensile stress. The material represented on the left is a square prism with initial length, L_0, and width and depth both equal to the side length s_0. Under tensile force, F, the material deforms to a new length, L, and side length, s. The strain, ε, is defined as the change in length of the material under tension while the stress, σ, can be defined as the tensile force, F, divided by the area perpendicular to the tensile loading direction, $A = s^2$. The relationship between σ and ε is often used to characterize the mechanical properties of a material. For an ideal purely elastic material, σ is directly proportional to ε by a factor known as the elastic modulus, E. These materials eventually experience brittle failure and do not deviate from this linear relationship at any point along the stress vs. strain curve.

For most real materials, except for highly crystalline ceramics, this linear relationship is true only at low strains. Reorganization of molecules and defects within the material at larger strains cause deviations from ideality [33]. In polymeric materials, much of the stress response depends on interchain friction, entanglements, and uncoiling of the polymer backbones which behave as entropic springs [34–36]. These processes may happen at different rates and have different associated energies and therefore cause a polymer material to have viscoelastic properties whereby the stress response is highly dependent on the strain rate (and/or temperature). This is the most basic overview of polymer mechanics necessary to understand the work presented in Chapter 3 and any other information is contained within the discussion there.

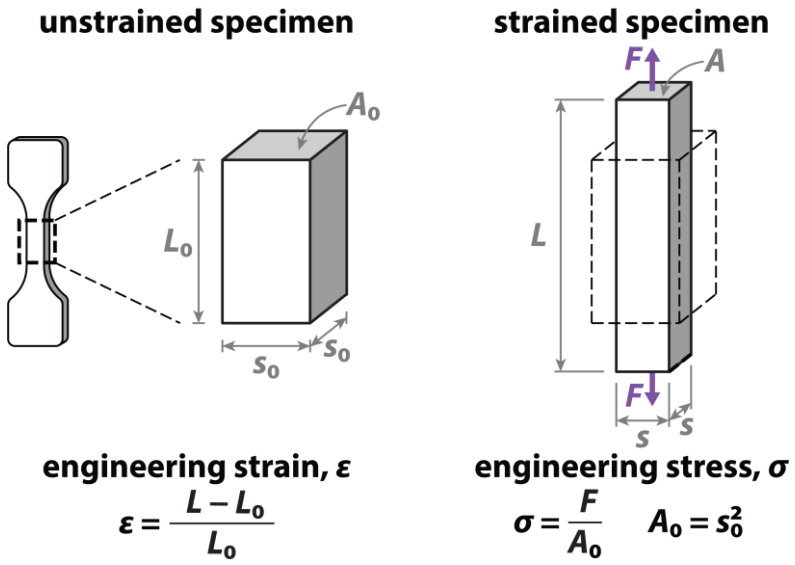

Figure 1.4 – Schematic representation of a material being uniaxially deformed, defining the engineering stress, σ, and strain, ε.

1.5 Other materials characterization methods

Discussed in more detail in the relevant chapters, in addition to the SFA (and its tribological attachments) and uniaxial tensile testing, a sweet of materials characterization techniques, including infrared spectroscopy, Raman spectroscopy, small- and wide-angle X-ray scattering, scanning and transmission electron microscopy, energy dispersive X-ray spectroscopy, nuclear magnetic resonance spectroscopy, X-ray photoelectron spectroscopy, rheology, differential scanning calorimetry, dynamic mechanical analysis, and other customized mechanical characterization techniques were used to characterize the mechanical, chemical, and microstructural properties of the materials presented in this dissertation.

1.6 References

1. Zhong, C., Gurry, T., Cheng, A.A., Downey, J., Deng, Z., Stultz, C.M., Lu, T.K.: Strong underwater adhesives made by self-assembling multi-protein nanofibres. Nat. Nanotechnol. 9, 858–66 (2014)

2. Yu, M., Deming, T.J.: Synthetic Polypeptide Mimics of Marine Adhesives.

Macromolecules. 31, 4739–4745 (1998)

3. Lee, B.P., Messersmith, P.B., Israelachvili, J.N., Waite, J.H.: Mussel-Inspired Adhesives and Coatings. Annu Rev Mater Res. 41, 99–132 (2011)

4. Shao, H., Stewart, R.J.: Biomimetic underwater adhesives with environmentally triggered setting mechanisms. Adv. Mater. 22, 729–733 (2010)

5. Levine, Z.A., Rapp, M. V, Wei, W., Mullen, R.G., Wu, C., Zerze, G.H., Mittal, J., Waite, J.H., Israelachvili, J.N., Shea, J.-E.: Surface force measurements and simulations of mussel-derived peptide adhesives on wet organic surfaces. Proc. Natl. Acad. Sci. 113, 4332–4337 (2016)

6. Gebbie, M.A., Wei, W., Schrader, A.M., Cristiani, T.R., Dobbs, H.A., Idso, M., Chmelka, B.F., Waite, J.H., Israelachvili, J.N.: Tuning underwater adhesion with cation–π interactions. Nat. Chem. 9, 473–479 (2017)

7. Long, R., Mayumi, K., Creton, C., Narita, T., Hui, C.Y.: Time dependent behavior of a dual cross-link self-healing gel: Theory and experiments. Macromolecules. 47, 7243–7250 (2014)

8. Faghihnejad, A., Feldman, K.E., Yu, J., Tirrell, M. V., Israelachvili, J.N., Hawker, C.J., Kramer, E.J., Zeng, H.: Adhesion and Surface Interactions of a Self-Healing Polymer with Multiple Hydrogen-Bonding Groups. Adv. Funct. Mater. 24, 2322–2333 (2014)

9. Holten-Andersen, N., Harrington, M.J., Birkedal, H., Lee, B.P., Messersmith, P.B., Lee, K.Y.C., Waite, J.H.: pH-Induced metal-ligand cross-links inspired by mussel yield self-healing polymer networks with near-covalent elastic moduli. Proc. Natl. Acad. Sci. U. S. A. 108, 2651–2655 (2011)

10. Chen, Y., Guan, Z.: Multivalent hydrogen bonding block copolymers self-assemble into strong and tough self-healing materials. Chem. Commun. (Camb). 50, 10868–70 (2014)

11. Krogsgaard, M., Behrens, M. a., Pedersen, J.S., Birkedal, H.: Self-healing mussel-inspired multi-pH-responsive hydrogels. Biomacromolecules. 14, 297–301 (2013)

12. Ahn, B.K., Lee, D.W., Israelachvili, J.N., Waite, J.H.: Surface-initiated self-healing of polymers in aqueous media. Nat. Mater. 13, 867–872 (2014)

13. Sun, J.-Y., Zhao, X., Illeperuma, W.R.K., Chaudhuri, O., Oh, K.H., Mooney, D.J., Vlassak, J.J., Suo, Z.: Highly stretchable and tough hydrogels. Nature. 489, 133–136 (2012)

14. Appel, E. a., del Barrio, J., Loh, X.J., Scherman, O. a.: Supramolecular polymeric hydrogels. Chem. Soc. Rev. 41, 6195 (2012)

15. Sun, T.L., Kurokawa, T., Kuroda, S., Ihsan, A. Bin, Akasaki, T., Sato, K., Nakajima, T., Gong, J.P., Haque, M.A., Nakajima, T., Gong, J.P., Haque, M.A.: Physical hydrogels composed of polyampholytes demonstrate high toughness and viscoelasticity. Nat. Mater. 12, 932–937 (2013)

16. Menyo, M.S., Hawker, C.J., Waite, J.H.: Versatile tuning of supramolecular hydrogels through metal complexation of oxidation-resistant catechol-inspired ligands. Soft Matter. 9, 10314–10323 (2013)

17. Lim, C., Huang, J., Kim, S., Lee, H., Zeng, H., Hwang, D.S.: Nanomechanics of Poly(catecholamine) Coatings in Aqueous Solutions. Angew. Chemie Int. Ed. 55, 3342–3346 (2016)

18. Lee, H., Dellatore, S.M., Miller, W.M., Messtersmith, P.B.: Mussel-Inspired Surface Chemistry for Multifunctional Coatings. Science. 318, 426–430 (2008)

19. Meis, N.N.A.H., Van Der Ven, L.G.J., Van Benthem, R.A.T.M., De With, G.: Extreme wet adhesion of a novel epoxy-amine coating on aluminum alloy 2024-T3. Prog. Org. Coatings. 77, 176–183 (2014)

20. Ryou, M.-H., Lee, Y.M., Park, J.-K., Choi, J.W.: Mussel-Inspired Polydopamine-Treated Polyethylene Separators for High-Power Li-Ion Batteries. Adv. Mater. 23, 3066–3070 (2011)

21. Israelachvili, J.N.: Intermolecular and Surface Forces: Revised Third Edition. Academic Press (2011)

22. Derjaguin, B., Landau, L.: Theory of the stability of strongly charged lyophobic sols and of the adhesion of strongly charged particles in solutions of electrolytes. Prog. Surf. Sci. 43, 30–59 (1993)

23. Verwey, E.J.W.: Theory of the Stability of Lyophobic Colloids. J. Phys. Colloid Chem. 51, 631–636 (1947)

24. Donaldson, S.H., Røyne, A., Kristiansen, K., Rapp, M. V., Das, S., Gebbie, M.A., Lee, D.W., Stock, P., Valtiner, M., Israelachvili, J.: Developing a General Interaction Potential for Hydrophobic and Hydrophilic Interactions. Langmuir. 31, 2051–2064 (2015)

25. Dowson, D.: History of Tribology. Professional Engineering Pub (1998)

26. Ruths, M., Steinberg, S., Israelachvili, J.N.: Effects of Confinement and Shear on the Properties of Thin Films of Thermotropic Liquid Crystal. Langmuir. 12, 6637–6650 (1996)

27. Feeny, B., Guran, A., Hinrichs, N., Popp, K.: A Historical Review on Dry Friction and Stick-Slip Phenomena. Appl. Mech. Rev. 51, 321 (1998)

28. Berman, A.D., Ducker, W.A., Israelachvili, J.N.: Origin and Characterization of Different Stick - Slip Friction Mechanisms †. 7463, 4559–4563 (1996)

29. Das, S., Cadirov, N., Chary, S., Kaufman, Y., Hogan, J., Turner, K.L., Israelachvili, J.N.: Stick-slip friction of gecko-mimetic flaps on smooth and rough surfaces. J. R. Soc. Interface. 12, 20141346 (2015)

30. Yoshizawa, H., Israelachvili, J.: Fundamental mechanisms of interfacial friction. 2. Stick-slip friction of spherical and chain molecules. J. Phys. Chem. 97, 11300–11313 (1993)

31. Israelachvili, J., Min, Y., Akbulut, M., Alig, A., Carver, G., Greene, W., Kristiansen, K., Meyer, E., Pesika, N., Rosenberg, K., Zeng, H.: Recent advances in the surface forces apparatus (SFA) technique. Reports Prog. Phys. 73, 036601 (2010)

32. Israelachvili, J.N., Adams, G.E.: Measurement of forces between two mica surfaces in aqueous electrolyte solutions in the range 0–100 nm. J. Chem. Soc. Faraday Trans. 1 Phys. Chem. Condens. Phases. 74, 975 (1978)

33. Lee, E.H.: Elastic-Plastic Deformation at Finite Strains. J. Appl. Mech. 36, 1 (1969)

34. Mead, D.W., Yavich, D., Leal, L.G.: The reptation model with segmental stretch. Rheol. Acta. 34, 360–383 (1995)

35. Gotlib, Y., Golovachev, G.: The relaxation of the polymer networks with interchain friction. J. Non. Cryst. Solids. 172–174, 850–854 (1994)

36. Gotlib, Y.Y., Gurtovenko, A.A.: The model theory of viscoelastic relaxation properties of bulk cross-linked polymers. Interchain friction effects. Macromol. Theory Simulations. 6, 523–551 (1997)

PART 1: Mussel-mimetic materials

2 Mussel-inspired peptoids: Studying the effect of backbone chemistry and structure on intrinsically-disordered biomolecular adhesives

2.1 Abstract

Intermolecular interactions are assumed to be dominated by amino acid side chains in intrinsically disordered proteins, such as highly charged and catecholic proteins employed by marine mussels to induce strong wet adhesion to rocky surfaces. However, it is known that the protein backbone influences protein hydration and structure. In this work, using a combination of nanoscale force measurements and molecular dynamics simulations, we demonstrate that by altering the backbone chemistry of short, mussel-mimetic adhesive peptides via synthesizing/modeling their peptoid counterparts, different adhesive/cohesive mechanisms between mineral surfaces can be achieved. Specifically, the lack of backbone hydrogen bonding allows for minimal intermolecular aggregation in solution and therefore the deposition of well-defined monolayers of peptoid molecules, providing a precise model system for determining the adhesive and cohesive contributions of the peptoid side chains. These insights highlight the possibility for using peptoids or peptoid/peptide hybrids as wet adhesives/primers whose intermolecular interactions can be specifically defined by side chain and backbone chemistry.

2.2 Introduction

The marine mussel uses robust byssal threads and plaques to adhere to rocky surfaces amidst turbulent waves and tidal forces [1]. Through extensive sequencing of the protein cocktail from which the mussel builds its threads and plaques, it has been determined that

proteins rich in both 3,4-dihydroxyphenylalanine (Dopa) and lysine (Lys) amino acids become localized at the plaque/substrate interface [1, 2]. Respectively, the catecholic and cationic side-chains in these residues are thought to work together to obtain optimal adhesion/cohesion through a combination of interactions. Cooperative interactions include charge-charge interactions between Lys and negative surface charges, mono- and bi-dentate hydrogen bonding between Dopa and surface oxides, metal chelation between Dopa and surface transition metals, cation-π bonding between Lys and aromatic side chains, oxidative coupling between Dopa residues, hydrophobic interactions, and π-π coupling [1, 3–5]. The complexity of this unique adhesive system has inspired numerous studies focused on determining the adhesive/cohesive strengths of native mussel proteins, mussel-inspired peptides, and mussel-inspired small molecules between various mineral and oxide surfaces [4, 6–14]. From these various studies, the relative importance of each of the above-listed intermolecular interactions has been inferred. However, absent from the literature is any consideration of the intermolecular forces arising from the peptide backbone chemistry and structure. Though the peptide sequences relevant to the mussel system are intrinsically disordered [15], the peptide backbone inherently influences intra- and intermolecular interactions, enabling transient β-sheet-like structuring, restricting backbone conformational freedom, and allowing hydrogen bonding with appropriate amino acid side chains. In this work, we study the effect of these backbone-mediated interactions by synthesizing peptoid analogues whose sequences are identical to peptides [16] inspired by mussel foot protein five (mfp-5) and measuring their surface interactions with mica using the surface forces apparatus (SFA). These results are corroborated with molecular dynamics (MD) simulations of both the peptide and peptoid molecules in solution and interacting with mica surfaces.

To give context to the current work, it is important to review the findings of the previous study by Gebbie, *et al*. [16] on peptide molecules whose sequences inspire the peptoid sequences in this work. In the previous study, cystine-linked dimers of a high-isoelectric-point segment of mfp-5, exhibiting high adhesion between cross-cylinder mica surfaces, were synthesized with varying amounts of ring hydroxylation in their aromatic residues (sequences depicted in Figure 2.1B). The maximum forces required to separate atomically smooth mica surfaces coated in these molecules exposed to low pH (< 3), high ionic strength (> 250 mM) solutions were reported. For molecules with either phenylalanine (Phe), tyrosine (Tyr), or Dopa populating the "X" position in the sequence (shown in Figure 2.1B), it was shown that multilayer films were consistently deposited, and all forces measured were due to cohesive interactions. To corroborate this interpretation, asymmetrical and symmetrical depositions of the peptide molecules, in which peptide films were deposited on one or both opposing mica surfaces, were shown to exhibit statistically identical pull-off forces for each peptide sequence. Most surprisingly, however, the strongest cohesive interactions were measured for the Phe-containing molecules, with the Tyr- and Dopa-containing molecules exhibiting lower, but equivalent cohesion. Comparing this trend in cohesion to the low cohesion of a hydrophobic leucine-substituted control sequence, it was inferred that the main cohesive interactions are cation-π-mediated, which are reduced by the entropically unfavorable steric contributions of the Tyr and Dopa hydroxyl groups. However, the authors were not so bold as to rule out other potential interactions. In this manuscript, we explore the possibility that the backbone chemistry and structure of the peptide molecules in the previous study are significant enough to impact the types of adhesive/cohesive interactions available to these classes of molecules. We observe significant differences between the adhesion/cohesion

strengths of the asymmetrically- and symmetrically-deposited peptoid films, allowing us to conclude that the peptoids can form distinct monolayers at each mica surface, driven by reduced aggregation in the absence of backbone hydrogen bonding groups. The peptoid films are also shown to be more densely packed, and therefore less hydrated, due to the backbone's increased hydrophobicity.

2.3 Results and Discussion

2.3.1 Design and synthesis of peptoids

Each peptoid sequence is comprised of peptoid analogues for the amino acids Lys, glycine (Gly), and cysteine (Cys), in addition to analogues of one of the aromatic amino acids Phe, Tyr, or Dopa. The locations and quantities of the Gly, Cys, Lys, and aromatic analogue residues are conserved among the three peptoids (Figure 2.1B). These 34-residue chains have sequences identical to the peptide sequences published in the previous work by Gebbie *et al.* and, more importantly, are prominently featured in mfp-5. The high charge content of the peptoid sequences, afforded by the ~35% Lys composition, allows these molecules to displace potassium ions bound to mica surfaces [17] and form multiple Coulombic interactions per peptoid molecule, thus nearly-irreversibly binding the first (and sometimes only) layer of each molecule to the mica surface. The aromatic side chains (Phe, Tyr, Dopa) mediate other interactions such as hydrophobic interactions, cation-π complexation, π-π interactions, and hydrogen bonding (for Tyr and Dopa only). Though these side-chain-mediated interactions are important, the most interesting feature of the peptoid molecules for this study is their backbone chemistry and structure. Peptoids differ from peptides simply by the relocation of the side chains from the α-carbon to the nitrogen.

This change in side chain placement causes the α-carbon to be achiral (it now has two hydrogen substituents), removes the N-H bond, and therefore the potential for backbone hydrogen bond donation, and weakens the delocalization of electrons in the N-C=O bond in the backbone, giving the backbone more conformational freedom. Together, these three differences cause peptoids to be more flexible molecules which tend to only form secondary (and higher-order) structure via specifically designed side chain interactions [18–20].

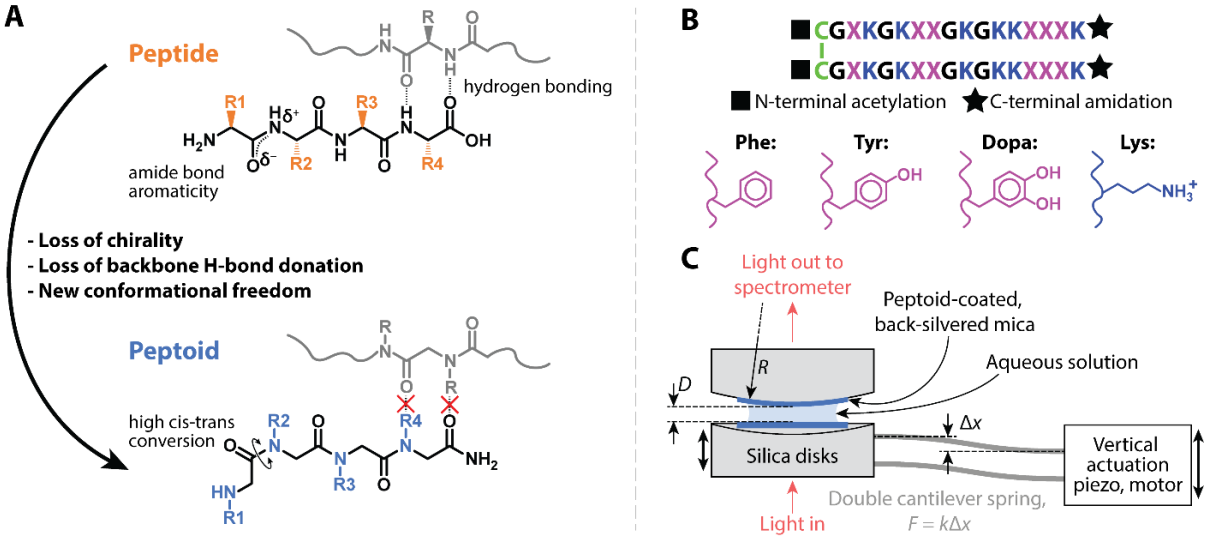

Figure 2.1 – Chemistry and experimental setup.A) A chemical description illustrating the differences between generic peptide (top) and peptoid (bottom) molecules. B) The sequence from which all peptides and peptoids discussed in this manuscript have been derived. For each molecule, the "X" position in the sequence can be either Phe, Tyr, or Dopa (purple) and is internally consistent for a given molecule. The lysine side chain is depicted in blue and the glycine side chain (G) is a simple hydrogen. C) Schematic of the SFA 2000 used to measure force vs. distance profiles and adhesion/cohesion forces in this study.

2.3.2 Adhesive and cohesive interactions between peptoid films

When exposed to the 250 mM KNO_3, 100 mM acetic acid solutions used in this study (high salt conditions) and separated at nanometers-per-second, mica surfaces, such as those schematically depicted in Figure 2.1C, are very minimally adhesive (F/R < 2 mN/m, Figure 2.3C,D). After depositing thin layers of peptoids asymmetrically on one the mica surfaces from dilute (~ 1 μM peptoid) solutions at the same high salt conditions (depicted on the left

side of the Figure 2.2 inset), adhesion forces of ~5 to 50 mN/m are observed, depending on the peptoid chemistry (Figure 2.2). Overall, these forces are similar in magnitude to the forces measured via the same method with analogous peptide molecules (Figure 2.2, orange bars), but demonstrate a different trend with aromatic ring hydroxylation. Most notably, we observe that the pull-off force measured for the asymmetrically deposited Phe peptoid is only about 20% of the force measured in the peptide system. However, for the same Phe-substituted molecules deposited symmetrically on both mica surfaces, the detachment forces are comparable to their peptide counterparts. We conclude that this must be due to different failure mechanisms in the asymmetrical and symmetrical Phe peptoid systems which are driven by the formation of discrete monolayers at each mica surface. Asymmetrical deposition therefore leads to weak adhesive failure between both the Phe rings and few unbound Lys and the opposing mica surface (Figure 2.5A). Symmetrical deposition allows the strongly bound peptoid molecules to interact with one another via cation-π bonding, π-π coupling, and hydrophobic forces, leading to high cohesion, similar to what is observed in the peptide system [16] (Figure 2.2 and Figure 2.5B). This difference between asymmetrical and symmetrical deposition is not observed in the peptide system due to backbone hydrogen bonding causing the peptide molecules to always form small aggregates in solution and therefore always deposit as multilayers, not monolayers, on the mica surfaces.

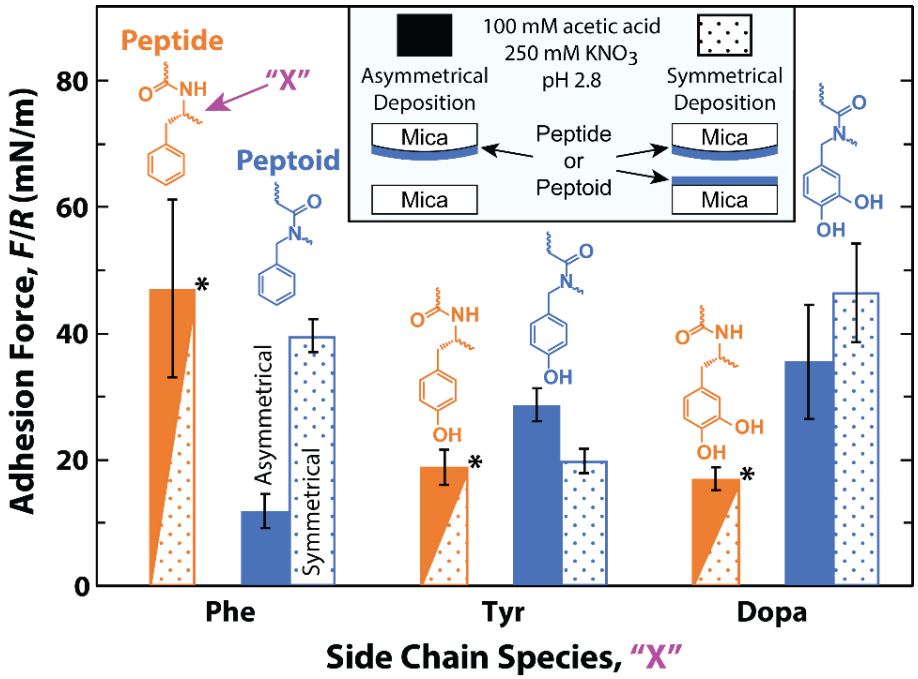

Figure 2.2 – Adhesive and cohesive interactions. A summary of the adhesive and cohesive forces between asymmetrically (solid bars) and symmetrically (dotted bars) deposited peptide (orange) and peptoid (blue) films on mica surfaces using the SFA. Bars indicate standard deviations. A schematic of the opposing mica surfaces for both deposition conditions is shown in the inset along with the background solution conditions. It was determined in the previous study* with peptide molecules that all forces measured were due to cohesive interactions, regardless of deposition method, therefore the solid and dotted bars for the peptide studies overlap. The aromatic residue present in each peptide/peptoid molecule is illustrated above each set of bars. *Adapted with permission from Gebbie *et al.* [16].

Conversely, for the Dopa peptoid, the film deposition symmetry has little effect on the measured forces due to the availability of strong interactions (surface and intermolecular hydrogen bonding, surface metal chelation, cation-π bonding, etc.) for either symmetry (Figure 2.5C,D). To explain the differences between the strong cohesive interactions measured in the Dopa peptoid system and the weaker cohesive interactions measured in the Dopa peptide system, we invoke the idea that backbone hydrogen bonding with the Dopa side chains in the peptide system disrupts those molecules' ability to form intermolecular bidentate hydrogen bonds and bridging metal coordination bonds with the opposing mica surface. Though the thermodynamic equilibrium bonding structure might necessitate the formation of these stronger bonds in both the peptide and peptoid system, the backbone

hydrogen bonding creates an additional kinetic barrier which may cause equilibration timescales of days to weeks.

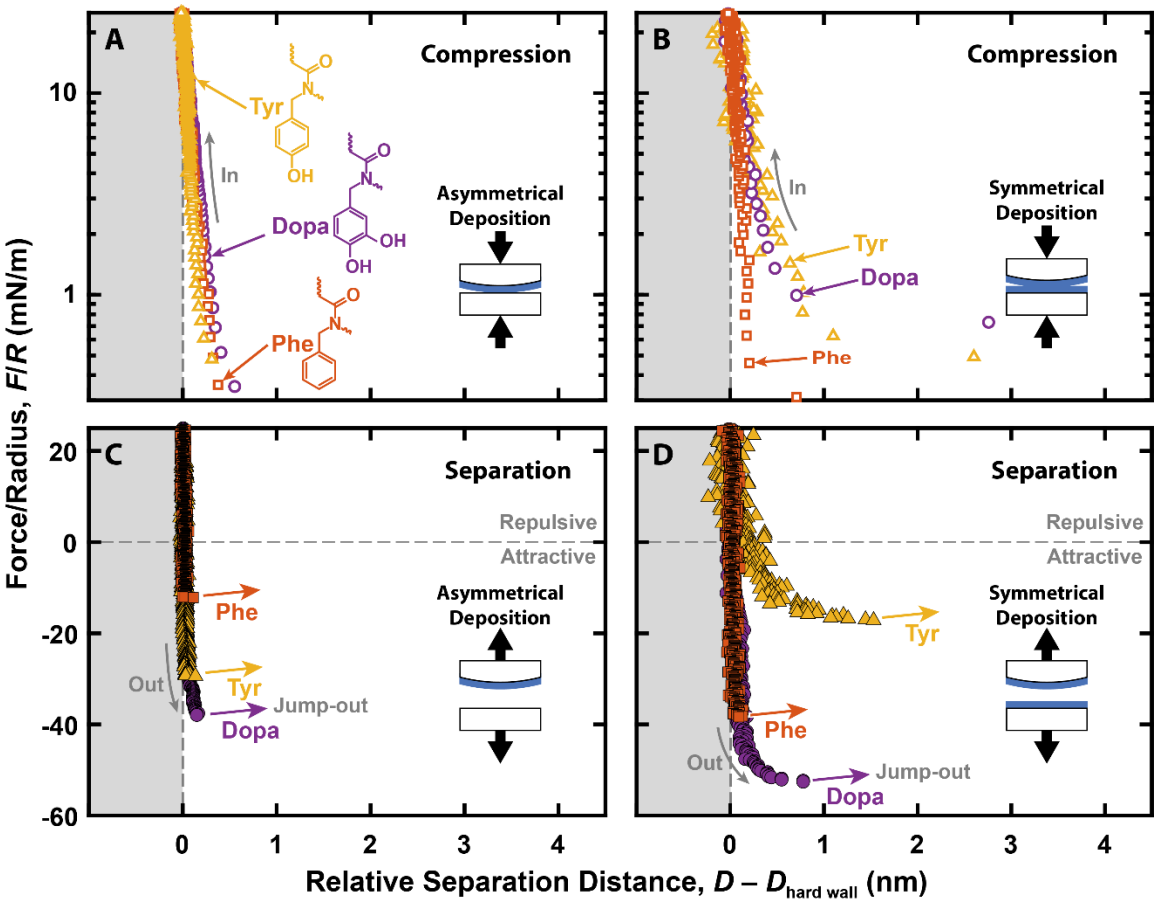

Figure 2.3 – Representative force curves for the peptoid molecules reveal low compressibility and low hydration. Force vs. distance profiles for Phe, Tyr, and Dopa peptoids deposited both A,C) asymmetrically and B,D) symmetrically between mica surfaces. Due to the nature of the peptoid deposition, absolute peptoid film thicknesses, $D_{\text{hard wall}}$, cannot be accurately calculated, therefore relative distances, $D - D_{\text{hard wall}}$ to directly compare their features near maximum compression, which are still meaningful. The uncertainty in the peptoid hard walls across all experiments, and valid for panels A-D, is illustrated by the red horizontal error bar in panel B. The compression curves (A,B) are represented with a log scale on the ordinate axis to highlight exponential features reminiscent of double-layer and hydration decay lengths.

Finally, the slight difference in the Tyr peptoid's adhesive and cohesive interactions can be explained by the notion that Tyr will be less likely to displace surface-bound Lys in these molecules relative to Dopa, therefore leading to a larger amount of Tyr-mica (vs. Dopa-mica and Lys-mica) interactions in the adhesive/asymmetrical system. The symmetrical

peptoid experiments, which exhibit cohesive failure, are in good agreement with the cohesive forces measured for analogous peptides.

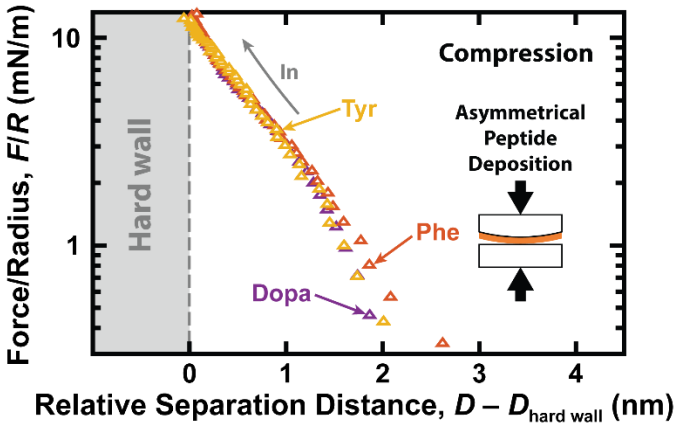

Figure 2.4 - Compression force vs. distance profiles of asymmetrically-deposited peptide analogs adapted from [16].

In addition to the values for the adhesive/cohesive forces, on compression, the force vs. distance profiles ($F(D)/R$) for the peptoid films reveal that the deposited layers are minimally compressible. Though the deposition technique, discussed further in the Methods section, requires that the mica surfaces be removed from the SFA, thus eliminating the ability to obtain accurate measurements for the films' hard walls (the maximally compressed film thicknesses), the relative behavior of the films while in compression is still accurate. Representative compression runs for each of the three peptoids are depicted in Figure 2.3A,B with their hard walls shifted in order to more clearly make comparisons between the shapes of the profiles. The slopes of the three curves for asymmetrically deposited peptoid films and nearly identical. The slopes of these curves are also smaller than those measured for the peptide films by Gebbie *et al.* [16] (Reproduced in Figure 2.4). This suggests that the peptoid films form more compact, less hydrated layers than their peptide counterparts. The symmetrically deposited peptoid films are slightly more compressible (Figure 2.3B) due to the larger layers of peptoid material with the Tyr and Dopa films showing the largest

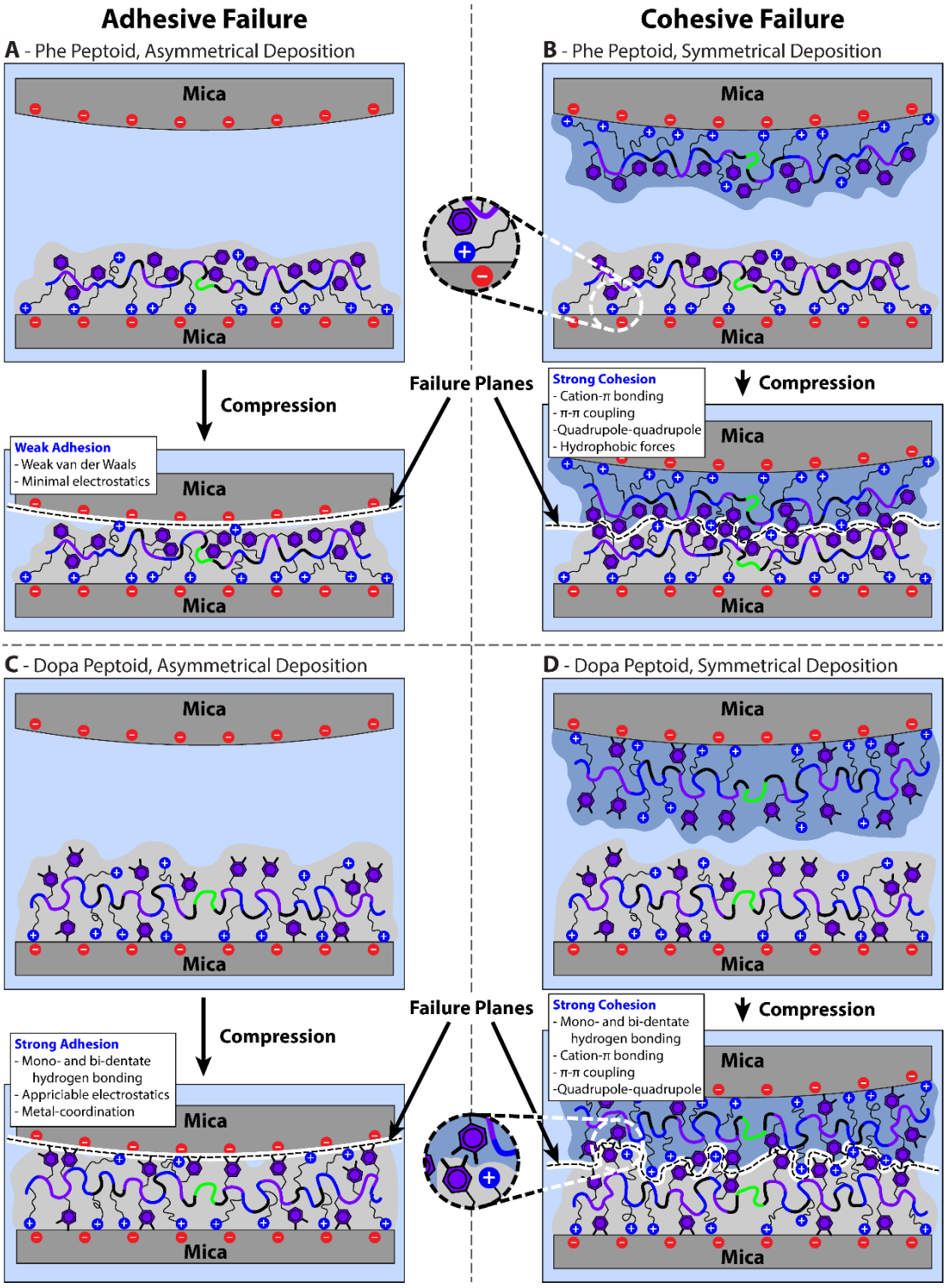

Figure 2.5 – Peptoid adhesion vs. cohesion schematics. Schematic representations of deposited peptoid films before and after compression for A) asymmetrical deposition of the Phe peptoid, B) symmetrical deposition of the Phe peptoid, C) asymmetrical deposition of the Dopa peptoid, D) symmetrical deposition of the Dopa peptoid. In all cases, asymmetrical deposition allows for adhesive failure and symmetrical deposition allows for cohesive failure. Failure planes are indicated by black dashed lines overlaid onto solid white lines. The "boundaries" of each peptoid molecule are indicated with either blue or gray shaded regions. The important interactions at each failure plan are indicated in the white boxes above each 'compressed' pair of surfaces.

changes. Representative separation/decompression runs for the same molecules are also shown in Figure 2.3C,D. The separation curves show small amounts of bridging between the surfaces before separation, which is common for polymeric molecules.

2.3.3 Effect of ionic strength on Dopa peptoid adhesion

The Dopa peptoids, which, due to potential Dopa-Dopa hydrogen bonding, may be most likely to form aggregates in solution, and therefore deposit as multilayers, require more careful consideration to determine that the asymmetrically deposited films fail adhesively. One way to further test this hypothesis is to expose the Dopa films to solutions of constant pH but varying ionic strength, thus increasing electrostatic screening. If the Dopa peptoids fail cohesively, it is likely that the cohesive forces are largely due to cation-π interactions, which, similar to other Coulombic interactions, should quickly weaken with increasing ionic strength [21]. Figure 2.6 shows the dependence of the Dopa peptoid adhesion force on ionic strength. In these experiments, the Dopa peptoid was deposited using a 0 mM KNO_3 solution and then the concentration of KNO_3 was successively increased by flushing the intervening capillary between the mica surfaces with 3-5 ml of peptoid-free solution at the new KNO_3 concentration. The films were allowed to equilibrate for > 30 min after each new KNO_3 concentration. Due to the Dopa peptoid's remarkably similar adhesive strength to the adhesive strength of bare mica surfaces at 0 mM KNO_3, the adhesion of bare mica at all salt concentrations was also measured for comparison. The data are also plotted normalized by the bare mica adhesion force at 0 mM KNO_3 to minimize the effect of geometrical differences on adhesion strength between the contact points. It can be seen that the adhesive performance of the Dopa peptoid between mica surfaces decreases much slower than the adhesion between bare mica surfaces, reaching about 50% of its 0 mM KNO_3 value when

finally equilibrated at 250 mM KNO_3. This decrease may be due to both material loss due to subsequent flushes of new salt solution as well as the decrease of Lys-mica bridging interactions at higher salt concentrations. This qualitative trend suggests that the adhesion is a result of more than just Coulombic interactions, such as Dopa-Dopa hydrogen bonding and Dopa-surface metal coordination, leading us to conclude that even the Dopa peptoid failure is adhesive.

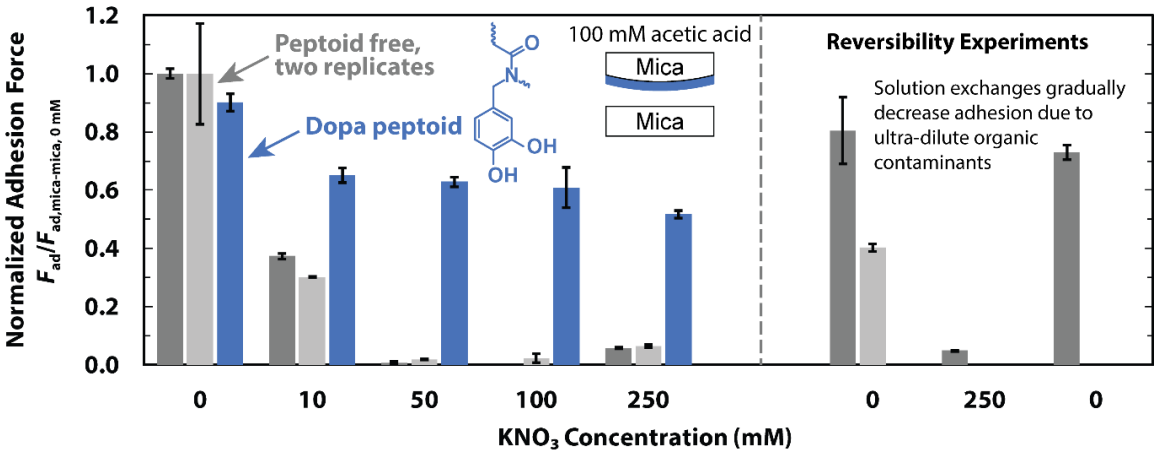

Figure 2.6 – Effect of ionic strength on Dopa peptoid adhesion. Adhesion forces for asymmetrically deposited Dopa peptoid films in 100 mM acetic acid and 0, 10, 50, 100, and 250 mM $KN0_3$ (blue bars) compared to the adhesion forces for peptoid-free mica surfaces at the same conditions (both sets of gray bars). From left to right, experiments of the same color bars are chronological, with the solution being exchanged between each set of measurements. In each case, the measured F_{ad} is normalized by the force of adhesion for the bare mica surfaces (before peptoid deposition) in 100 mM acetic acid and 0 mM KNO_3. The 'Reversibility Experiments' demonstrate that partial recovery of the 0 mM KNO_3 bare-mica adhesion is possible over multiple cycles between high and low salt conditions.

2.4 Conclusions

We have demonstrated that the wet adhesion and cohesion of peptoid analogues of mussel-inspired peptides is comparable to the cohesive strength of the peptide molecules as well as the mussel adhesive proteins from which they are derived. Therefore, peptoid molecules may further add to the growing portfolio of molecules which have useful applications for wet adhesion. However, the mechanisms of film deposition and film failure

depend strongly on the backbone structure of these molecules. The lack of intermolecular aggregation in the peptoid molecules allows for monolayer deposition from dilute solutions, producing more well-defined, less hydrated adhesive films than their peptide analogues.

We have also shown that when the *adhesive* mode of failure can be well established for these peptoid molecules, the expected increasing trend in adhesive performance with increasing aromatic ring hydroxylation from Phe to Tyr to Dopa is observed.

Further, we show that though peptides may be classified as 'intrinsically disordered', the backbone chemistry and structure may still influence their molecular properties. If such backbone interactions are undesirable for a specific application, such as selective surface priming, peptoid molecules can be used to maintain side chain function without the complication of backbone interactions. Then, intermolecular ordering can be engineered through specific side-chain interactions to tailor a peptoid's structure based on a desired function.

2.5 Materials and Methods

2.5.1 Materials

All materials were purchased from Sigma Aldrich and used as received.

2.5.2 Peptoid Synthesis

2.5.2.1 Tfa protection of 4-hydroxybenzylamine

4-hydroxybenzylamine (25 g, 203 mmol) and triethylamine (85 mL, 609mmol) were added to methanol and stirred for 10 minutes for full dissolution. Methyl trifluoroacetate (52 g, 406mmol) was then slowly added over a period of 20 minutes, and the reaction mixture was stirred at room temperature overnight. The solvent was removed via rotary evaporation.

The residue was treated with 1N HCl (100 mL) and extracted with ethyl acetate (3x75 mL). The organic layer was washed with 1N HCl (100 mL), brine (100mL), dried over $MgSO_4$, filtered, and the solvent removed to afford a brown solid (40 g, 88%).

2.5.2.2 THP protection of Tfa-4-hydroxybenzylamine

Tfa-4-hydroxybenzylamine (40 g, 183 mmol) and PPTS (6.28g, 25mmol) were added to a 1000mL round bottom flask and dissolved with DCM (250mL). DHP (42.7g, 507.5 mmol) was added over a 20-minute period *via* an addition funnel. After 1 hour of stirring the reaction mixture at room temperature a white precipitate formed. The reaction was stirred over night at room temperature. The reaction mixture was cooled to -20^{o}C and the white, crystalline precipitate was removed by filtration and washed with cold DCM. and dried under high vacuum yielding the product as white crystals (30.6 g, 101 mmol, 55% yield).

2.5.2.3 Tfa-deprotection

Lithium hydroxide (2.75g, 57.5 mmol) dissolved in 100mL H_2O was added to a stirring solution of Tfa/THP protected 4-hydroxybenzylamine (17.5g, 57.7mmol) dissolved in THF (200mL) in a 1000 mL round bottom flask. The reaction was stirred for 3 hours, after which the THF was removed by rotary evaporation. Water (50 mL) was added, and the aqueous solution was extracted with ethyl acetate (3x100mL). The organic layers were combined, washed with water, dried over Na_2SO_4 and evaporated to give a yellow oil (9.54 g, 80%).

2.5.2.4 Mussel-inspired peptoid synthesis

Peptoids were synthesized using a Symphony X automated peptide synthesizer on a 50 μM scale using Rink amide resin (0.64mmol/g). Peptoid coupling was achieved according to published procedures [22]. Bromoacetlyation was achieved by treatment with

N,N'-diisopropylcarbodiimide (DIC) (0.8 M in DMF) and bromoacetic acid (0.8 M in DMF), and displacements by treatment with 1M amine concentration. Glycine and cysteine were incorporated using standard Fmoc solid-phase synthesis procedures [23]. Couplings were performed using a solution of Fmoc-protected amino acid (0.8 M in DMF) and DIC (0.8 M in DMF) for 20 minutes. The Fmoc protecting group was removed by treating the resing with a 20% piperidine solution in DMF for 10 minutes. The N-termini of oligomers were acetylated on resin by treatment with a solution of acetic anhydride (3 parts) and pyridine (2 parts) for 30 minutes. Peptoids were cleaved from the resin by treatment with 95:2.5:2.5 TFA/H_2O/triisopropylsilane for 30 minutes. Solvent was removed from cleaved peptoids using a Biotage V-10 evaporator, and the crude peptoids were dissolved in 5% acetonitrile. Purification was achieved using reverse-phase HPLC with a C18 semipreparative column at a flow rate of 10mL/min.

2.5.2.5 Peptoid modification

Mushroom tyrosinase (3,000 U mg-1) was purchased from Sigma-Aldrich. Peptoids were dimerized with disulfide linkages as described previously [16]. Monomers (1 mg) were dissolved in 0.1 M phosphate buffer (1mL, pH=7) and NaIO4 was added (10μL, 5mg mL-1). The solution was shaken for 20 minutes, filtered, and injected onto a reverse-phase HPLC using a C18 column and purified with a linear gradient of aqueous acetonitrile (5 – 70%). Protein elution was monitored at 280 nm and the peak fractions were analyzed by matrix-assisted laser desorption ionization mass spectrometry (MALDI-MS). MALDI-MS samples were prepared by mixing with saturated α-cyano-4-hydroxycinnamic acid in 50% aqueous acetonitrile, 0.1% trifluoroacetic acid.

The peptoid dimer containing the 4-hydroxybenzylamine submonomer (tyrosine mimic) was modified using mushroom tyrosinase to obtain a dopa containing peptoid. The peptoid containing the tyrosine mimic (1 mg) was dissolved in a 100mM phosphate/50mM borate buffer (1 mL, pH=7). Mushroom tyrosinase (0.3 mg) was added and the solution bubbled with oxygen for 4 hours, after which the reaction was stopped by the addition of glacial acetic acid (50μL). This solution was then filtered, purified by reverse-phase HPLC, and analyzed with MALDI-MS as described for the dimerization process. Fractions containing the most dopa residues(10-13) were frozen, lyophilized, and resuspended in 100 mM acetic acid (Sigma-Aldrich) buffer (pH = 2.5) to ~1 mg mL-1 and stored at -80°C°.

2.5.3 Surface Forces Apparatus Measurements

Standard SFA procedures were used to measure force vs. distance profiles, normalized by the contact radius ($F(D)/R$) as detailed in [24]. Briefly, after obtaining the dry mica thickness in air, one or both mica surfaces were removed from the SFA in a laminar flow cabinet and exposed to 3 ml of 250 mM KNO_3, 100 mM acetic acid (pH 2.5-2.8) solutions. Subsequently, 15 μL of a 1 mg/ml peptoid solution in 100 mM acetic acid was diluted into the 3 ml salt and the surfaces were allowed to incubate for 20-30 minutes. The surfaces were then flushed with generous amounts (5-10 mL) of peptoid-free salt solution and transferred back into the SFA, carefully kept wetted by a droplet of solution. These peptoid-coated mica surfaces (Figure 2.1C) were then brought into molecular contact at nanometers-per-second velocities, generating the ‘Compression’ curves in [FIG NUM]. After compression, the surfaces were retracted at nanometer-per-second velocities giving a total time in contact of around 5 minutes. During separation, the double cantilever springs (Figure 2.1C) progressively accumulate tensile stress until the surfaces finally abruptly jump apart to

distances > 500 nm. The jump distance multiplied by the cantilever spring constant, k, measures the force of adhesion (or cohesion), F_{ad}, between the surfaces. For comparison between experiments, F_{ad} is normalized by the measured contact radius of the interacting surfaces for each experiment. We do not further normalize F_{ad} to an adhesion energy using either the Derjaguin Approximation [21] or the Johnson-Kendall-Roberts (JKR) theory of adhesion [25] because of the mixed nature of the adhesive/cohesive modes of failure in these systems.

2.6 References

1. Lee, B.P., Messersmith, P.B., Israelachvili, J.N., Waite, J.H.: Mussel-Inspired Adhesives and Coatings. Annu Rev Mater Res. 41, 99–132 (2011)

2. Floriolli, von Langen J, Waite: Marine Surfaces and the Expression of Specific Byssal Adhesive Protein Variants in Mytilus. Mar. Biotechnol. (NY). 2, 352–363 (2000)

3. Hofman, A.H., van Hees, I.A., Yang, J., Kamperman, M.: Bioinspired Underwater Adhesives by Using the Supramolecular Toolbox. Adv. Mater. 30, 1704640 (2018)

4. Lee, H., Scherer, N.F., Messersmith, P.B.: Single-molecule mechanics of mussel adhesion. Proc. Natl. Acad. Sci. U. S. A. 103, 12999–13003 (2006)

5. Kord Forooshani, P., Lee, B.P.: Recent approaches in designing bioadhesive materials inspired by mussel adhesive protein. J. Polym. Sci. Part A Polym. Chem. 55, 9–33 (2017)

6. Kim, S., Faghihnejad, A., Lee, Y., Jho, Y., Zeng, H., Hwang, D.S.: Cation–π interaction in DOPA-deficient mussel adhesive protein mfp-1. J. Mater. Chem. B. 3, 738–743 (2014)

7. Das, S., Rodriguez, N.R.M., Wei, W., Waite, J.H., Israelachvili, J.N.: Peptide Length and Dopa Determine Iron-Mediated Cohesion of Mussel Foot Proteins. Adv. Funct. Mater. 25, 5840–5847 (2015)

8. Yu, J., Wei, W., Menyo, M.S., Masic, A., Waite, J.H., Israelachvili, J.N.: Adhesion of mussel foot protein-3 to TiO2 surfaces: The effect of pH. Biomacromolecules. 14, 1072–1077 (2013)

9. Martinez Rodriguez, N.R., Das, S., Kaufman, Y., Israelachvili, J.N., Waite, J.H.:

Interfacial pH during mussel adhesive plaque formation. Biofouling. 31, 221–227 (2015)

10. Lu, Q., Danner, E., Waite, J.H., Israelachvili, J.N., Zeng, H., Hwang, D.S.: Adhesion of mussel foot proteins to different substrate surfaces. J. R. Soc. Interface. 10, 20120759 (2013)

11. Levine, Z.A., Rapp, M. V, Wei, W., Mullen, R.G., Wu, C., Zerze, G.H., Mittal, J., Waite, J.H., Israelachvili, J.N., Shea, J.-E.: Surface force measurements and simulations of mussel-derived peptide adhesives on wet organic surfaces. Proc. Natl. Acad. Sci. 113, 4332–4337 (2016)

12. Wei, W., Yu, J., Gebbie, M.A., Tan, Y., Martinez Rodriguez, N.R., Israelachvili, J.N., Herbert Waite, J.: Bridging Adhesion of Mussel-Inspired Peptides: Role of Charge, Chain Length, and Surface Type.

13. Rapp, M. V, Maier, G.P., Dobbs, H.A., Higdon, N.J., Waite, J.H., Butler, A., Israelachvili, J.N.: Defining the Catechol-Cation Synergy for Enhanced Wet Adhesion to Mineral Surfaces. J. Am. Chem. Soc. 138, 9013–9016 (2016)

14. Yu, J., Kan, Y., Rapp, M., Danner, E., Wei, W., Das, S., Miller, D.R., Chen, Y., Waite, J.H., Israelachvili, J.N.: Adaptive hydrophobic and hydrophilic interactions of mussel foot proteins with organic thin films. Proc. Natl. Acad. Sci. 110, 15680–15685 (2013)

15. Hwang, D.S., Waite, J.H.: Three intrinsically unstructured mussel adhesive proteins, mfp-1, mfp-2, and mfp-3: analysis by circular dichroism. Protein Sci. 21, 1689–95 (2012)

16. Gebbie, M.A., Wei, W., Schrader, A.M., Cristiani, T.R., Dobbs, H.A., Idso, M., Chmelka, B.F., Waite, J.H., Israelachvili, J.N.: Tuning underwater adhesion with cation–π interactions. Nat. Chem. 9, 473–479 (2017)

17. Maier, G.P., Rapp, M. V., Waite, J.H., Israelachvili, J.N., Butler, A.: Adaptive Synergy Between Catechol and Lysine Promotes Wet Adhesion by Surface Salt Displacement. Science. 349, 628–631 (2015)

18. Kai Huang, †,‡, Cindy W. Wu, §, Tracy J. Sanborn, §, James A. Patch, §, Kent Kirshenbaum, ¶, Ronald N. Zuckermann, #, Annelise E. Barron, *,§ and, Ishwar Radhakrishnan*, †: A Threaded Loop Conformation Adopted by a Family of Peptoid Nonamers. (2006)

19. Stringer, J.R., Crapster, J.A., Guzei, I.A., Blackwell, H.E.: Extraordinarily Robust Polyproline Type I Peptoid Helices Generated via the Incorporation of α-Chiral Aromatic N -1-Naphthylethyl Side Chains. J. Am. Chem. Soc. 133, 15559–15567 (2011)

20. Vollrath, S.B.L., Hu, C., Bräse, S., Kirshenbaum, K.: Peptoid nanotubes: an oligomer

macrocycle that reversibly sequesters water via single-crystal-to-single-crystal transformations. Chem. Commun. 49, 2317 (2013)

21. Israelachvili, J.N.: Intermolecular and Surface Forces: Revised Third Edition. Academic Press (2011)

22. Olivier, G.K., Cho, A., Sanii, B., Connolly, M.D., Tran, H., Zuckermann, R.N.: Antibody-Mimetic Peptoid Nanosheets for Molecular Recognition. ACS Nano. 7, 9276–9286 (2013)

23. Fields, G. ed: Solid-Phase Peptide Synthesis, Volume 289. In: Methods in Enzymology. pp. 44–67. Academic Press, New York (1997)

24. Israelachvili, J., Min, Y., Akbulut, M., Alig, A., Carver, G., Greene, W., Kristiansen, K., Meyer, E., Pesika, N., Rosenberg, K., Zeng, H.: Recent advances in the surface forces apparatus (SFA) technique. Reports Prog. Phys. 73, 036601 (2010)

25. Johnson, K.L., Kendall, K., Roberts, A.D.: Surface Energy and the Contact of Elastic Solids. Proc. R. Soc. A Math. Phys. Eng. Sci. 324, 301–313 (1971)

3 Studying the toughening mechanisms of mussel-inspired iron-catechol complexes in dry epoxy networks

3.1 Toughening elastomers using mussel-inspired iron-catechol complexes

Adapted from: Filippidi, E., **Cristiani, T.R.**, Eisenbach, C.D., Waite, J.H., Israelachvili, J.N., Ahn, B.K., Valentine, M.T., ***Science*****.** 358, 502–505 **(2017)**
Supported by: United States Department of Energy Award Number: DE-FG02-87ER45331

3.1.1 Abstract

Materials often exhibit a trade-off between stiffness and extensibility; for example, strengthening elastomers by increasing their cross-link density leads to embrittlement and decreased toughness. Inspired by cuticles of marine mussel byssi, we circumvent this inherent trade-off by incorporating sacrificial, reversible iron-catechol cross-links into a dry, loosely cross-linked epoxy network. The iron-containing network exhibits 2-3 orders of magnitude increases in stiffness, tensile strength, and tensile toughness compared to its iron-free precursor while gaining recoverable hysteretic energy dissipation and maintaining its original extensibility. Compared to previous realizations of this chemistry in hydrogels, the dry nature of the network enables larger property enhancement due to the cooperative effects of both the increased cross-link density given by the reversible iron-catecholate complexes and the chain-restricting ionomeric nanodomains that they form.

3.1.2 Introduction

Despite demands for tough, high-modulus polymer materials, it remains difficult to develop strategies that increase their mechanical strength without sacrificing their maximum elongation and toughness. The traditional approach of incorporating fillers into polymers,

including nanofillers [1], results in a trade-off between stiffness and extensibility. Recent strategies, such as interpenetrating double/triple networks [2, 3], employ intricate network architectures to efficiently dissipate energy through the mechanically-induced rupture of one or more sacrificial networks. Alternatively, energy can be dissipated in single-network architectures by incorporating sliding [4] or sacrificial, reversible cross-links. Examples of the latter include metal coordination [5–7], hydrogen bonding [8], supramolecular systems [9], and ionic/Coulombic interactions [10]. Reversible bonding and interpenetrating networks have also been combined, resulting in property enhancements exceeding those of either individual strategy [7, 11]. However, to date, these improvements have been limited to soft, low elastic moduli dry networks, $E < 10$ MPa [2, 8] or to promising hydrated networks ($E = 35$ MPa, [7]).

Our strategy is inspired by the tough polymeric byssal threads used by marine mussels to secure themselves on surfaces to survive the wave-swept intertidal zone. The distal portions of the *M. californianus* and *M. galloprovincialis* mussel threads are comprised of cylindrical collagenous cores surrounded by proteinaceous cuticles, which are stiff and extensible, and partially recover after loading [12]. The cuticle's chemistry, which contains considerable coordination bonding between the abundant catecholic amino acid, 3,4-dihydroxyphenylalanine (Dopa), and iron (III) [13], has inspired numerous efforts [5, 14, 15] that demonstrate enhanced mechanical properties and control of dynamic bonding timescales, but have been limited to wet, soft systems such as hydrogels. However, the extended chains of hydrated systems prevent a combination of high stiffness and elongation. Furthermore, water weakens physical interactions that depend on close spatial proximity of

interacting groups, such as Coulombic attraction, coordinate bonding, or inter-chain friction, softening hydrated materials.

In contrast to previous studies, we present a dry polymeric system that uses these sacrificial metal coordination bonds alongside chemical cross-links resulting in a load-bearing network ($E \approx 184$ MPa) that does not trade off extensibility ($\varepsilon_{max} \approx 150\%$) for stiffness. The iron-catechol coordination bonds provide the additional benefit of being dynamic and spatially reconfigurable with bond strengths comparable to covalent bonds [16–18], resulting in a material with both high stiffness and toughness relative to similar networks lacking coordination bonds. The development of a dry polymer that is stiff yet extensible has the potential to substitute stiff but brittle polymers, especially in impact and torsion-related applications.

3.1.3 Results and discussion

To achieve networks of architecture and performance similar to the mussel byssal cuticle, a loosely cross-linked amorphous epoxy network with high catechol content (~14 mol% of starting constitutive units) was synthesized and subsequently treated with iron to form dynamic iron-catechol cross-links (Figure 3.1). The desired network topology was attained by reacting a short-chain bisepoxide (PEG-DE), a monoepoxide carrying a triethylsilyl-protected catechol group (CAT), and a tetrafunctional diamine cross-linker (DAB). Given the stoichiometry of the starting materials (Figure 3.1A, Table 3.1), particularly the ratio of monoepoxide to bisepoxide, a highly-branched, slightly-crosslinked network is expected [19] (see Section 3.1.6.3). Networks of similar topology but different catechol content were obtained by replacing some or all of the CAT monomers by (2,3-

epoxypropyl)benzene (BENZ), which is unable to coordinate iron. Curing was performed at a low enough temperature (60 °C) to avoid premature deprotection of CAT. High epoxy conversion was confirmed by Fourier-transform infrared spectroscopy (Figure 3.2) and gelation was confirmed by rheology (Figure 3.3).

Table 3.1 - Polymer Network Compositions. Monomer composition of reaction mixtures for each cured network. Tetrahydrofuran (4 wt% of neat monomers) was added as a compatibilizer to each reaction mixture.

Network 1 – PEG-DE:CAT:DAB = 1.00:1.54:0.88 – "Protected, 100% CAT"				
	PEG-DE	**DAB**	**CAT**	
Mass Percent	42.2	6.6	51.2	
Mole Percent	29.2	25.8	45.0	
Mole Percent Constitutive Units	77.8	8.1	14.1	
Network 2 – PEG-DE:BENZ:DAB = 1.00:1.54:0.88 – "100% BENZ"				
	PEG-DE	**DAB**	**(2,3-epoxypropyl)benzene**	
Mass Percent	63.8	9.9	26.3	
Mole Percent	29.2	25.8	45.0	
Mole Percent Constitutive Units	77.8	8.1	14.1	
Network 3 – PEG-DE:CAT:BENZ:DAB = 1.00:0.77:0.77:0.88 – "Protected, 50% BENZ"				
	PEG-DE	**DAB**	**(2,3-epoxypropyl)benzene**	**CAT**
Mass Percent	50.8	7.9	10.5	30.8
Mole Percent	29.2	25.8	22.5	22.5
Mole Percent Constitutive Units	77.8	8.1	7.05	7.05
Network 4 – PEG-DE:DAB = 1.00:0.50 – "No aromatic species"				
	PEG-DE	**DAB**		
Mass Percent	91.9	8.1		
Mole Percent	66.7	33.3		
Mole Percent Constitutive Units	94.5	5.5		

After curing, the protected network was swollen in aqueous solutions, first to deprotect the CAT groups, and second to introduce iron, forming the iron-catechol cross-links (Figure 3.1B-D). To prevent undesirable cross-links due to catechol-catechol oxidative coupling, and thus establish a well-defined network structure, side reactions that deprotected-catechols may undergo during iron complexation were avoided by modifying the protocol

developed by Fullenkamp *et al.* [20]. In our study, deprotection was performed in dilute HCl (pH 2.5) under an argon atmosphere to avoid catechol oxidation. Both Fe^{3+}-mediated catechol oxidation (Figure 3.4) and Fe^{3+} hydroxide formation were avoided by introducing the swollen deprotected networks to Fe^{3+} in bicine/NaOH-buffered solutions of highly-soluble ferric nitrate nonahydrate at pH 7.5. In the Fe^{3+}-catecholate equilibrium, this pH favors the formation of bis-catecholate complexes in particular (Figure 3.4), as opposed to mono-catecholate complexes [5]. Possible counterions to the bis- and tris- catecholate complexes include Na^{+}, excess Fe^{3+}, and charged ammonium groups formed from the diamine crosslinker; any mono-complexes present are likely neutralized with nitrate. Lastly, iron coordination is much faster than catechol oxidation, preventing catechol covalent coupling [20]. Furthermore, bicine weakly chelates Fe^{3+}, protecting it from hydroxylation.

The added iron is uniformly distributed (5-8 wt%, as measured by inductively-coupled plasma atomic emission spectroscopy, ICP-AES and energy dispersive X-ray spectroscopy,(EDX, Figure 3.5B and Figure 3.6) and complexed with catechols (confocal resonance Raman spectroscopy, Figure 3.5A). In particular, the Raman peak at 512 cm^{-1} has been associated with increased bis- and tris-complexation relative to mono-complexation [5, 13], indicating that many coordinate bonds act as additional cross-linking points. The same cross-linking strategy is used by the mussel [13].

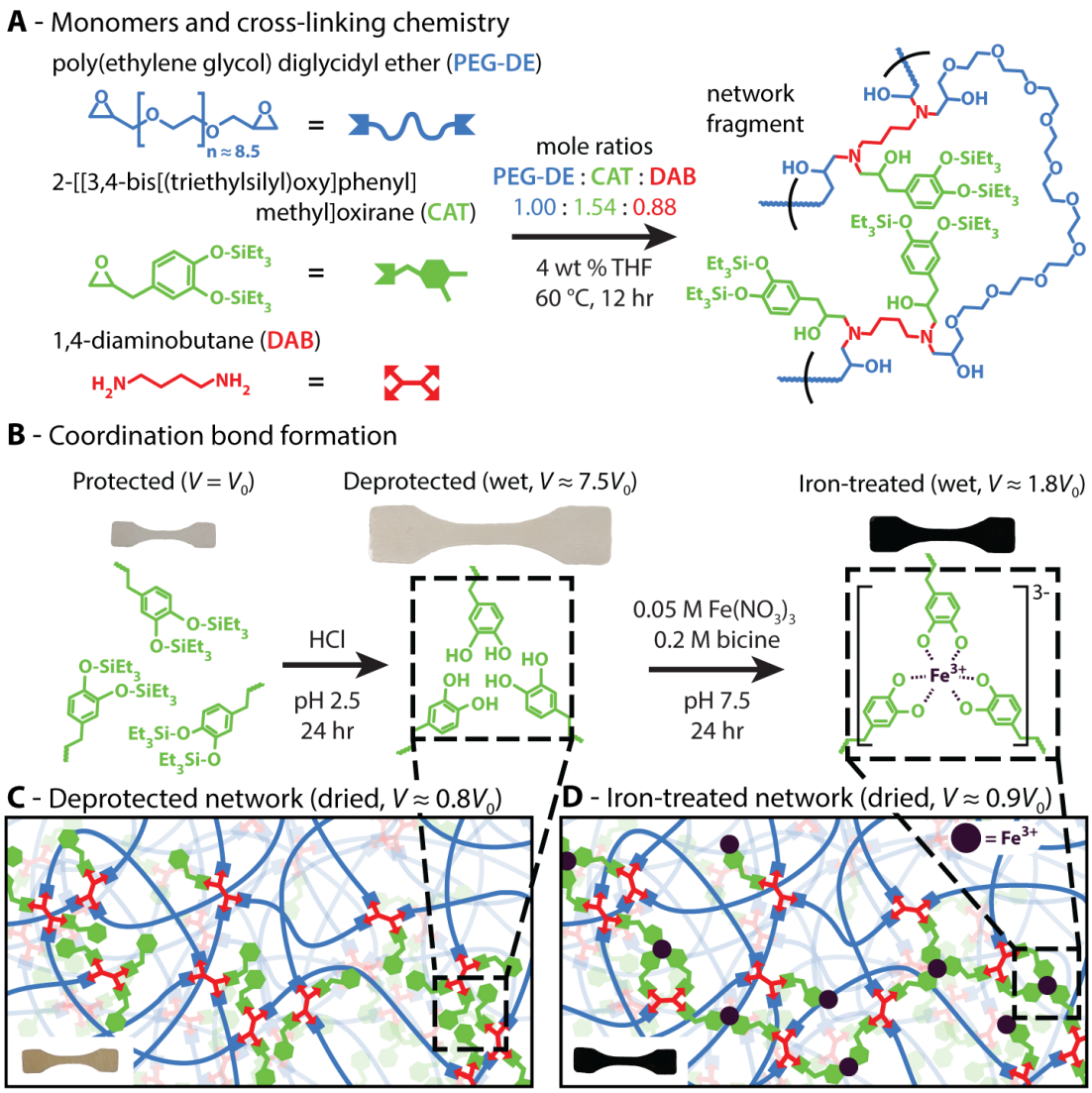

Figure 3.1 - Monomer and network-formation chemistry. (A) The monomers, mole ratios and curing conditions used in the synthesis of protected catechol-containing networks, and a schematic network fragment showing a CAT cluster. (B) A scheme of the cleavage of the silyl protective groups and subsequent iron complex formation, and a depiction of the swelling of a test specimen during the process. (C) and (D) Schematics of the network structure before (C) and after (D) iron treatment, illustrating mono-, bis-, and tris-complexation.

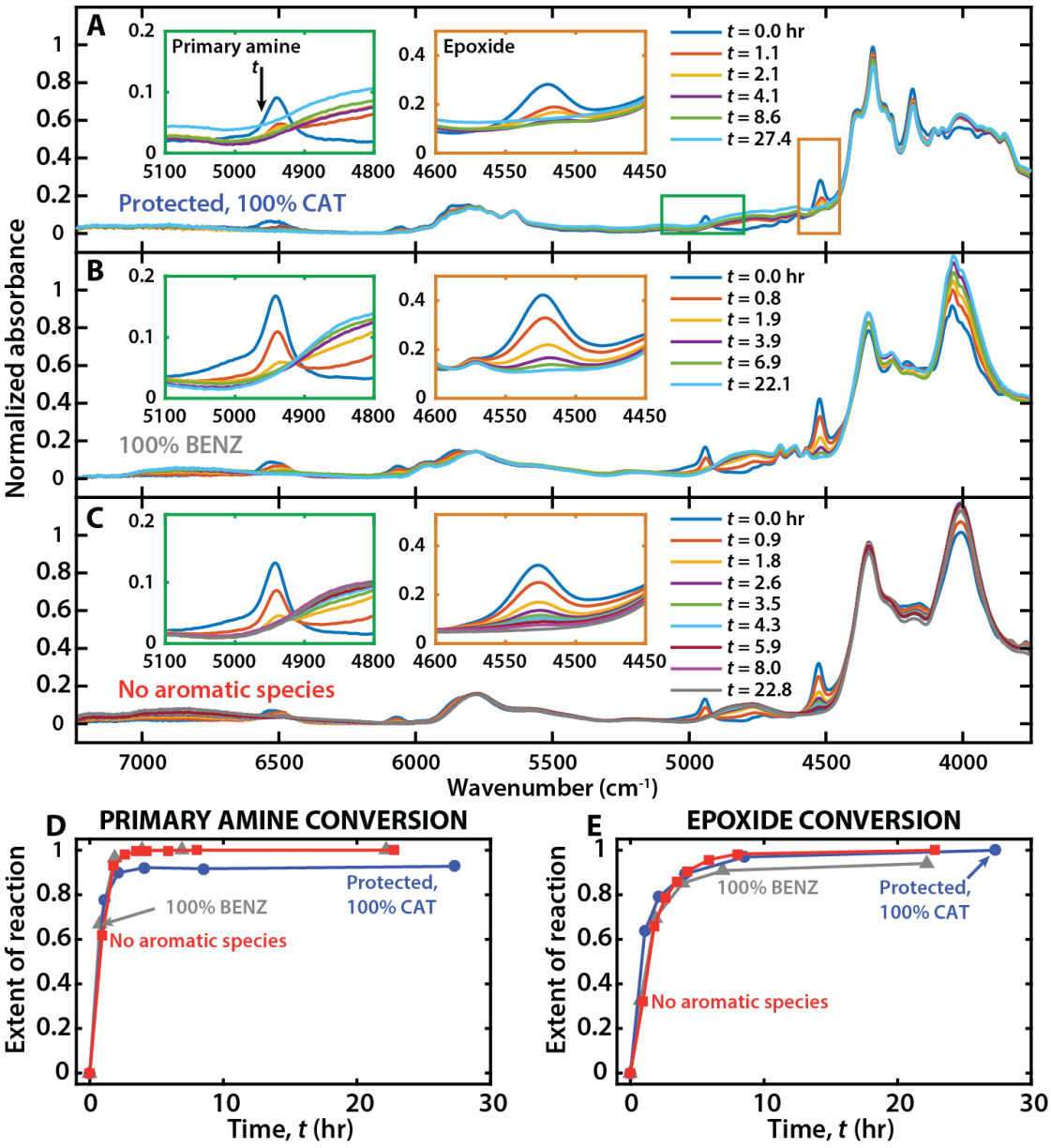

Figure 3.2 - Fourier transform infrared spectroscopy of benzyl- and catechol-containing networks. (A-C) FTIR spectra taken at different times during the curing of the (A) protected, 100% catechol network (Network 1), (B) the 100% benzyl network (Network 2), and (C) a network containing no aromatic species (Network 4). The spectra were normalized to an invariant band centered at approximately 1960 cm^{-1} (not shown), which is a skeletal band corresponding to the PEG backbone. A combination band of NH stretching and bending from the primary amines is centered at 4940 cm^{-1} and has been enlarged in the green insets (left). The combination band of the second overtone of the epoxide ring stretching and the fundamental CH stretching is centered at 4520 cm^{-1} and has been enlarged in the orange insets (right). The bands centered around 6500 cm^{-1} are due to both primary and secondary amines and cannot easily be used quantitatively. However, with increasing conversion, these bands exhibit a shift towards lower wavenumbers before disappearing, an indication of conversion of both primary amine to secondary amine and secondary amine to tertiary amine. (D, E) Conversion of (D) primary amine groups and (E) epoxide groups vs. curing time for all three networks (Network 1, red squares; Network 2, gray triangles; Network 4, blue circles).

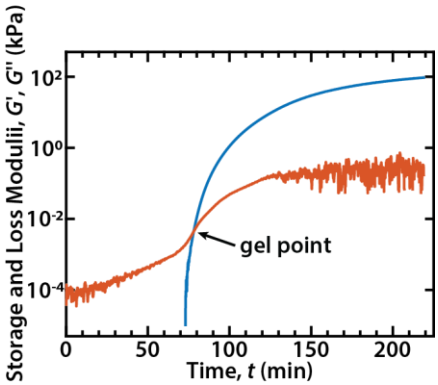

Figure 3.3 - Bulk, oscillatory rheology demonstrates gelation. Measurement of storage (G') and loss (G'') moduli during curing at 60 °C, starting from the liquid monomer mixture of Network 1. The cross-over of G' and G'' is indicative of the gelation and corresponds to an epoxy conversion of 67% and primary amine conversion of 80% (Figure 3.2D-E) as monitored by IR spectroscopy. This measurement suggests a large difference in the reactivity of the PEG-DE epoxide groups and the CAT epoxide groups [19]. According to Cheng *et al.*, for a monoepoxide:bisepoxide ratio of $s = 0.77$, a gel-point epoxide conversion of 67% would correspond to a ratio of activities of monoepoxide:bisepoxide, $\lambda \approx 0.2$. This value for λ is reasonable, given the steric bulk, and therefore reduced mobility, of the CAT moiety. The storage modulus after complete curing ($t >$ 220 min), $G'_{max} \approx 100$ kPa, is within the appropriate order of magnitude as compared to the tensile modulus of the protected Network 1, $E_{prot} = 240$ kPa, given the expression $E = (2G')(1+\nu)$.

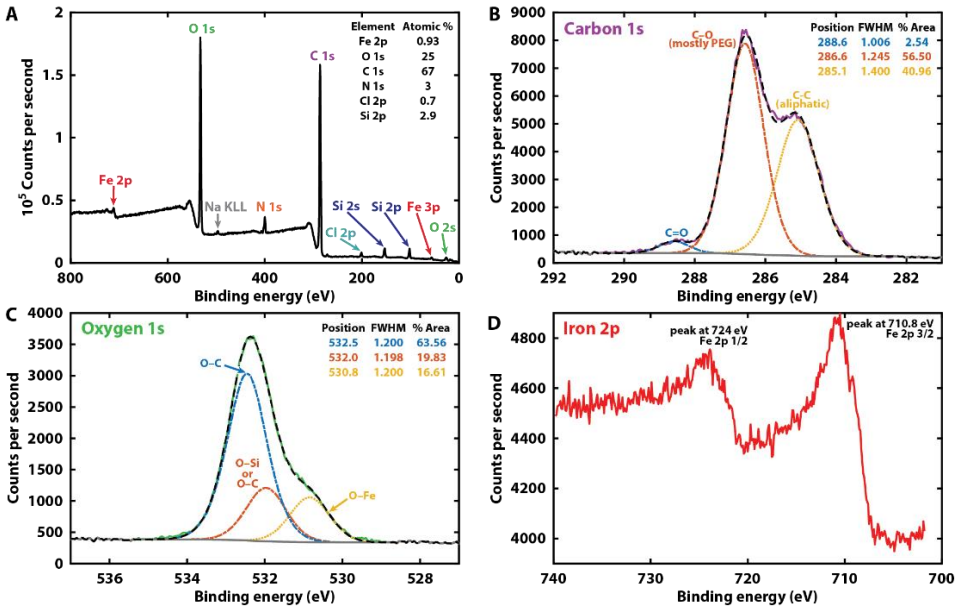

Figure 3.4 - X-ray photoelectron spectroscopy (XPS) scans. (A) Survey scan (B) Carbon shifts. The largest peak is attributed to the PEG C-O binding. (C) Oxygen shifts. Corresponding to the largest carbon peak, we attribute the largest oxygen peak to the PEG O-C binding. The lower binding energy shift is attributed to O-Fe binding and in particular C-O-Fe binding. Fe-O-Fe binding according to the chemistry proposed in [21] is not supported by the O shifts as it should occur at lower binding energies than the O-Fe peak. The area of the C-O-Fe binding curve corresponds to 16.61% of the total atomic percentage of oxygen, so 4.46% of total atomic mass. From the survey scan, the iron is 0.93% of total atomic mass, therefore we can estimate 4.46 non-water oxygen atoms per iron atom, supporting mixed bis- and tris- iron-catechol coordination. (D) Iron shifts. The low content of iron leads to a low signal-to-noise ratio. However, comparison of the peak in our data at 710.8 eV with tabulated values which give the Fe2p3/2 for Fe_2O_3 at 710.8 eV versus 709.6 eV for FeO, supports the presence of Fe(III) versus Fe(II).

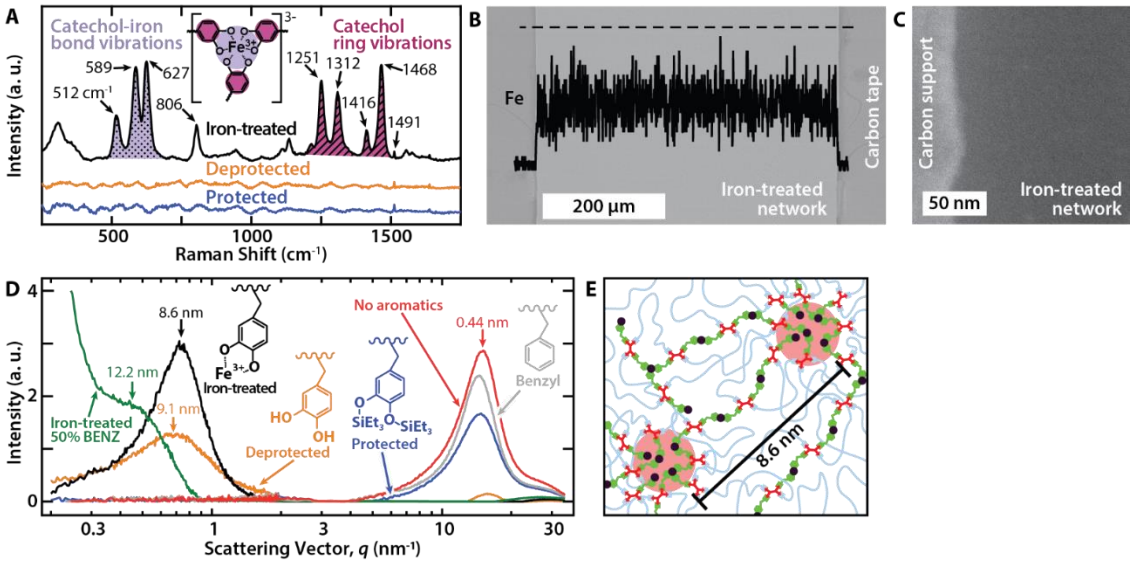

Figure 3.5 - Characterizing network structure and chemistry in the presence of iron. (A) Background-subtracted resonance Raman spectra of protected (blue), deprotected (orange), and iron-treated (black) catechol-containing networks. Both the signal enhancement and characteristic shifts in the shaded regions from 500-700 cm^{-1} (purple, dotted) and 1200-1500 cm^{-1} (magenta, hashed) confirm iron-catechol coordination. (B) Backscattered SEM micrograph (background image) and EDX (Fe K) line scan (black curve) along the dashed line of a cross-section of a typical sample used for tensile tests. Both show uniform iron diffusion (see also Figure 3.6). (C) High angle annular dark-field STEM shows no iron aggregates. (D) SAXS/WAXS of the dry networks. Networks with benzyl (gray), protected catechol (blue), and no aromatic (red) pendant groups show no features in the SAXS regime ($0.1 < q < 2$ nm^{-1}). WAXS peaks (amorphous halo: 0.4197 ± 0.0003 nm) result from inter-atom matrix scattering. Iron-treated (black) and deprotected (orange) networks have emergent peaks (correlation distances) at 8.57 ± 0.02 and 9.14 ± 0.04 nm corresponding to the development of iron-coordinated and hydrogen-bonded catechol clusters, respectively. (E) Schematic of ionomer-like Fe^{3+}-catechol clusters.

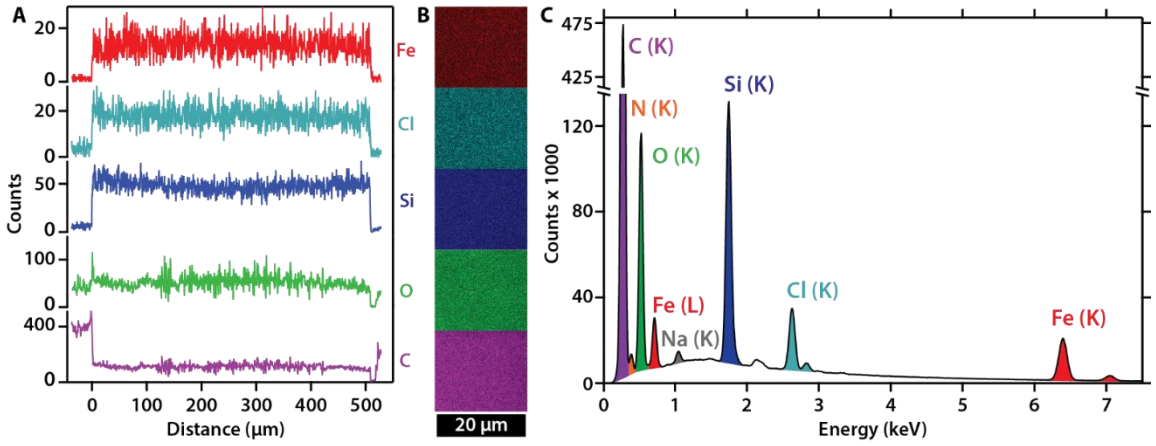

Figure 3.6 - Energy dispersive X-ray (EDX) scans of a sample cross-section. (A) Line scans across the sample thickness of all elements of interest: Fe, Cl, Si, O and C. The sample used and scan line measured are shown in Fig. 2B. All species show uniform distribution along the measured line-scan. (B) Area scans of the nearby regions confirm uniformity. (C) Spectrum corresponding to the area scans collected in (B) showing the signal and the Bremsstrahlung radiation background.

The resulting networks, before and after iron-treatment, are amorphous, exhibiting broad glass transitions between −100 and +50 °C, as measured by differential scanning calorimetry (DSC) (Figure 3.7). The amorphous state was further corroborated by the lack of crystalline peaks measured by X-ray diffraction Figure 3.5D), which also rules out the formation of iron oxide precipitates. In the wide-angle scattering regime, where such peaks would be expected, only an amorphous halo resulting from matrix interchain scattering is observed (0.42 nm). Iron precipitation was not detected by EDX at the microscale, nor at the nanoscale (down to ~2 nm) probed with scanning transmission electron microscopy (STEM-HAADF – a technique with high atomic number sensitivity) (Figure 3.5B, C). As such, any micro- or nano-filler contribution to the mechanical properties of the network is excluded.

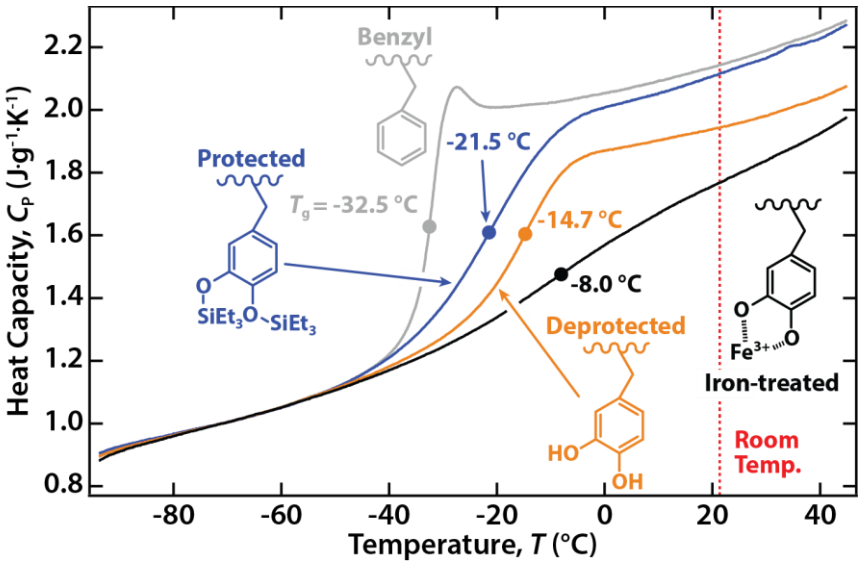

Figure 3.7 - Differential scanning calorimetry (DSC) of benzyl, protected, deprotected and iron-treated samples. Specific heat capacity as a function of temperature. The iron-treated curve is arbitrarily shifted in C_p to illustrate both the broadening and the ΔC_p associated with the glass transition. All samples have T_g values (filled circles) below room temperature.

However, small-angle X-ray scattering (SAXS, Figure 3.5D) shows broad peaks for the deprotected and iron-treated networks. The corresponding distances must be attributed to the correlation distance, *r*, between electron-rich, catechol-rich hydrogen-bound domains in the deprotected network (r_{depro} = 9.14 ± 0.04 nm) and iron-rich iron-catechol domains in the

iron-treated network ($r_{100\%}$ = 8.57 ± 0.02 nm, Figure 3.5E). Similar broad amorphous peaks have been observed in ionomers and attributed to their ionic domains of liquid-like order [22, 23]. In these domains, Fe^{3+} complexed with two or three catechols can be induced to exchange ligands by external energy contributions, such as mechanical stress. These domains also restrict network mobility compared to the iron-free networks. Reducing the number density of these domains by halving the catechol-content (50% BENZ network), and thus doubling the average chain length between iron-catechol clusters, *n*, shifts the ionomer peak to a longer correlation distance ($r_{50\%}$ = 12.2 ± 0.08 nm), as expected from $\langle r^2_{50\%}\rangle = (n_{50\%}/n_{100\%})\langle r^2_{100\%}\rangle$, with $n_{50\%} = 2n_{100\%}$ (see Section 3.1.6.2).

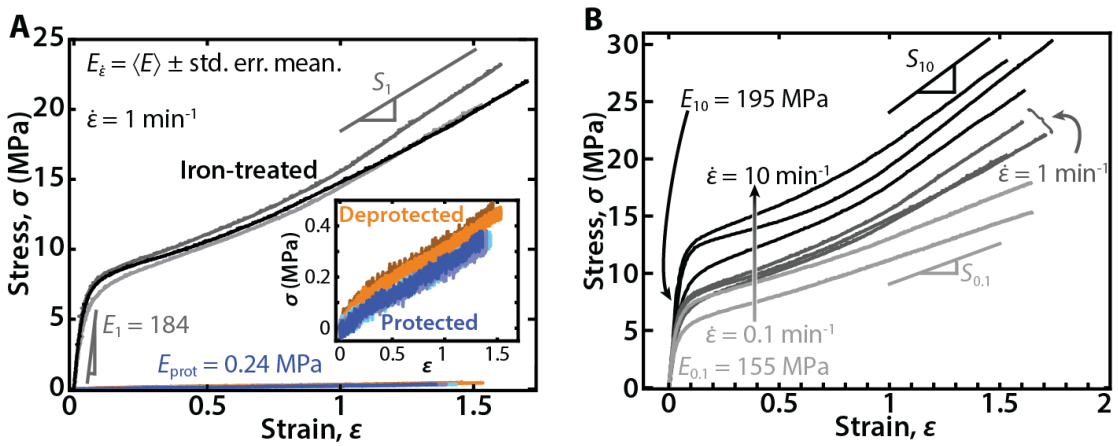

Figure 3.8 - Uniaxial tensile tests. (A) Engineering stress as a function of strain of protected (blue), deprotected (orange) and iron-treated samples (grey); strain rate, $\dot\varepsilon$ = 1 min^{-1}. (B) Strain-rate dependence ($\dot\varepsilon$ = 0.1, 1, and 10 min^{-1}) of iron-treated samples.

Uniaxial tensile tests (Figure 3.8A, D638 ASTM standard) show the striking increase in stiffness and toughness of the iron-treated networks compared with the protected and deprotected networks, without loss of maximum extensibility. Protected samples are perfectly linearly elastic (E_{prot} = 0.240 ± 0.007 MPa). Deprotection causes doubling of the elastic modulus (E_{depro} = 0.45 ± 0.02 MPa) and the emergence of a yield point at strain $\varepsilon \approx$ 0.2, both of which may be attributed to catechol-catechol weak reversible hydrogen bonds

and preferential segregation of catechols to domains (as supported by SAXS). Post-yielding, the linear $\sigma(\varepsilon)$ segment has slope S_{depro} = 0.253 ± 0.003 MPa, converging to the stiffness E_{prot}, as both hydrogen bonds and domain structure are disrupted. After iron-treatment, the iron-catechol coordination bonds, which have significantly higher dissociation energies than hydrogen bonds, increase the energetic barrier for a chain to detach from a domain. The net effect is an extraordinarily high 770-fold increase in elastic modulus (E_1 = 184 ± 14 MPa), a 58-fold increase in tensile strength from σ_{prot} = 0.378 ± 0.002 to σ_1 = 21.9 ± 0.8 MPa, and a corresponding 76-fold increase in the yield stress from 0.084 ± 0.006 to 6.4 ± 0.4 MPa. Accordingly, there is a 92-fold increase in tensile toughness (energy density) from 0.244 ± 0.007 to 22 ± 2 MJ/m^3. As expected for thermoset polymers [24], the yield stress increases with increasing strain rate (Figure 3.8B). Exposure to humidity (reversible) or oxidative conditions (irreversible) reduce both the stiffness and extensibility of the network (Figure 3.9).

Though part of the increase in the iron-treated network's stiffness at room temperature could be attributed to the increase of T_g observed by DSC (Figure 3.7), dynamic mechanical analysis (DMA) shows only a small decrease in storage modulus from E'_{iron} = 250 MPa at T = 22 °C (N = 1) to E'_{iron} = 179 MPa at 28.7 °C, where $\Delta T_{iron} = \Delta T_{depro} = T_{room} - T_{g,depro}$ = 36.7 °C (Figure 3.10). Furthermore, increased temperature causes no measurable morphological changes in the static ionomer domains (SAXS, Figure 3.11), implying no structural rearrangements. Thus, the increase in the breath of the glass transition is perhaps more influential than the value of T_g and reflects an overlap of various relaxation processes due to the emergent dynamic bonds and ionomeric domains.

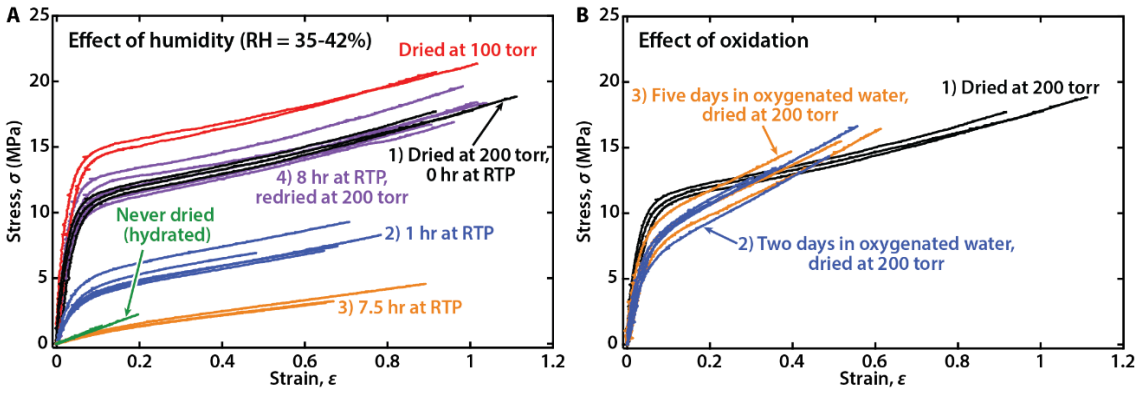

Figure 3.9 - Effect of relative humidity and oxidative conditions on the tensile properties of the iron-treated material pulled at a strain rate of 1 min^{-1}. **(A)** Wet iron-treated specimens (green) exhibit a linear stress-strain relation (E_{wet} = 5.7 ± 0.4 MPa, N = 4) and a reduction in maximum strain to fracture (~20%) as one would expect for a hydrogel, compared to specimens dried at 200 torr (black, E = 141 ± 35 MPa, N = 3). The hydrophilic nature of PEG implies fully hydrated chains, constricted only by the covalent and hydrated iron-catechol complexes. Exposure to ambient conditions, T = 21.5 °C and relative humidity, RH = 41%, for 1 hr causes a significant decrease in mechanical performance (blue). The Young's modulus drops to 39 ± 7 MPa (N = 5) and the maximum strain to fracture is reduced. The effect can be attributed to three factors: (i) water slightly shifts the iron(III)-catechol equilibrium away from complex formation, effectively reducing the number of complexes by an exceedingly small amount; (ii) water acts a plasticizer and reduces inter-chain interactions, and, most importantly, (iii) water causes increased charge screening of the coordination complexes with the ionomeric domains. The effect is exacerbated after longer exposure (7.5 hr) to ambient conditions (orange, E = 5.1 ± 1.2 MPa, N = 4). However, re-drying the exposed samples at the same pressure (purple) largely removes all humidity effects, recovering both the modulus (E = 118 ± 17 MPa, N = 5) and the maximum strain at fracture to their original values, within error. This recovery strongly suggests that humidity only imparts physical changes in the network (not chemical changes, such as catechol oxidation). Drying the network at lower pressure (100 torr, red curves) with no exposure to ambient conditions further increases the network's modulus to E = 256 ± 63 MPa, N = 2, by removing even more water. (B) The effect of exposing the iron-treated specimens to non-degassed water accelerates the oxidative cross-linking of catechol. For the oxidized samples, there is a small decrease in the initial modulus, which is dominated by the coordination bonds, from E = 141 ± 35 MPa in the non-oxidized material, to E = 87 ± 22 MPa, N = 3 after two-day exposure in water (blue) and E = 106 ± 28 MPa, N = 3 five-day exposure (orange). Assuming catechol oxidative cross-linking only increases the overall cross-link density, one would expect oxidation to further increase the elastic modulus. However, this is not what we observe. Other explanations are necessary, such as iron oxidation, which reduces the amount of iron available for complex formation, or the disruption of the complexes due to the oxidative coupling of catechol. The combination of these effects may cause a net reduction in elastic modulus with a small amount of oxidation caused by a short exposure to ambient conditions. However, the increase in modulus after five days of oxidation compared to two days may reflect that oxidative cross-linking has begun to dominate. The major effect of oxidative cross-linking is observed post-yield, when the coordination bonds start dissociating, with a markedly stiffer behavior dominated by a more cross-linked covalent network due to oxidative cross-linking. The higher density of covalent cross-links also leads to a lower maximum strain to fracture.

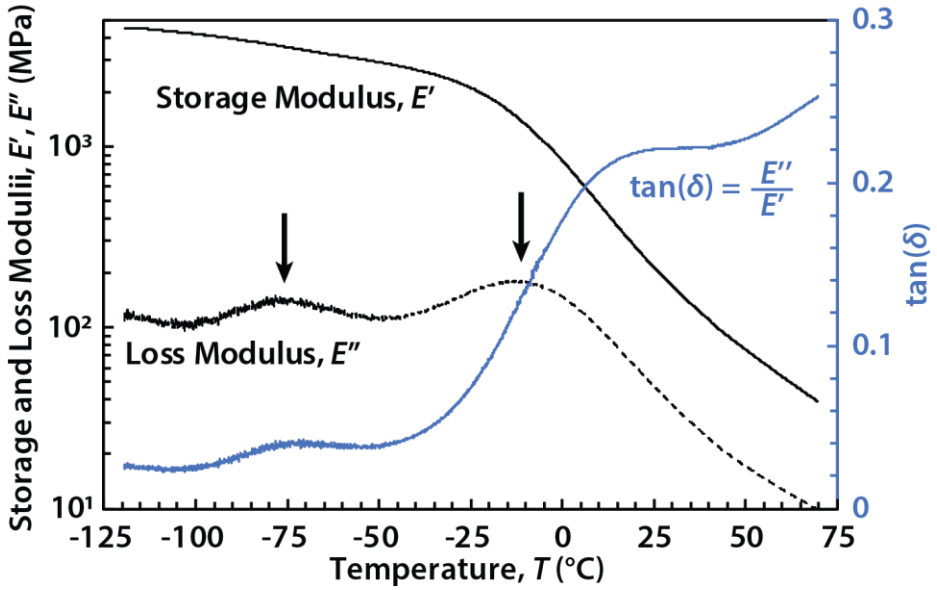

Figure 3.10 - Storage (E') and loss (E'') moduli, and tan(δ) of the iron-treated network measured by dynamic mechanical analysis (DMA). The storage modulus, E' (black line) exhibits a broad decay with increasing temperature, never reaching a rubbery state (where E' would be linearly increasing with temperature). The long transition also reflects the broad glass transition observed in DSC. The drop of E' coincides with the peak of E'' at −13 °C, which is in good agreement with the glass transition T_g measured by DSC, considering the difference in heating rate. The two peaks of E'' (indicated by black arrows) suggest a phase-separated system at very low temperatures, possibly correlated with the ionomer-like domains. At temperatures above 50 °C, which in DSC correspond to a region beyond the glass transition, tan(δ) (blue line) does not decrease. This suggests that the broad glass transition arises from a combination of multiple relaxations that are intrinsic to the designed system that contains both covalent bonds and iron-catechol dynamic coordinate bonds.

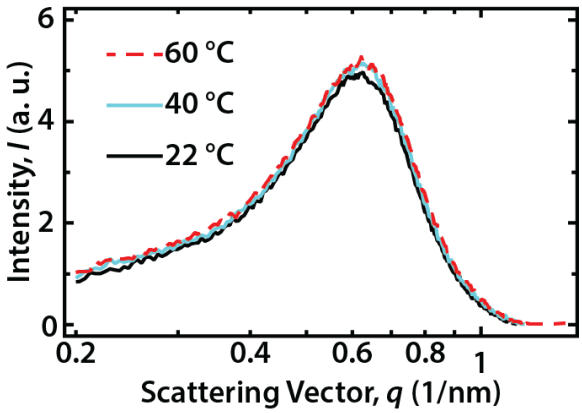

Figure 3.11 - Small-angle X-ray scattering (SAXS) of iron-treated 100% CAT network as a function of temperature. The so-called 'ionomer peak' does not change with temperature, indicating that the structure, spacing, and shape of the electron dense regions are static despite the energy input.

Upon cyclic loading of iron-treated networks (Figure 3.12A-C), energy dissipation is manifested as prominent hysteresis loops for strains beyond the linear regime. At small applied strains ($\varepsilon_n \leq 30\%$, Figure 3.12A) after a loading-unloading cycle, the covalent network and the unbroken coordination bonds preserve shape-memory and entropically drive the network back to the unstretched state. At larger applied strains ($\varepsilon_n \geq 50\%$), residual strain is observed even after resting intervals of t_{rest} = 90 min. This residual strain originates from the breaking of coordinate bonds during elongation and their reformation at newly accessible sites, resulting in stress-free network chains (illustrated in Figure 3.12E). These rearranged random-coil chains, upon release of tension, attempt to hold the network in the deformed shape for entropic reasons and oppose the restoring force of the covalent scaffold's elasticity. Stress relaxation curves (Figure 3.12D) corroborate the fast kinetics.

Other stiff, dry systems with reconfigurable architectures, such as self-healing supramolecular polymers where metal ions bridge polymer chains [9], neutralized thermoplastic ionomer resins [25], or thermoplastic polyurethanes [26], rely almost entirely on their respective microstructures. In contrast, the catechol-rich domains in the iron-treated network are not solely responsible for the enhanced mechanical properties. In the deprotected network, despite the presence of catechol-rich domains, the stiffness, strength, and toughness are low. It is the strength of the iron-catechol coordination bonds that amplifies the effect of the nanoscale domains beyond that which would be expected [27]. The tough mussel byssal cuticle may rely on the cooperation of similar mechanisms.

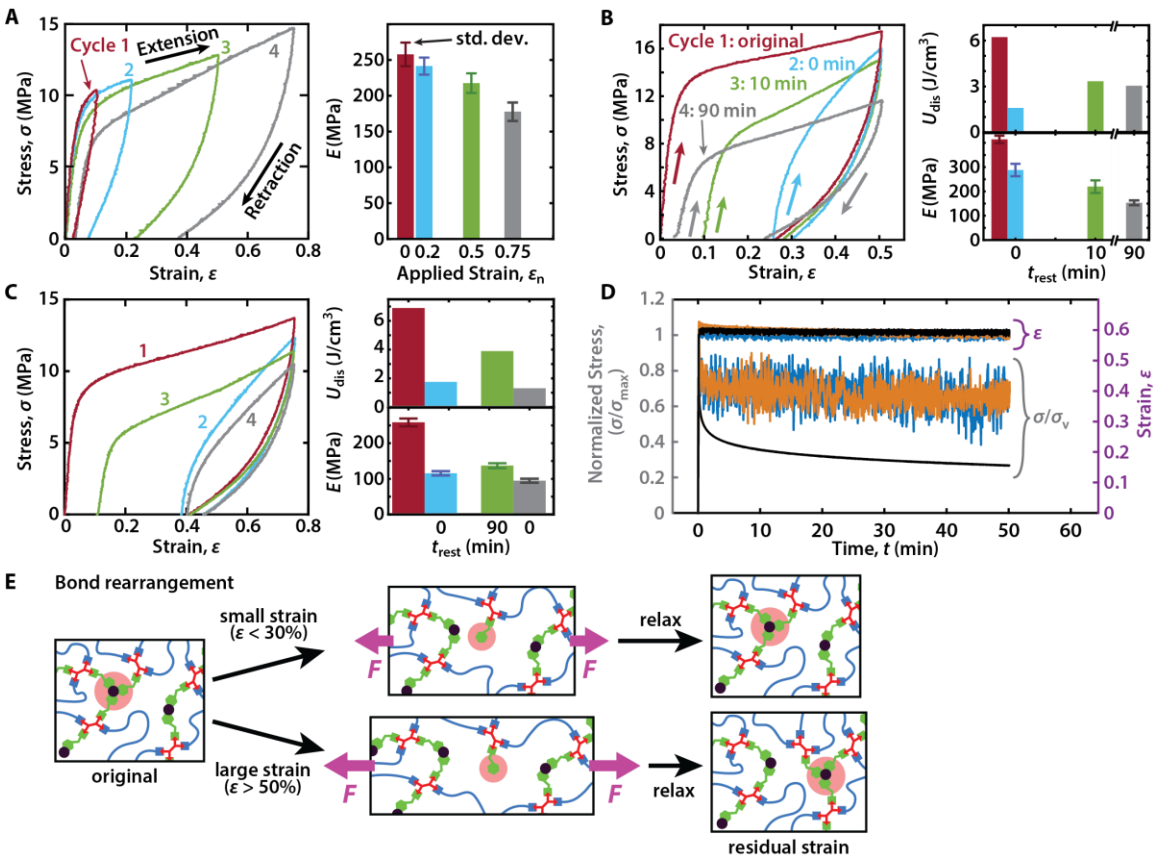

Figure 3.12 - Cyclic tensile tests and stress relaxation of iron-treated networks show hysteresis and mechanical recovery. (A) Sequential loading-unloading cycles with 30 min rest intervals, t_{rest} show successful recovery of elastic modulus and no residual strain for ε_n < 50%. (B, C) Strain-history dependence with varying rest intervals. Immediate reloading results in reduced toughness (histogram, top) and stiffness (bottom), but a 10-min rest interval results in 90% strain recovery. Longer resting (90 min) does not result in full strain recovery. Softening occurs possibly due to repeated loading or as a result of exposure to low, ambient relative humidity (19-20%) (see Figure 3.9A). Larger applied strain (C) results in reduced strain recovery (72%). (D) Stress relaxation for protected (blue), deprotected (orange), and iron-treated (black) specimens indicates the fast elastic and slow viscous responses. σ_{max} = 0.2, 0.3, and 19.3 MPa for protected, deprotected, and iron-treated samples, respectively. (E) Proposed mechanism for the strain recovery: at small strains, bonds reform at their original positions; at large strains, bonds migrate further, causing residual strain.

3.1.4 Conclusions

In summary, we have combined the bioinspired iron-catechol coordination bonds, which are sacrificial and reversible, with the covalent bonds of a cross-linked epoxy network, and created a single load-sharing network which is orders of magnitude stiffer, stronger, and tougher than its iron-free precursor. The toughening mechanism is due to the cooperation of dynamic iron-catechol chemistry in a dry environment and the incorporation of ionomeric nanodomains into a cross-linked network for mechanical enhancement.

3.1.5 Materials and Methods

3.1.5.1 Materials

The polymer poly(ethylene glycol) diglycidyl ether (PEG-diepoxide), cross-linker 1,4-diaminobutane, benzyl control group (2,3-epoxypropyl)benzene, hydrochloric acid, iron(III) nitrate nonahydrate, tetrahydrofuran, bicine, sodium hydroxide, trace metal grade sulfuric acid, and trace metal grade hydrogen peroxide were all purchased from Sigma Aldrich. The protected catechol species, 2- [[3,4-bis [(triethylsilyl)oxy]phenyl]methyl]-oxirane was kindly donated from Osaka Organic Chemical Industry.

3.1.5.2 Network synthesis and treatment

Polymer networks were synthesized by mixing the monomers per the compositions in Table 1 and degassing for 3 min at mtorr pressures. The monomer mixtures were then cured between hydrophobized glass slides at 60 °C and 450 torr for 12-15 hours. The 0.5 mm polymer films were then cut into D638 ASTM standard dog bone specimens using a steel punch. Specimens were then deprotected by submerging in 350 ml of degassed HCl at pH 2.5 for 24 hours. The solution was exchanged for fresh HCl every 2 hours for the first 6 hours of deprotection. After deprotection, the swollen specimens were immediately transferred to a 200-ml solution of 0.2 M bicine and 0.05 M $Fe(NO_3)_3 \cdot 9H_2O$, titrated to pH 7.5 with NaOH, and kept submerged for 24 hours. All samples – protected, deprotected, and iron-treated – were dried at 30 °C and 125 torr in a vacuum oven for 24 hours before any measurements were performed. All dry measurements were taken immediately after removing the samples from vacuum. Samples for tensile measurements under wet conditions were never dried. Instead, after iron incorporation, they were immersed in degassed deionized water for 24 hours. Samples for tensile measurements taking place before and after exposure to ambient conditions were dried in a vacuum oven at 30 °C and 200 torr for over 24 hours and then

either exposed for 1 hour to 21.5 °C and 41% relative humidity, or to 22 - 24 °C and 40 - 35% relative humidity for 7.5 hours. For comparison, samples were dried at a lower pressure at 100 torr, and then immediately pulled to fracture. To study the effects of induced oxidation, samples were placed into non-degassed deionized water immediately after iron incorporation, stored for either two or five days, then dried at 30 °C and 200 torr for 24 hours, and subsequently subjected to tensile testing.

3.1.5.3 Fourier-transform infrared (FTIR) spectroscopy

The network-curing epoxy-amine reaction was monitored in time with FTIR spectroscopy (Magna-IR 850, Series II by Nicolet). The separate reactants and the mixed solution were measured in between ZnSe windows and the entire assembly was placed at 60 °C. The IR spectra (7250-1000 cm^{-1}) were monitored at regular time intervals for the curing reactions of Networks 1, 2, and 4 (Table S1). The disappearance of the normalized, background-subtracted areas of the bands centered at 4940 cm^{-1} (primary amine) and 4520 cm^{-1} (epoxide) were monitored with time. The extent of reaction, X_t^i, of a given functional group, *i*, at total curing time, *t*, was calculated by dividing the difference between the area, A_t^i, of the corresponding IR band at $t = 0$ and the area at *t* by the area of the band at $t = 0$ [28, 29]:

$$X_t^i = \frac{A_{t=0}^i - A_t^i}{A_{t=0}^i} \tag{3.1}$$

3.1.5.4 Rheology

Rheometry was performed using a ARES-G2 by TA Instruments with a cone-and-plate geometry (2°, 40 mm diameter) at the curing temperature of 60 °C, 0.1% strain amplitude, and 10 rad/s angular frequency. The time evolution of the loss (G'') and storage

(G') moduli was measured for the protected catechol network starting from the mixture of the monomers.

3.1.5.5 Differential scanning calorimetry (DSC)

DSC was performed (TA Instruments Q2000) in the range of −100 °C to 50 °C with a heating and cooling rate of 5 °C/min. Final data were collected for two full cycles which were identical. The results of the second cycle are shown (Figure 3.7). Preliminary data were taken for three full cycles at 10 °C/min, which again were identical. The inflection points of the DSC traces were used for the determination of the glass transition temperatures, T_g.

3.1.5.6 X-ray photoelectron spectroscopy (XPS)

XPS was performed on a Kratos Axis Ultra DLD XPS system using a monochromated Al source (1486 eV). Survey scans were run at a pass energy of 160 eV, and high-resolution scans were run at 20 and 40 eV. A low-energy electron flood was used to neutralize charge, and the energy scale was calibrated by fitting the high-resolution aliphatic carbon 1s peak to 285.0 eV.

3.1.5.7 Resonance Raman spectroscopy

The interior surfaces of cross-sections were used to collect Raman spectra (Horiba, LabRAM Aramis spectrometer with confocal microscope) with a 785-nm laser line with the spectrometer pinhole and slit each set to 400 μm. Each spectrum is the average of 100 exposures of 500 ms each.

3.1.5.8 Inductively-coupled plasma atomic emission spectrometry (ICP-AES)

ICP-AES (Thermo iCAP 6300) was performed on samples previously digested in piranha (5:1 sulfuric acid:hydrogen peroxide, trace metal grade) and diluted to a parts per million concentration with Milli-Q water (resistivity of 18 MΩ).

3.1.5.9 Scanning electron microscopy (SEM) and energy dispersive X-ray spectroscopy (EDX)

For SEM, 20 μm thick cross-sections, sectioned with the Leica CM1850 cryostat at −28.3 °C, were sputter coated with gold/palladium 60/40, 99.99% (Hummer 6.2, Anatech, USA) for 90 seconds and imaged in backscattered mode with a scanning electron microscope (FEI XL30 Sirion FEG with EDX) using accelerating voltages of 5 kV. EDX was performed at 15 kV, more than double the K-edge absorption energy of iron.

3.1.5.10 Transmission electron microscopy (TEM, STEM-HAADF)

For TEM, 70 nm thin cross-sections were sliced with the Leica EM FC7 cryo-ultramicrotome using a diamond knife at −80 °C, significantly below the glass transition temperature of all samples. High resolution TEM (HRTEM, FEI Titan at 300 kV, λ = 1.96 pm) was performed to check for the presence of small precipitates with crystalline order. In addition, scanning TEM (STEM) was performed in a high angle annular dark-field STEM (HAADF-STEM) configuration to check for any clustering of iron atoms. The higher atomic number of iron, 26, compared to carbon, oxygen, and hydrogen (6, 8, and 1 respectively), ensures that any clustering of iron would lead to brighter regions in a STEM- HAADF image due to the greater incoherent scattering of electrons by heavy nuclei.

3.1.5.11 Small- and wide-angle X-ray scattering (SAXS and WAXS)

SAXS and WAXS measurements were conducted using a custom constructed SAXS instrument in the X-ray diffraction facility in the Materials Research Laboratory (MRL). The instrument uses a 50-μm microfocus, Cu target X-ray source (wavelength, λ = 1.54 Å) with parallel-beam multilayer optics and monochromator (Genix from XENOCS SA, France), high efficiency scatterless hybrid slits collimator developed in house [30], and Pilatus100k and Eiger 1M solid state detectors (Dectris, Switzerland). A built-in temperature stage that

houses the sample was used for the 40 °C and 60 °C SAXS measurements (Figure 3.11).

3.1.5.12 Uniaxial tensile testing

Uniaxial tensile testing was performed on 0.5 mm thick dog bone-shaped specimens (shown in Figure 3.1C-D) according to the ASTM D638 standard, on a custom-built setup on a vertical TwinRail positioning table (Lintech, CA) with a 10-lb load cell (3108-10, Eaton Corp., MI) fitted with a laser extensometer (LE-01, Electronic Instrument Research, PA). Cyclic-loading experiments were held at zero force between cycles by reducing the applied strain as specimens contracted.

3.1.5.13 Stress relaxation

Samples were first loaded uniaxially at a strain rate of $\dot{\varepsilon} = 10\ \text{min}^{-1}$ to a strain of $\varepsilon = 0.6$. Load and strain are measured with time at constant grip displacement.

3.1.5.14 Dynamic mechanical analysis (DMA)

DMA was performed at the Cornell Center for Materials Research. Experiments were conducted under tension in nitrogen atmosphere (Q800, TA Instruments) on iron-treated rectangular samples of dimension 7.5749 mm × 4.9100 mm × 0.5 mm. A tensile preload force of 0.01 N was applied and small oscillations of amplitude 0.05% strain applied at 1 Hz frequency. A temperature sweep from −120 °C to 70 °C was performed with a rate of 2 °C/min.

3.1.6 Additional Information

3.1.6.1 Rate-dependent uniaxial tensile stress strain curves

We calculate the slopes $S_{0.1}$, S_1, S_{10} corresponding to the segment $\sigma(\varepsilon > 1)$ for strain rates 0.1, 1, and 10 respectively. The slopes of these linear segments increase with strain rate from $S_{0.1} = 7.1 \pm 0.6$ MPa to $S_1 = 11.5 \pm 0.6$ MPa and $S_{10} = 14.2 \pm 0.4$ MPa. As this slope

occurs post-yielding, significant rearrangements have occurred compared to the original unstretched system. Increasing the tensile strain rate does not allow time for the coordination bonds to explore configurations and increases the resistance to dissociation, therefore increasing *S*. Furthermore, as the duration of the experimental run (the time to reach fracture) is very short, 0.4 min for the 10 min^{-1} strain rate versus 41 min for the 0.1 min^{-1} rate, there is not sufficient time to form stress-free coordination complexes. At slower strain rates, stress-free complexes can form, however the decreased slope shows that the increased number of reformed bonds cannot increase *S* sufficiently to compete with the softening due to ample time given for bonds and chains to explore new configurations and dissociate.

3.1.6.2 Predicting the *q*-shifts in SAXS ionomer peaks

The atomistic simulations of Bolintineanu et al. (*28*) predict for linear ionomers that changing the spacing between ionic side chains correspondingly changes the SAXS correlation distance between the 'ionomer peaks.' The ionomer peak measures the average distance, *r*, between ionomer clusters. This distance is related to the number of chain segments, *n*, between clusters by:

$$\langle r^2 \rangle = C_\infty n l^2 \tag{3.2}$$

where l is the length of a single chain segment and C_∞ is the characteristic ratio for the ionomer backbone. For the same backbone of sufficient length, C_∞ and l will be invariant, yielding the expression:

$$\frac{\langle r_1^2 \rangle}{n_1} = \frac{\langle r_2^2 \rangle}{n_2} \tag{3.3}$$

where subscripts denote polymers with different chain lengths between ionomer side groups. Thus, for two networks with Gaussian chains, the relationship between the ionomer peaks will be:

$$\langle r_2 \rangle = \langle r_1 \rangle \sqrt{\frac{n_2}{n_1}} \tag{3.4}$$

In the present work, the iron-treated 50% BENZ network has twice the average spacing between catechol groups as compared to the iron-treated 100% CAT network; therefore, $n_{50\%} = 2n_{100\%}$ and $r_{50\%} = r_{100\%}\sqrt{2}$. The measured values for $r_{50\%}$ and $r_{100\%}$ from SAXS (Figure 3.5D) are 12.2 ± 0.8 and 8.57 ± 0.02 nm, respectively, and $\frac{12.2 \pm 0.08 \text{ nm}}{8.57 \pm 0.02 \text{ nm}} = 1.42 \pm 0.09 \approx \sqrt{2}$.

3.1.6.3 Polymer network compositions

The monomer stoichiometries for Networks 1-3 were chosen to maximize the total composition of their respective monofunctional species while maintaining a fully-crosslinked network at very low cross-link density. The kinetic model presented by Cheng [19] describes exactly the type of epoxy-system we have synthesized (a bisepoxide/diamine system with a monoepoxide diluent). This model predicts a very slightly cross-linked, gelled network for a ratio, *s*, of [epoxy functional groups originating from monoepoxides] to [epoxy functional groups originating from bisepoxides], between 0.6 and 0.8. For the networks studied, $s = 0.77$ was chosen to maximize monoepoxide content while maintaining a true network and not creating a merely hyper-branched system.

3.1.6.4 DSC analysis

The benzyl-containing sample exhibits a typical glass transition curve with $T_g = -32.5 \pm 0.4$ °C. The protected catechol-containing sample with the bulky protecting groups exhibits reduced rotational freedom, in accordance with the crankshaft model, and a broadening of the glass transition with T_g −21.5 ± 0.5 °C. Even though the transition starts at the same temperature, it ends at a higher temperature depicting the additional energy needed

to overcome the lack of rotational freedom. However, the same ΔC_p is reached. The deprotected catechol sample shows a delay in the onset of the glass transition and a reduced ΔC_p, leading to an even higher T_g of -14.7 ± 0.5 °C. The deprotected catechols' ability to hydrogen bond fortuitously balances the lack of a bulky deprotecting group which would have driven T_g to a lower value. The net effect is a delay in the onset of the transition. The iron-treated sample exhibits a pronounced broadening with a T_g of -8.0 ± 0.6 °C. The presence of covalent and coordination bonds that act as cross-links, the polydispersity of the distances between them, and the multiple relaxation processes with varying timescales introduced due to the two types of bonding as well as the spatial segregation of catechols lead to the broadening of the transition. Dynamic mechanical analysis (DMA) data shown in Figure 3.10 provide a more detailed measurement of the broad glass transition measured by DSC.

3.2 Determining the effect of catechol concentration on the mechanical properties and nanostructure of iron-catechol epoxides

3.2.1 Abstract

In order to better understand the formation and structure of the nano-domains observed in the iron-catechol epoxy networks described in Section 3.1, a follow-up study was conducted to measure the mechanical properties and nanostructure of networks whose catechol concentrations were systematically varied by replacing a portion of the mono-functional catechol monomers with a non-chelating methyl glycidyl ether group. Though iron is successfully chelated by catechol in each network, the nano-domains do not form until some critical catechol concentration within the network. Both uniaxial tensile testing and SAXS experiments observe a qualitative shift in mechanical properties and nanostructure,

respectively, between these two catechol concentrations. The effect of residual, unchelated iron salts is also quantified but is determined to have a minimal effect compared to the effect of the complexation and nano-domain formation.

3.2.2 Results and discussion

3.2.2.1 Network design and formulation

The networks synthesized for this study use the same cross-linker (DAB) and backbone (PEG-DE) monomers as the networks synthesized in Section 3.1 (Figure 3.1). However, for each network composition, some mole percentage of the monofunctional catechol species (CAT) has been replaced by a non-chelating racemate of methyl glycidyl ether (MGE, Figure 3.13A, top panel). The mole ratios of PEG-DE:(CAT+MGE):DAB are equivalent to the ratio of PEG-DE:CAT:DAB in Section 3.1, and THF is added to each network until the entire system becomes miscible. The mole fractions of each monomer in the seven synthesized networks can be found in Figure 3.13A (table, bottom panel). The replacement of CAT by MGE leads to a network with fewer available iron-chelating ligands (Figure 3.13B, top panel), which leads to a network structure with a smaller amount of secondary iron-catechol cross-links after deprotection and iron-treatment[1] (Figure 3.13B, bottom panel). Though the network topology is preserved by keeping the overall mole fraction of monofunctional diluents constant across all CAT/MGE concentrations, the MGE monomer has a lower volume than the CAT monomer. This reduced volume proportionally increases the volumetric covalent cross-link density for networks with higher MGE (lower CAT) concentration. The effect of this change in covalent cross-link density on mechanical properties and nanostructure is discussed further in the following sections.

[1] In all cases, deprotection and iron-treatment is performed using the same solutions described in Section 3.1.5.2, without further washing. The networks in this study are dried at millitorr pressures and measured with minimal exposure to ambient conditions.

3.2.2.2 Uniaxial tensile testing reveals higher mechanical property enhancement with higher CAT concentration

Tensile testing samples for all seven network compositions were prepared and tested according to the procedure in Section 3.1.5.12. Figure 3.14A compares tensile properties of the protected, deprotected, and iron-treated networks for three catechol concentrations (10%, 30%, and 100% CAT). It is first important to note that the tensile properties of the iron-treated 100% CAT networks in this concentration study are about half the magnitude of the tensile properties of the 100% CAT network in Section 3.1 (Figure 3.8A). However, the orders-of-magnitude increases in toughness, ultimate strength, and elastic modulus without sacrificing ultimate strain are still observed. We attribute the differences between 100% CAT networks in the two studies to differences in the batches of PEG-DE, CAT, and DAB monomers used for network synthesis and therefore can only make qualitative comparisons with the networks in Sections 3.1. The other two CAT concentrations (10% and 30% CAT) shown in Figure 3.8A demonstrate further that the mechanical property change due to deprotection is minimal compared to the change due to iron-treatment (this observation is also true for the 2% and 50% CAT networks). Though it is suggested by the plots in Figure 3.8A that increased CAT concentration increases the mechanical property enhancement gained from iron-treatment, the true effect is subtle.

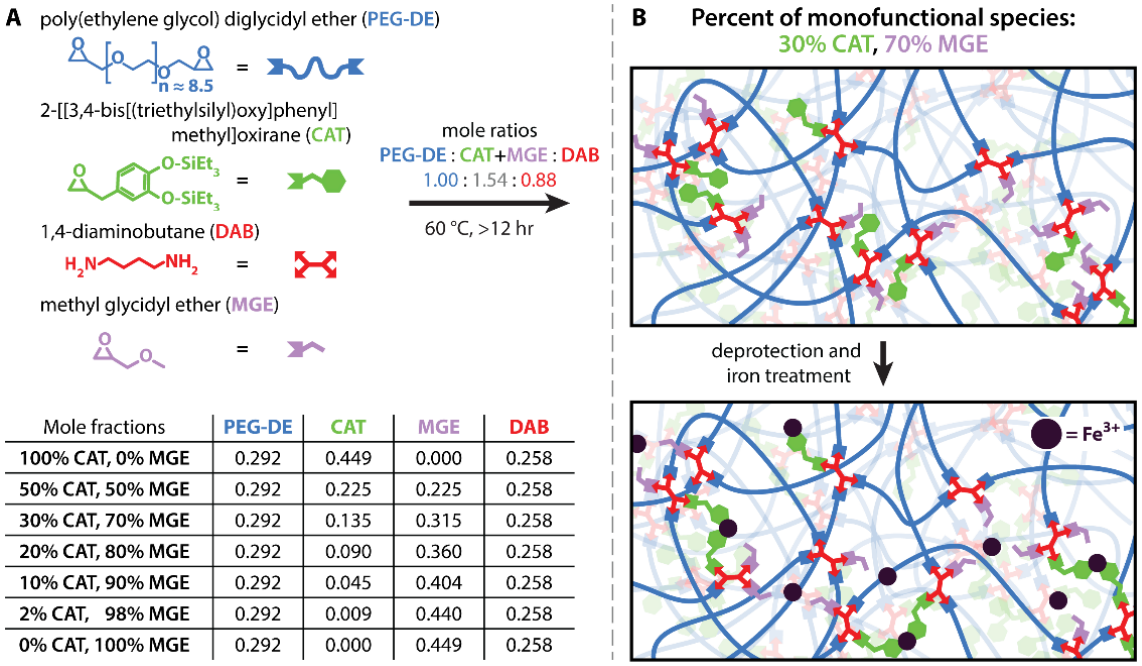

Mole fractions	PEG-DE	CAT	MGE	DAB
100% CAT, 0% MGE	0.292	0.449	0.000	0.258
50% CAT, 50% MGE	0.292	0.225	0.225	0.258
30% CAT, 70% MGE	0.292	0.135	0.315	0.258
20% CAT, 80% MGE	0.292	0.090	0.360	0.258
10% CAT, 90% MGE	0.292	0.045	0.404	0.258
2% CAT, 98% MGE	0.292	0.009	0.440	0.258
0% CAT, 100% MGE	0.292	0.000	0.449	0.258

Figure 3.13 – Network structure and compositions. A) The four monomers used to study the effect of catechol concentration. The overall mole ratio of monofunctional species, CAT+MGE, is preserved in all network formulations (table). B) representation of the protected and iron treated network for an example catechol concentration of 30% CAT, 70% MGE. The "deprotection and iron treatment" steps indicated by the vertical arrow are identical to those detailed in Figure 3.1. Also note that unbound iron is represented within the network which could potentially be left over from the iron-treatment steps.

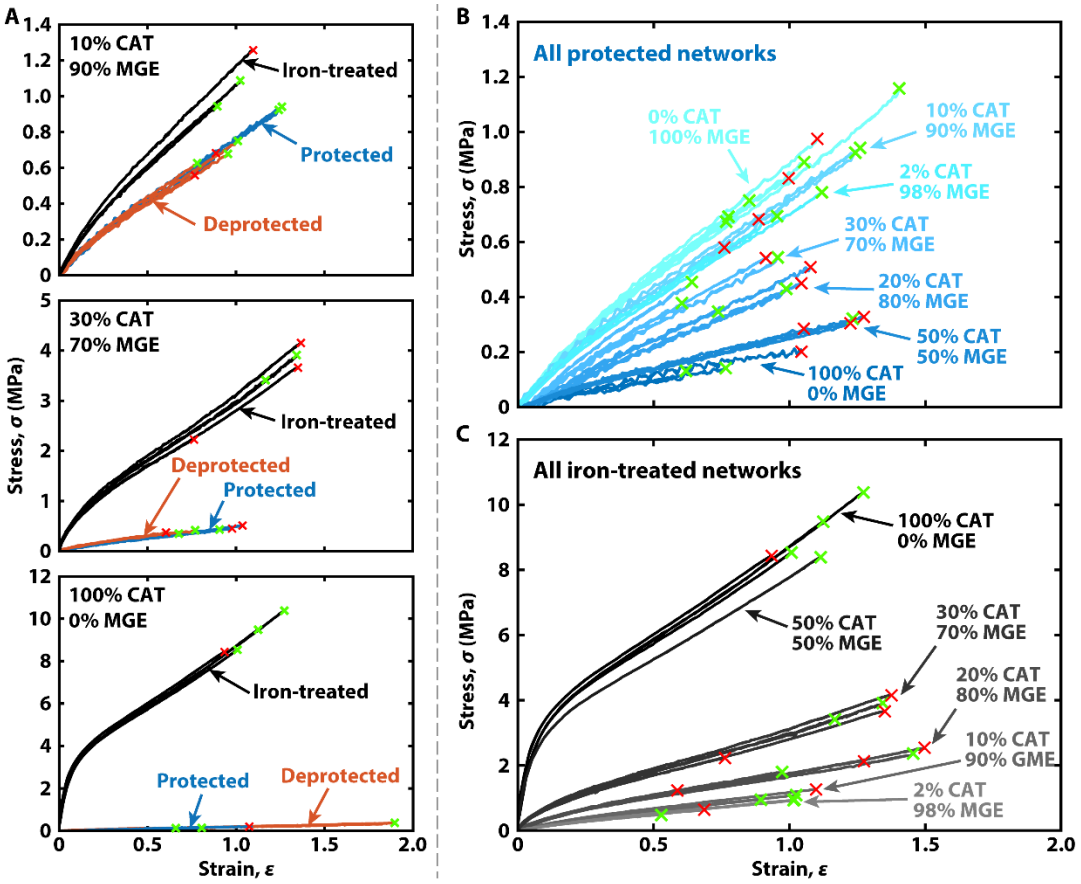

Figure 3.14 – Mechanical properties as a function of relative CAT/MGE concentration. (A) Stress vs. strain relationships comparing protected (blue), deprotected (orange), and iron-treated (black) networks for 10% CAT/90% MGE (top), 30% CAT/70% MGE (middle), and 100% CAT/0% MGE (bottom) monofunctional monomer compositions. For all three network compositions, the protected and deprotected networks have similar mechanical properties. Increasing % CAT increases the relative mechanical property enhancement (further visualized in Figure 3.15). The failure point for each test is represented by an "X", where green X's indicate failure within the specimen's gauge length and red X's indicate failure outside of the specimen's gauge length. Because sample preparation causes the failure strain to be defect driven, we conclude that there is no significant variation in failure strain among the full population of tests. (B) Protected network mechanical properties for all seven network compositions tested. Increasing % CAT decreases the stress measured at a given strain. (C) Iron-treated network mechanical properties for all seven network compositions tested. Increasing % CAT increases the stress measured at a given strain.

As noted above, the volume of MGE is lower than that of CAT. This manifests as an increase in covalent cross-link density with increasing MGE (decreasing CAT) concentration and can be observed by the increase in measured stresses for a given strain in the protected networks when transitioning from 100% CAT/0% MGE to 0% CAT/100% MGE (Figure 3.14B). After iron-treatment, the trend of increased mechanical properties with increased MGE concentration is reversed (Figure 3.14C). Even with a weaker covalent scaffold in the

higher CAT concentration networks, the formation of iron-catechol complexes dominates the stress response which increases with increasing CAT content. Further, the similarities between the tensile properties of 50% CAT and 100% CAT networks are surprising and indicate that there is likely a critical concentration above which the mode of stress transfer changes within the network. Using information related to the nanostructure of the networks gained from SAXS experiments (Figure 3.16), we conclude that this shift in mode of stress transfer is related to the formation of the iron-catechol nano-domains discussed in Section 3.1.

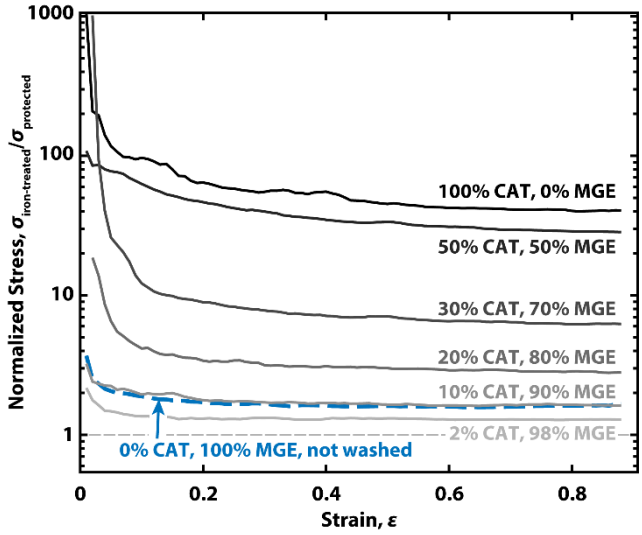

Figure 3.15 – Normalized stress vs. strain curves reveal relative property enhancement. Normalized curves are produced by dividing a representative iron-treated stress vs. strain curve for each CAT concentration by the corresponding representative stress vs. strain curve for the protected network of the same CAT concentration. The curves reveal a plateau in mechanical property enhancement at all CAT concentrations which increases with increasing CAT concentration. The dashed blue line representing the iron-treated but unwashed 0% CAT/100% MGE network gives a baseline for the effect of residual precipitates from the iron-treatment solution and is discussed further in Section 3.2.2.4 and Figure 3.17.

To better contextualize the relative increases in mechanical properties due to iron-treatment for each CAT concentration, the stress responses of the iron-treated networks, $\sigma_{iron\text{-}treated}$, have been normalized by the stress responses of the corresponding protected networks, $\sigma_{protected}$, by calculating $\sigma_{iron\text{-}treated}/\sigma_{protected}$ at each strain, ε (Figure 3.15). This phenomenological treatment of the data reveals that iron-treatment has a larger effect on the

initial mechanical properties of each network at low strains which then asymptotes to some constant, large-strain value. Also shown in Figure 3.15 is the effect of iron-treatment on the CAT-free network (blue dashed line) which is discussed further in Section 3.2.2.4.

3.2.2.3 Small-angle X-ray scattering correlates nano-structure to mechanical properties

For the high-CAT networks (50% CAT/50% MGE (purple) and 100% CAT/0% MGE (black)), the same trend of increasing scattering distance with decreasing CAT concentration is observed for the prominent Bragg peaks (blue shaded region) between $q = 0.3\ nm^{-1}$ and $2.0\ nm^{-1}$ (as compared to the 50% CAT/50% BENZ networks in Section 3.1, Figure 3.5D). Again, this trend arises from the increased spacing of iron aggregates with decreasing CAT concentration. The weaker scattering peaks in the low-CAT networks (0-30% CAT) in the same q-range are attributed instead to iron localizing near net points but not yet forming true multi-net-point aggregates. This is further supported by these weaker peaks shifting towards lower q (higher average separation, d) and higher intensity as the CAT concentration is increased. The decrease in q can be explained by the decrease in cross-link density (and therefore increase in cross-link spacing). The increase in intensity can be explained by the larger amount of cross-link points which contain CAT, and therefore iron-catechol complexes, whose large scattering cross-section increases the scattering intensity. Taken together, the peaks in the 50% and 100% CAT networks and the peaks in the 0% to 30% CAT networks corroborate the notion that there is a critical concentration of CAT, between 30% and 50%, which allows for the formation of iron-catechol nano-domains.

Also apparent in the SAXS curves is the increased scattering intensity at low q for the 10% to 30% CAT networks. We presume this effect is due to the precipitation of residual solutes, as discussed above and elaborated upon in the next section.

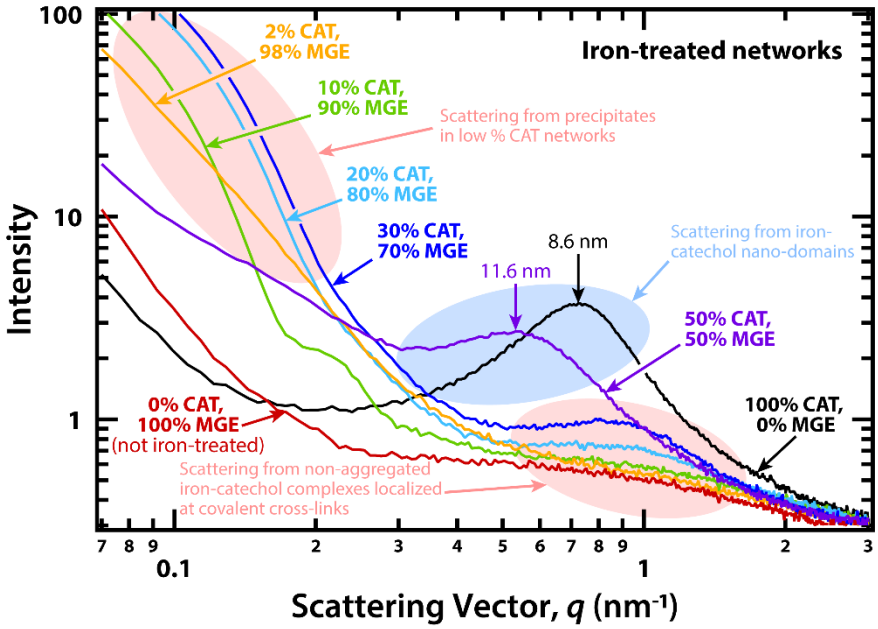

Figure 3.16 – Effect of CAT concentration on network nanostructure. SAXS experiments on iron-treated networks of each CAT concentration reveal characteristic features of both low-CAT (10-30% CAT, red shaded regions) and high-CAT (50-100% CAT, blue shaded regions) networks. The untreated 0% CAT network is also plotted and shows a very weak, broad peak around $q = 1$ nm^{-1}. The prominent Bragg peaks for the high-CAT networks are labeled with their corresponding *d*-spacing. The weaker Bragg peaks for the low-CAT networks correspond to average *d*-spacings of about 6 to 7 nm. Possible physical interpretations for each characteristic feature are indicated. The iron-treated, unwashed 0% CAT network (not shown) was also measured and shows similar low-*q* scattering attributed to residual solutes, but its intensity cannot be scaled relative to the other SAXS curves.

3.2.2.4 Accounting for the effect of residual solutes

The previous sections have alluded to one important caveat to the results presented in this Section 3.2: It is possible that some amount of residual solutes precipitate out of the iron-treated networks upon drying, especially at lower CAT concentrations, due to a lack of washing after treatment. This phenomenon is directly observable in the 0% CAT/100% MGE network and is detailed in Figure 3.17.

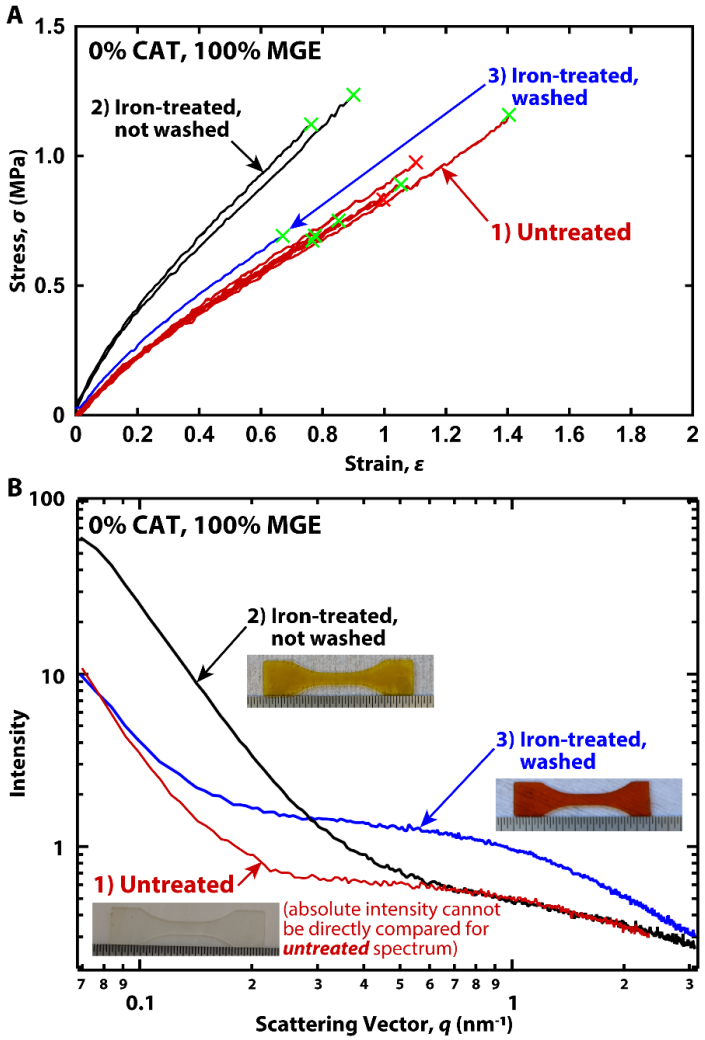

Figure 3.17 – Determining the effect of precipitates on the 0% CAT/100% MGE network. Uniaxial tensile tests (A) and SAXS measurements (B) on the 0% CAT/100% MGE network as cured ('untreated', red), after exposure to the iron-treatment solution and then dried ('iron-treated, not washed', black), and after being washed with 18 MΩ Milli-Q water for 48 hrs post-iron-treatment ('iron-treated, washed', blue). Both the tensile and SAXS data show partial reversibility. Pictures of representative tensile testing specimen are also shown in (B).

After swelling the 0% CAT network in the same iron solution used to treat the other networks the re-dried 0% CAT network becomes a yellow-orange color and is no longer fully transparent (Figure 3.17B). We attribute this change in coloration to the precipitation of residual solutes from the iron-treatment solution. These solutes may also be present in other low-CAT networks, but they are not directly observable due to the opaque, near-black shade of purple that even the 2% CAT network exhibits due to the high extinction coefficient of the iron-catechol complexes. This change of color in the 0% CAT network is accompanied by a

slight increase in mechanical properties (Figure 3.15, Figure 3.17A, ‘not washed’). We believe this indicates that some of the mechanical property enhancement seen in the low-CAT networks could be due to these precipitates.

Exposing ‘not washed’ networks to 18 MΩ Milli-Q water for 48 hours nearly completely removes the precipitates: the network is again transparent but has a small amount of red-orange coloration (Figure 3.17B), perhaps due to a low concentration of iron-PEG or iron-hydroxyl chelation. The iron-treated washed 0% CAT network also exhibits a stress response nearly identical to that of the untreated 0% CAT network. A similar reversibility is measured in SAXS (Figure 3.17B), where the ‘not washed’ network has much higher-intensity scattering at low q compared to the untreated 0% CAT network. Similar low-q scattering is observed for the unwashed 10%, 20%, and 30% CAT networks (Figure 3.16). However, the low-q scattering is reduced after the washing step for the 0% CAT concentration. This leads us to conclude that the low-q scattering is due to precipitation of residual solutes.

A seemingly trivial solution to avoid this precipitation would be to wash all networks after iron treatment. However, we believe that the susceptibility of the catechol to oxidation and the complexation dependence on pH would together cause more uncertainties in interpreting the data than simply not washing the networks. We have also demonstrated that the effect of residual solutes, though measurable, is small compared to the effects of the iron complexation. If anything, successfully removing the residual solutes would further separate the mechanical properties of the high-CAT and low-CAT networks, strengthening the conclusion that a critical CAT concentration within these networks allows for the formation of iron-catechol clusters.

3.2.3 Conclusions

To further understand the mechanism by which iron-catechol complexes, and the nano-domains which they form, enhance the mechanical properties of epoxy networks (especially their toughness and stiffness), we studied a series of CAT-containing networks whose CAT concentration was systematically varied. We discovered that there exists a critical catechol concentration beyond which iron-rich nano-domains can form and further enhance the mechanical properties of the network. Unlike traditional linear ionomer networks, the covalent scaffold of this network locks iron-catechol clusters in place and prevents aggregation at low CAT concentrations. We believe this phenomenon is generalizable to other metal-ligand systems.

If this strategy of binding metal-chelating ligands to a covalent network to improve toughness without sacrificing extensibility is to be widely adopted, 'critical ligand concentrations' must be considered when devising appropriate network formulations.

3.3 References

1. Domun, N., Hadavinia, H., Zhang, T., Sainsbury, T., Liaghat, G.H., Vahid, S., Improving the fracture toughness and the strength of epoxy using nanomaterials – a review of the current status. *Nanoscale*. 7, 10294–10329 (2015)

2. Ducrot, E., Chen, Y., Butlers, M., Sijbesma, R.P., Creton, C., Toughening elastomers with sacrificial bonds and watching them break. *Science*. 186, 186–190 (2014)

3. Ducrot, E., Creton, C., Characterizing large strain elasticity of brittle elastomeric networks by embedding them in a soft extensible matrix. *Adv. Funct. Mater.* 26, 2482–2492 (2016)

4. Ohmori, K., Abu Bin, I., Seki, T., Liu, C., Mayumi, K., Ito, K., Takeoka, Y., Molecular weight dependency of polyrotaxane-cross-linked polymer gel extensibility. *Chem. Commun.* 52, 13757–13759 (2016)

5. Holten-Andersen, N., Harrington, M.J., Birkedal, H., Lee, B.P., Messersmith, P.B., Lee, K.Y.C., Waite, J.H., pH-induced metal-ligand cross-links inspired by mussel yield self-healing polymer networks with near-covalent elastic moduli. *Proc. Natl.*

Acad. Sci. U. S. A. 108, 2651–2655 (2011)

6. Mozhdehi, D., Ayala, S., Cromwell, O.R., Guan, Z., Self-healing multiphase polymers via dynamic metal–ligand interactions. *J. Am. Chem. Soc.* 136, 16128–16131 (2014)

7. Lane, D.D., Kaur, S., Weerasakare, G.M., Stewart, R.J., Toughened hydrogels inspired by aquatic caddisworm silk. *Soft Matter*. 11, 6981–6990 (2015)

8. Neal, J.A., Mozhdehi, D., Guan, Z., Enhancing mechanical performance of a covalent self-healing material by sacrificial noncovalent bonds. *J. Am. Chem. Soc.* 137, 4846–4850 (2015)

9. Burnworth, M., Tang, L., Kumpfer, J.R., Duncan, A.J., Beyer, F.L., Fiore, G.L., Rowan, S.J., Weder, C., Optically healable supramolecular polymers. *Nature*. 472, 334–337 (2011)

10. Sun, T.L., Kurokawa, T., Kuroda, S., Ihsan, A. Bin, Akasaki, T., Sato, K., Nakajima, T., Gong, J.P., Haque, M.A., Nakajima, T., Gong, J.P., Haque, M.A., Physical hydrogels composed of polyampholytes demonstrate high toughness and viscoelasticity. *Nat. Mater.* 12, 932–937 (2013)

11. Sun, J.-Y., Zhao, X., Illeperuma, W.R.K., Chaudhuri, O., Oh, K.H., Mooney, D.J., Vlassak, J.J., Suo, Z., Highly stretchable and tough hydrogels. *Nature*. 489, 133–136 (2012)

12. Carrington, E., Gosline, J.M., Mechanical design of mussel byssus: Load cycle and strain rate dependence. *Am. Malacol. Bull.* 18, 135–142 (2004)

13. Harrington, M.J., Masic, A., Holten-Andersen, N., Waite, J.H., Fratzl, P., Iron-clad fibers: A metal-based biological strategy for hard flexible coatings. *Science*. 328, 216–220 (2010)

14. Barrett, D.G., Fullenkamp, D.E., He, L., Holten-Andersen, N., Lee, K.Y.C., Messersmith, P.B., pH-based regulation of hydrogel mechanical properties through mussel-inspired chemistry and processing. *Adv. Funct. Mater.* 23, 1111–1119 (2013)

15. Grindy, S.C., Learsch, R., Mozhdehi, D., Cheng, J., Barrett, D.G., Guan, Z., Messersmith, P.B., Holten-Andersen, N., Control of hierarchical polymer mechanics with bioinspired metal-coordination dynamics. *Nat. Mater.* 14, 1210–1216 (2015)

16. Lee, H., Scherer, N.F., Messersmith, P.B., Single-molecule mechanics of mussel adhesion. *Proc. Natl. Acad. Sci. U. S. A.* 103, 12999–13003 (2006)

17. Xu, Z., Mechanics of metal-catecholate complexes: The roles of coordination state and metal types. *Sci. Rep.* 3, 2914 (2013)

18. Menyo, M.S., Hawker, C.J., Waite, J.H., Versatile tuning of supramolecular hydrogels through metal complexation of oxidation-resistant catechol-inspired ligands. *Soft*

Matter. 9, 10314–10323 (2013)

19. Cheng, K.-C., Kinetic model of diepoxides with reactive diluents cured with amines. *J. Polym. Sci. Part B Polym. Phys.* 36, 2339–2348 (1998)

20. Fullenkamp, D.E., Barrett, D.G., Miller, D.R., Kurutz, J.W., Messersmith, P.B., pH-dependent cross-linking of catechols through oxidation via Fe 3+ and potential implications for mussel adhesion. *RSC Adv.* 4, 25127–25134 (2014)

21. Taylor, S.W., Chase, D.B., Emptage, M.H., Nelson, M.J., Waite, J.H., Ferric ion complexes of a DOPA-containing adhesive protein from Mytilus edulis. *Inorg. Chem.* 35, 7572–7577 (1996)

22. Grady, B.P., Review and critical analysis of the morphology of random ionomers across many length scales. *Polym. Eng. Sci.* 48, 1029–1051 (2008)

23. Buitrago, C.F., Bolintineanu, D.S., Seitz, M.E., Opper, K.L., Wagener, K.B., Stevens, M.J., Frischknecht, A.L., Winey, K.I., Direct comparisons of x-ray scattering and atomistic molecular dynamics simulations for precise acid copolymers and Ionomers. *Macromolecules*. 48, 1210–1220 (2015)

24. Lesser, A.J., Kody, R.S., A generalized model for the yield behavior of epoxy networks in multiaxial stress states. *J. Polym. Sci. Part B Polym. Phys.* 35, 1611–1619 (1997)

25. Hirasawa, E., Yamamoto, Y., Tadano, K., Yano, S., Effect of metal cation type on the structure and properties of ethylene ionomers. *J. Appl. Polym. Sci.* 42, 351–362 (1991)

26. Qi, H.J., Boyce, M.C., Stress-strain behavior of thermoplastic polyurethanes. *Mech. Mater.* 37, 817–839 (2005)

27. Bellinger, M.A., Sauer, J.A., Hara, M., Tensile fracture properties of rigid-rigid blends made of sulfonated polystyrene ionomer and polystyrene. *Macromolecules*. 27, 6147–6155 (1994)

28. Moraes, L.G.P., Rocha, R.S.F., Menegazzo, L.M., Araújo, E.B. de, Yukimito, K., Moraes, J.C.S., Infrared spectroscopy: a tool for determination of the degree of conversion in dental composites. *J. Appl. Oral Sci.* 16, 145–149 (2008)

29. González-González, M., Carlos, J., Baselg, J., Applications of FTIR on epoxy resins - Identification, monitoring the curing process, phase separation and water uptake. In: Theophile, T. (ed.) Infrared Spectroscopy - Materials Science, Engineering and Technology. pp. 261–284. InTech (2012)

30. Li, Y., Beck, R., Huang, T., Choi, M.C., Divinagracia, M., Scatterless hybrid metal-single-crystal slit for small-angle X-ray scattering and high-resolution X-ray diffraction. *J. Appl. Crystallogr.* 41, 1134–1139 (2008)

PART 2: Characterizing consumer skincare and hair care products

4 Characterizing dynamic, high-frequency friction in lubricating complex-fluid thin films between viscoelastic surfaces

Adapted from: **Cristiani, T.R.**, Cadirov, N.A., Ehrman, M., Kristiansen, K., Scott, J., Jamadagni, S., Israelachvili, J.N., ***Tribol. Lett.*** 66, 149 **(2018)**

4.1 Abstract

To investigate the friction dynamics (time evolution of the friction response, including stiction and stick-slip sliding) between viscoelastic surfaces lubricated with complex fluid films, a 'wavelet decomposition' time-series analysis method was applied to measured friction traces. Data was acquired using an updated 'Rotating Disk' attachment for the Surface Forces Apparatus (RD-SFA). We have studied the friction frequency response of PDMS surfaces (sphere-on-flat geometry, 2 cm radius) interacting across various 'everyday' fluids (oils, creams, moisturizers, etc.) from 0 to 2,500 Hz under high sliding velocities/shear rates. The RD attachment is capable of shearing two surfaces at velocities from mm/s to m/s in controlled temperature, humidity, and vapor composition environments. The friction experiments were performed at varying loads (20 to 320 mN) and velocities (1 to 40 mm/s) with a 20-microsecond sampling time. At such (and especially higher) velocities, 'wavelet decomposition' can be used to explore the time evolution of friction dynamics and is the most appropriate method for such tasks given its unique ability to resolve broad-spectrum transient frequency components with good time- and frequency-localization. This technique is general and enables the unambiguous characterization of any system fluctuations or resonant vibrations associated with stick-slip sliding and other 'intermittent friction'. These results illustrate the complex and varied friction dynamics that can arise under different

experimental or environmental conditions and have implications for damage, wear, and sensory perception.

4.2 Introduction

Everyday fluids are heterogeneous and complex, and, when used as lubricants, will give rise to time-dependent, intermittent, and non-Amontonian friction behavior. Such fluids range from skin care products (creams, moisturizers, etc.), soaps, and detergents, to device lubricants (motor oil, coolants, etc.), which contain several constituents at the molecular and colloidal scale. Insights into the frictional behavior of everyday fluids are important to extract essential information about sensory perception, feel, and wear and friction control [1–4]. However, the complexity in the friction forces, such as fluctuations, has made a standardized analysis scheme difficult to propose, and simpler coarse models are still in use.

Although fluctuations in friction forces with time are commonly observed, the average friction force alone is generally used to describe friction behavior. The most common way to quantify friction is through a friction coefficient, $\mu = F/L$, or simply the friction force (the resistive parallel force between sliding surfaces, F) divided by the load (the perpendicular or normal force, L). This metric can give insight into energy loss due to frictional processes but tends not to be constant with varying sliding conditions, including loads and velocities, especially in the presence of adhesion forces and for lubricated (viscous, rheological) systems [5–7].

Common systems used to study friction and lubrication in engineering and manufacturing settings include four ball [8], twin disk [9], ball-on-disk, and pin-on-disk tribometers [9]. These systems can achieve a large range of speeds (mm/s to m/s) and loads

(mN to 10s of N), but how friction varies with time (friction dynamics) is rarely considered during analysis [10, 11]. Atomic Force Microscopy (AFM) is used to measure friction on the molecular level, but has difficulties decoupling parallel (F) and normal (L) forces [12]. Also, friction experiments with a highly pointed AFM tip do not easily or directly translate to the more applicable scenario of two extended (macroscopic) surfaces shearing. Most friction studies are performed to create a Stribeck curve [13, 14], which evaluates the friction coefficient, μ, over a wide range of sliding velocities. However, many of these studies only analyze friction behavior at a single, constant load. Also, these relationships only consider the average friction force – ignoring the subtle but important low and high frequency components that can vary from 10^{-3} – 10^{4} Hz.

Since friction behavior can be quite complex (due to system parameters such as: (1) surface chemical and physical features, (2) fluid and molecular heterogeneities, and (3) temperature fluctuations), there is no simple relationship that predicts how kinetic friction will vary with time, leaving these variations often over-simplified or ignored. Historically, the fluctuations in friction were assumed to be noise (random fluctuations) in the measurement. Yet frictional systems exhibit everything from smooth sliding, to resonant vibrations (sinusoidal), intermittent fluctuations (chaotic), and stick-slip friction (periodic, non-sinusoidal) [15]. Friction dynamics have been shown to be prevalent in many phenomena including sensory perception [16–18] (mouth feel, sound, touch), as well as the explanation for shudder [19] or noise in car engines, and as a damage predictor in systems such as hard drives [20] and articular cartilage [21]. These effects can be much better understood by studying friction dynamics as opposed to the average values in a friction experiment or measurement.

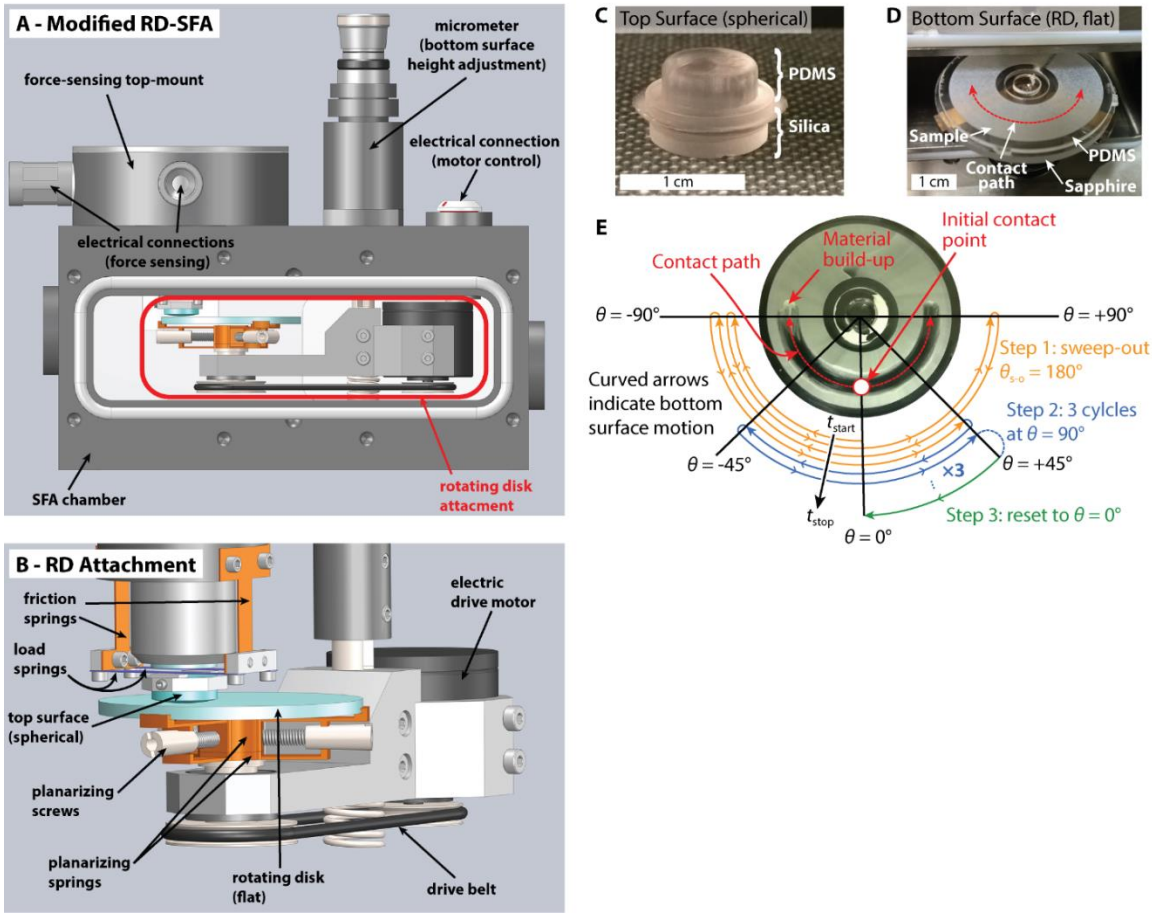

Figure 4.1- The Rotating Disk Surface Forces Apparatus (RD-SFA) and surfaces used. A. Schematic of the RD-SFA. The rotating disk attachment fits into the chamber of an SFA2000 (Surforce LLC). The height of the bottom (flat) rotating surface can be adjusted with a micrometer to load and separate the surfaces. B. Detailed view of the RD attachment. A rotating stage, driven by an electric servo-motor and pully system, holds the bottom surface (a 40-mm diameter sapphire disk). The stage can be planarized by splaying three pairs of cantilever springs with adjustable conical screws. The upper (spherical) surface is mounted on a stage with both friction (orange) and load (blue) sensing springs, each equipped with metal foil strain gauges. C. The top surface used in these experiments is a spherical PDMS cap attached to a typical silica disk used in SFA experiments. D. The bottom surface is a flat PDMS (with a 50-micron trough to hold the sample fluid) on a 40 mm diameter silica sapphire disk. E. Sweeping path used in the experimental procedure: an initial 180° (~48 mm) "sweep-out" is performed followed by three cycles at 90° (~24 mm) in which the analyzed forces were obtained.

To more fully characterize friction behavior and perform high-speed, high-sensitivity friction measurements (to determine dynamic or transient effects), we have developed an updated rotating disk attachment for the surface forces apparatus (RD-SFA), shown in Figure 4.1 and described below. The rotating disk attachment utilizes interchangeable motors that can achieve linear speeds of mm/s to m/s. The device has a high torque threshold and high

normal and friction force resolution. The motion of the disk can be arbitrarily controlled, including continuous sliding and oscillatory motion. In addition, though not explored explicitly in this work, the surfaces can be prepared to include reflecting layers for sub-nanometer distance measurements using multiple-beam interferometry. We analyze the high-speed friction data using 'wavelet transforms' [22–24] to determine the variation of frequency components with time, as well as their relative magnitudes. This method allows for unambiguous differentiation between oscillatory responses from natural, e.g., mechanical resonance, frequencies in the whole system and stick-slip friction that arises from surface interactions. Such techniques have been used in tribological systems to generate predictive models for evaluating joint and bearing failure but are applied to acoustic emission signals and not directly to friction traces [25]. We have performed friction experiments on several complex fluid mixtures, and characterized them with these methods, quantifying their differing complex dynamic responses at various velocities and loads.

4.3 Materials and methods

4.3.1 Experimental apparatus

The updated rotating disk attachment for the SFA2000 (SurForce LLC, RD-SFA, Figure 4.1) builds upon an earlier design [26]. Previously, the rotating disk bottom surface was directly attached to the motor, requiring the use of small motors, making it difficult to achieve a large range of velocities and loads. This choice of motor placement also limited the amount of torque the drive motor could supply and increased the mass of the rotating elements, therefore decreasing the resonant frequency of the system, which ultimately limits the maximum frequencies that can be measured. The motor in the new design is coupled to

the bottom surface using a pulley/belt system, the diameters of which can be tuned to achieve a range of desired speeds. The new motor is also driven by a digital motion controller which can independently specify velocity, acceleration, and displacement, as opposed to the limited-ranged and unidirectional velocity control available with the low-torque motors in the previous design. The bottom disk is more modular in the redesigned system as well, allowing the bottom surface to be easily interchanged between experiments. The method to ensure planarity of the bottom surface has also been simplified and improved using three arms, each of which contains two opposing cantilever springs which, with the aid of a conical screw, push on each other and tilt the bottom surface in any direction (Figure 4.1B).

By utilizing this new design, the top disk mount was also altered to contain both the (vertical, normal) load- and the (lateral) friction-sensing springs because the lower rotating-disk mount no longer senses the load (Figure 4.1B) as in conventional SFAs. The foil-gauged friction and load springs have a force resolution of 0.1 mN and a range of 30 N. Greater sensitivity can be achieved with semiconductor strain gauges and different spring stiffness.

4.3.2 Surface Preparation

Cross-linked, molded PDMS films were adhered to silica disks in these experiments to mimic ‘soft’ (viscoelastic) biomaterial interfaces. A 1:10 ratio of cross-linker to PDMS was used (Sylgard 184 Dow Corning), and the surfaces were cured overnight in an oven at 85 ^{o}C. The top surface is a spherical cap with a 1 cm radius of curvature that was adhered to a 1 cm diameter flat silica disk Figure 4.1C). The bottom (rotating) PDMS surface, which is cured onto a 40-mm sapphire disk, is 1 mm thick and 40 mm in diameter and has a 50-μm deep annular trough used to cast a thin film of each sample Figure 4.1D).

4.3.3 Sample characteristics

Model personal care skin creams and facial moisturizers were studied to determine their friction (or lubrication) behavior. Three non-Newtonian shear thinning fluids (based on rheological behavior, Figure 4.2) were chosen for this study. Each fluid is a modification of a similar polyacrylate starch microgel. Sample 1 is an oil in water emulsion dispersed in the aqueous microgel. The formulation contains typical skin-care additives, fatty alcohols (combination of stearyl alcohol, cetyl alcohol, and behenyl alcohol), and feel-modifying powders. Sample 2 does not include any secondary or tertiary 'structurants' and is only comprised of the polyacrylate starch microgel. The formula includes aqueous skin-care additives but includes no additional oils, no fatty alcohols, and no additional powders. Lastly, Sample 3 is a silicone emulsion dispersed in the microgel with additional crystallized hydrocarbon waxes. The synthetic waxes are unbranched hydrocarbons with molecular weights ranging from 300 to 1000 Da. The melting points of the waxes are between 61-67 °C. The silicone phase of the emulsion also contains dimethicone crosspolymers which are typically added to skin-care fluids for their tactile and sensory benefits. Table 3.1 displays some qualitative properties among the fluids.

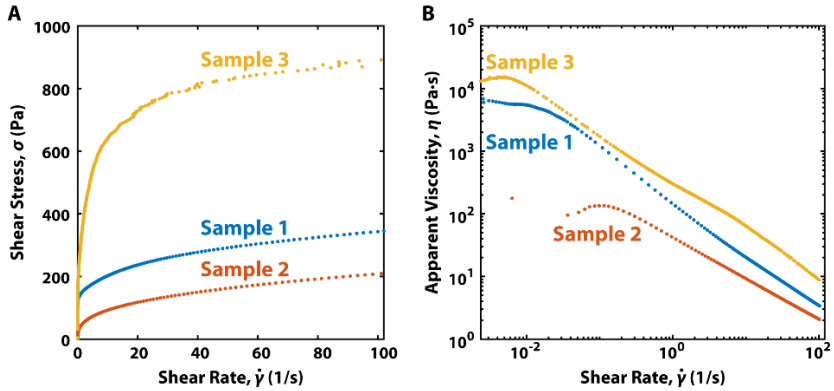

Figure 4.2 - Rheological data of each sample tested via a stress-controlled flow ramp. A. Shear stress, σ, (in Pa) plotted as a function of shear rate, $\dot{\boldsymbol{\gamma}}$, (in 1/s) for each sample. B. Apparent viscosity, η, (in Pa·s) plotted as a function of $\dot{\boldsymbol{\gamma}}$. Both panels A and B suggest that each sample is shear thinning, with the 'upper Newtonian plateau' of Sample 2 extending to higher shear rates than both Samples 1 and 3.

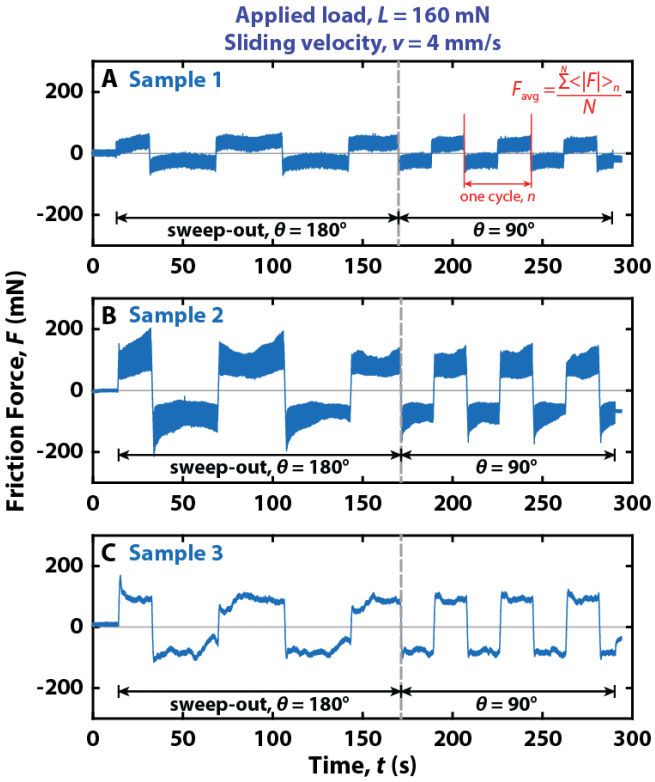

Figure 4.3 - Representative friction traces for all three samples at L = 160 mN and v = 4 mm/s. Large angle sweeps (180°, 2 full oscillations) of deposited films were conducted to normalize the sample thicknesses and previous histories and are indicated to the left of the vertical gray dashed lines. The analyzed portions of the friction traces occur to the right of the vertical gray dashed lines (smaller oscillations of 90°) and when averaged over multiple runs give rise to the points in Figure 4.6 (see Results and Discussion). The corresponding sweeping path is illustrated in depth in Figure 4.1E.

4.3.4 Friction measurements

The rotating disk was used to perform oscillating shear experiments with a peak-to-peak angle, θ = 90° (~24 mm). Prior to each measurement, the as-cast films of each sample were conditioned by performing three 'sweep-out' oscillations with a sweep-out angle of $\theta_{s\text{-}o}$ = 180° (~48 mm) to remove excess material from the contact area and prevent build-up. The overall motion path is illustrated in Figure 4.1E. The sweep-out regime is labeled in each sample's friction trace in Figure 4.3. For each film, the applied load started at 20 mN and stepwise increased to 320 mN (corresponding to pressures of 2 to 60 kPa), and the velocity was stepwise increased from 1 to 40 mm/s at each applied load. These ranges of loads and velocities are relevant for applications such as determining sensory perception or 'feel' on

human skin. The top panel of Figure 4.3 also illustrates how the 'average kinetic friction', F_{avg}, plotted in Figure 4.6 was calculated. Data was collected at 20 µs intervals to ensure that high maximum frequencies were measurable (as high as 12.5 kHz); however, no resonance or stick-slip features were observed above ~1 kHz. Therefore, the number of data points were decreased by a factor of ten to reduce wavelet transform computational time.

4.3.5 Wavelet analysis

To expand friction analysis beyond typical friction coefficient measurements, a continuous Morse wavelet transform [27, 28] was applied to each friction trace to unambiguously extract the time-dependent frequency components of the friction traces, allowing for detailed interpretation of dynamic, intermittent, or transient effects, even in 'noisy' data.

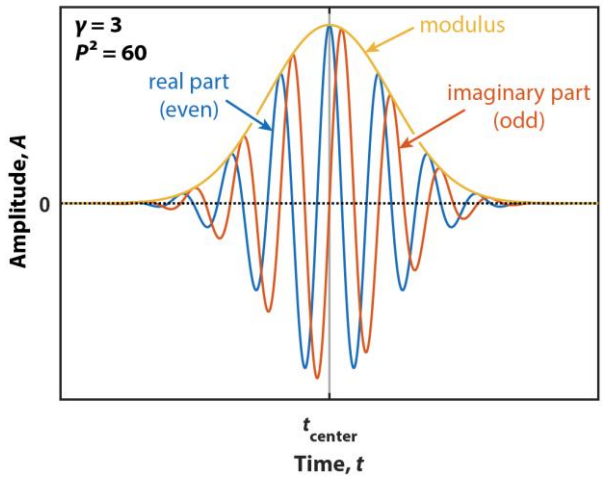

Figure 4.4 – The Morse wavelet. The Morse wavelet's shape is determined by two parameters: γ, the symmetry parameter, which dictates the symmetry of the wavelet about its center, and P^2, the time-bandwidth product, which is proportional to the wavelet duration in time. For the analytical wavelets used in the analysis in this work, γ = 3 was chosen because it corresponds to the maximum symmetry for Morse wavelets. P^2 = 60 was chosen for a sufficiently large number of oscillations within the wavelet's width to detect higher frequencies. Analytic wavelets like the Morse wavelet are complex-valued and thus contain real and imaginary components. Their Fourier transforms are only supported on the positive real axis.

Briefly, a continuous wavelet transform is a convolution of an input signal (in this case a time series) with a set of scaled wavelet functions generated by a 'mother wavelet',

typically using a fast Fourier transform algorithm. The mother wavelet is a packet of wave-like oscillations whose amplitude is maximal in the center of the wavelet and quickly approaches zero as $t \rightarrow \pm\infty$ (a Morse wavelet is shown in Figure 4.4). The mother wavelet can then be stretched or compressed (scaled) in time with respect to a complete orthonormal set of basis functions, creating a wavelet series whose individual functions have varying duration but consistent shape (and therefore varying frequency). An input signal is then convoluted piece-wise with each of the series' functions to determine the similarity, or 'coherence', of the signal with the given wavelet, thus extracting which frequencies are most coherent with the input signal at a given time. In contrast to the short-time Fourier transform algorithm, which obeys the time-frequency uncertainty principle, $\Delta t \Delta \omega \geq ½$, the scaling feature of the wavelet algorithm allows for both excellent time and frequency localization when determining the time-varying frequency components of an input signal. To calculate the wavelet transforms of friction traces in this work, the MATLAB (MathWorks, version 9.3 2017b) continuous wavelet transform function 'cwt' was used.

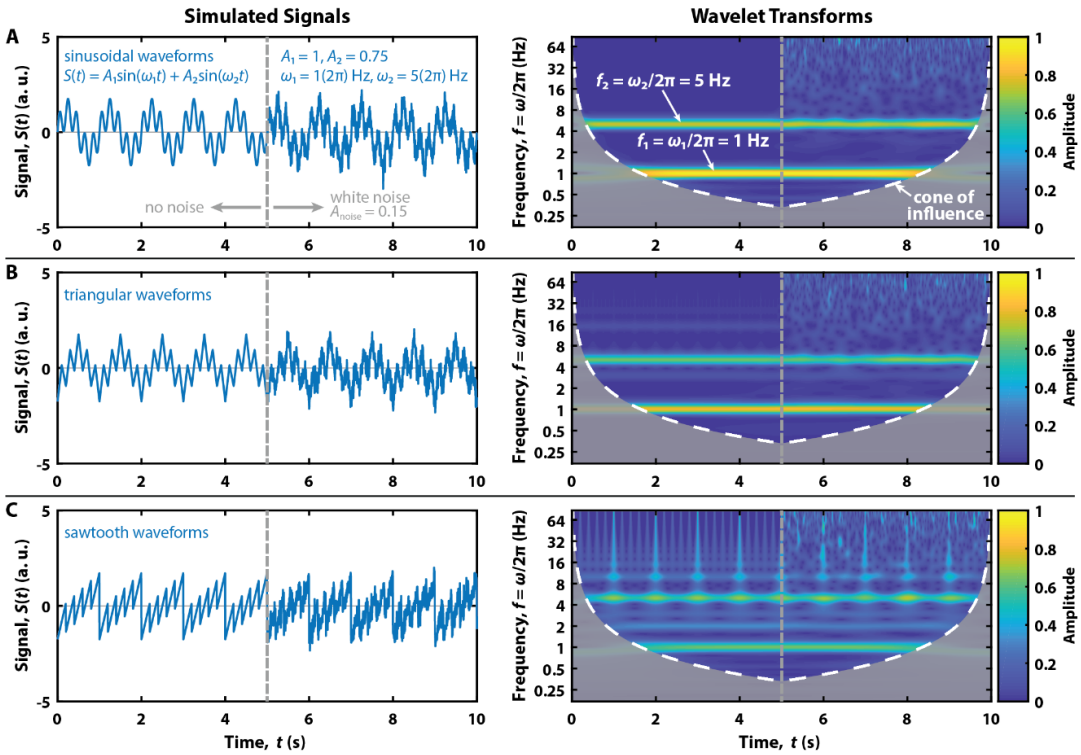

Figure 4.5 - Wavelet analysis of three different model signals. Simulated composite signals of frequencies f_1 = 1 Hz and f_2 = 5 Hz and amplitudes A_1 = 1 and A_2 = 0.75 have been generated for A. sine, B. triangle, and C. saw-tooth waveforms (left panels). At time t = 5 s, white noise with amplitude A_{noise} = 0.15 is introduced. The right panels illustrate the wavelet transforms of the time series on the left. The gray regions are the parts of the wavelet transform that fall outside of the 'cone of influence' (white dashed line), a boundary in time/frequency space where edge effects become significant [29]. A. The sine wave results in a large amplitude band at 1 Hz and 5 Hz in the wavelet transform. B. The triangle wave results in weaker amplitude bands compared to the pure sine wave with the emergence of vertical spikes and overtones due to the sharp discontinuities in the time series. C. The saw-tooth wave (resembling stick-slip) results in still lower intensity bands and demonstrates more intense vertical spikes and overtones. For all model signals, introduction of white noise does not fully degrade the features in the wavelet transforms.

To illustrate the information revealed from performing a wavelet transform on time-series data, several differently-shaped model waveforms with two constituent frequencies (f_1 = 1 Hz, f_2 = 5 Hz), and their corresponding wavelet transforms are shown in Figure 4.5. The amplitude of a given frequency contained in the time-series at a given time is plotted to provide a rich, detailed representation of the frequencies present.

Different waveform shapes have specific characteristic features in the wavelet transform, which are robust against noise. Most notably, as the characteristic waveform becomes more asymmetrical and 'sawtooth-like' (like stick-slip friction), more overtones and

vertical frequency ‘spikes’ are observed in the wavelet transform. Therefore, wavelet transforms of friction traces should not only be able to easily characterize their frequencies, but also qualitatively determine if such frequencies are resonant frequencies of the system (sinusoidal, device specific) or stick-slip oscillations due to surface interactions (saw-tooth, surface and lubricant specific).

4.3.6 Rheological measurements

Rheological measurements were conducted using a TA Instruments DHR-3 rheometer which is a combined motor and transducer instrument. The experiments conducted were stress controlled flow ramps using a 40-mm diameter cross-hatched stainless-steel parallel plate geometry. The cross hatched parallel plate configuration was selected to limit wall slippage. For each sample, two stress ramps were conducted as pre-conditioning experiments (similar to the friction experiment ‘sweep-out’ traces), to remove any initial internal structure of the films. The third stress ramp is reported for shear rates of 0 to 100 s^{-1}. Temperatures were controlled at 25 °C for all experiments.

4.4 Results and discussion

4.4.1 Friction vs. velocity at varying loads

Lubricating systems typically have velocity dependent friction forces. Over many orders of magnitude in velocity, it is not uncommon for the system to exhibit multiple increases and decreases (highs and lows) in the friction force traces (see Figure 4.6A for a schematic example). These increases and decreases in friction forces can usually be attributed to certain time- and length-scales characteristic to the molecular structure of the lubricant, surface features, and lubricant-surface interactions, which can be interpreted by the

Deborah number [30]. The Deborah Number, which is the relationship between the system's relaxation time(s) and the time over which an interaction occurs (is measured), can similarly be represented as the relationship between the velocity of a system and the characteristic velocity or velocities, defined as the characteristic distance(s) divided by their relaxation time(s) [31]. In complex systems, there can be multiple relaxation times and length scales, giving rise to multiple maxima and minima in the friction force over many orders of magnitude of velocity. Experimental studies on three samples that span different aspects of these phenomena are further discussed, as well as their relation to friction dynamics.

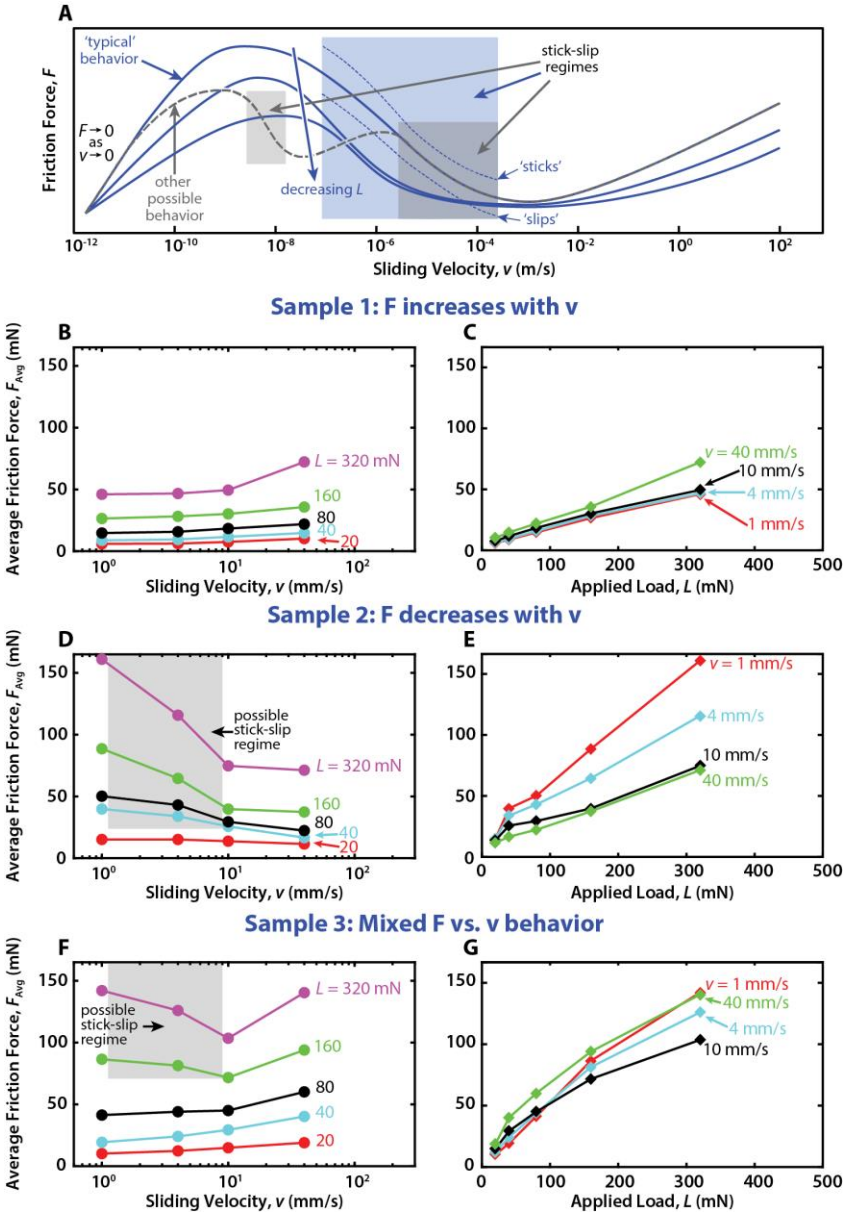

Figure 4.6 - Average friction force vs. sliding velocity (F_{avg} vs. v) at various loads, L, for three different samples. A. A schematic of a typical (blue) F vs. v relationship for two surfaces interacting with an intervening lubricating fluid. The prominent 'peak' at low velocities moves towards lower F and higher v as L is decreased. 'Stick-slip' regimes are shaded and can occur when dF/dv is negative. Dashed blue lines have been added in the 'stick-slip' regime for the 'typical' curve with the highest load to illustrate the stick-slip deviations/fluctuations from the average friction force. Other relationships with many peaks in F as v increases – arising from systems with multiple characteristic relaxations timescales– may also be observed, leading to multiple stick-slip and smooth sliding regimes at different velocities. As the velocity approaches zero, at a finite temperature, due to the relaxation times and bond lifetimes of the materials in the interacting surfaces and the fluid medium, thermal energy will allow the system to relax in a (nearly) force-free way and little to no friction force will be measured. B,C. Sample 1 exhibits increasing F_{avg} with v for all L and an approximately linear F_{avg} vs. L relationship. D,E. Sample 2 exhibits decreasing F_{avg} with v for all L and a non-linear F_{avg} vs. L relationship, especially at lower velocities. F,G. Sample 3 exhibits a mix of increasing and decreasing F_{avg} with v for different L. The extent of stick-slip depends on the stiffness of the sensing mechanism.

4.4.2 Sample 1: Typical viscous fluid

The first lubricant studied behaves as a typical viscous fluid in the velocity regime from 1 mm/s to 40 mm/s. As seen in Figure 4.6B, this fluid exhibits a gradual increase in the friction force with increasing shear velocity for all applied loads, indicating that in this load and velocity regime, the viscosity of the fluid dominates the friction behavior as in hydrodynamic lubrication [32] and as is typically seen in shear experiments at higher velocities (refer to high velocity regime in Figure 4.6A schematic). With increasing velocity, there is more resistance to shear due to the viscosity of the fluid, and thus the friction (strictly, lubrication) force increases. This type of lubrication force can be described by Couette flow, $F_{\parallel} = \eta A V_{\parallel}/D$, for two parallel plates of area A at separation D moving at relative velocity $V_{\parallel}$, where η is the bulk viscosity of the lubricating fluid. The friction vs. load curves, shown in Figure 4.6C, are linear and extrapolate through the origin (0,0), indicating there is no adhesion contribution to the friction force which is therefore strictly load and velocity dependent.

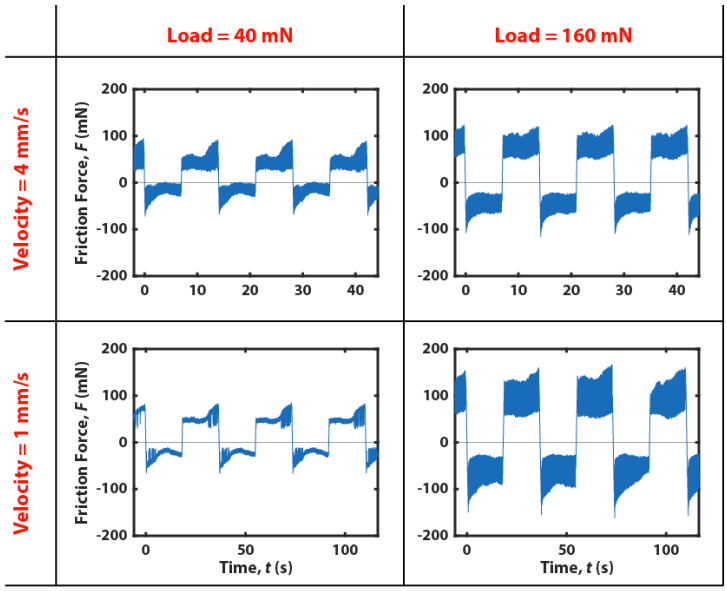

Figure 4.7 - Friction traces as a function of load and velocity for Sample 2. The breadth of the friction signal at higher loads and velocities is indicative of resonant or stick-slip response.

4.4.3 Sample 2: Stick-slip exhibiting fluid

The friction forces measured using Sample 2 as a lubricant (Figure 4.6D,E) exhibit the opposite trend with velocity as compared to Sample 1. The friction force decreases with increasing velocity in the same velocity and load regime as Sample 1, with a sharp decrease at higher loads (160-320 mN, Figure 4.6D). However, between 10 and 40 mm/s the friction force remains relatively constant. The steep decrease in friction force with sliding velocity may indicate a region where stick-slip friction is expected [33–35]. The stick-slip response in this regime is therefore analyzed further with wavelet transforms (Figure 4.8 and Figure 4.9). Figure 4.7 shows plots of the friction traces for Sample 2 as a function of load and velocity where the breadth in F of a given uni-directional sliding event indicates stick-slip oscillations in the friction force. The friction vs. load curves are not completely linear, as displayed in Figure 4.6E. Rate-dependent viscous effects (shear-thinning) may explain why the friction force is higher at lower velocities. The surfaces may be moving slower than the characteristic time and length scale of the adhesive bonds between the fluid and surfaces, giving rise to higher friction forces at lower velocities. As the load is decreased, the steepness of the average friction as a function of velocity is reduced. These effects of load, and sliding speed, combined with the effects of temperature, and the elasticity of the system (including the surfaces, intervening fluid, and force-measuring springs) are inter-related in a complex way. In general, decreasing the load makes the lubricant more liquid-like: the maximum in the friction force decreases and is observed at higher velocities, and the negative slope regime decreases in magnitude and extent (its width in velocity space). The magnitude of the stiction spikes in the stick-slip regime now decrease, as does the velocity range over which stick-slip can be observed. These effects of load on the shape of the F vs. v curve (Figure 4.6D) as well

as the stick-slip magnitude and stick-slip velocity regime (Figure 4.9) are observed for Sample 2.

4.4.4 Sample 3: Mixed behavior fluid

Sample 3 exhibits two different regimes of friction behavior at different loads (Figure 4.6F,G). At low loads, the friction force increases with increasing velocity (similar to Sample 1), yet at higher loads (160-320 mN) there is an initial decrease in friction force from 1-10 mm/s and then an increase. Structural changes of the fluid components upon higher compression may lead to the differing velocity and load dependence, thus affecting the force required to shear and time allowed for molecular rearrangements and alignment [36]. Other time-associated effects due to repeated shear at the same contact could also explain the variable trends with load [37]. This fluid shows an example of how testing multiple loads can exhibit drastically different friction forces compared to many studies that produce a Stribeck curve for only one load. Also, a simple friction coefficient would not be effective to describe the friction behavior in this fluid since the relation between friction and load (Figure 4.6G) is non-linear. As was interpreted for Sample 2, it appears the F_{avg} vs. v curve is shifted towards lower F and higher v as the load is decreased during shearing.

4.4.5 Wavelet interpretation and implications

The friction traces for Sample 2 and their wavelet transforms are presented in Figure 4.8. Sample 2 was selected for wavelet analysis due to the richness of stick-slip, oscillatory, and smooth sliding behavior exhibited at different loads and velocities. The steep negative trends in the F_{avg} vs. v (for all L), along with the stiffness of the system, is a likely indicator of stick-slip sliding. Figure 4.8A shows that at low load and velocity (L = 20 mN, v = 4 mm/s), the only frequency component present in the friction trace is a pure sinusoidal

oscillation at 120 Hz, indicative of mechanical resonance in the system. The horizontal band in the wavelet transform is steady and displays no significant overtones. Considering the F_{avg} vs. v plot of Sample 2 in Figure 4.6D, the lack of stick-slip friction at this load and velocity is not surprising because the friction is nearly constant with increasing velocity at this load. Increasing the load to L = 80 mN at v = 4 mm/s, a combination of load and velocity which lies within a negative slope in Figure 4.6D causes the system to exhibit both mechanical resonance (160 Hz) and stick-slip sliding (26 Hz) responses (Figure 4.8B). The strong horizontal band in the wavelet transform is the fundamental stick-slip frequency which causes overtones at each slip event. The overtones cannot be sustained above the 160 Hz mechanical frequency, because all of the vibration energy is dissipated within the system's resonance vibrations. Finally, increasing the load to L = 160 mN at v = 1 mm/s damps out most of the mechanical resonance in the system and results in a high amplitude stick-slip friction response with a fundamental frequency of approximately 5 Hz (Figure 4.8C). Overtones are clearly visible in the wavelet transform as weaker horizontal bands at higher frequencies. Figure 4.8D-F show wider sweeps in θ during which more complicated friction dynamics are observed, including switching modes from stick-slip to resonance vibrations (Figure 4.8D,E) and gradual changes in stick-slip frequency (Figure 4.8F). The richness of this information is not easily evaluated without applying a wavelet transform to the time series. The stick-slip frequencies and amplitudes are easily extracted from these types of analyses and may be modeled as predictors for various surface phenomena associated with friction in complex systems.

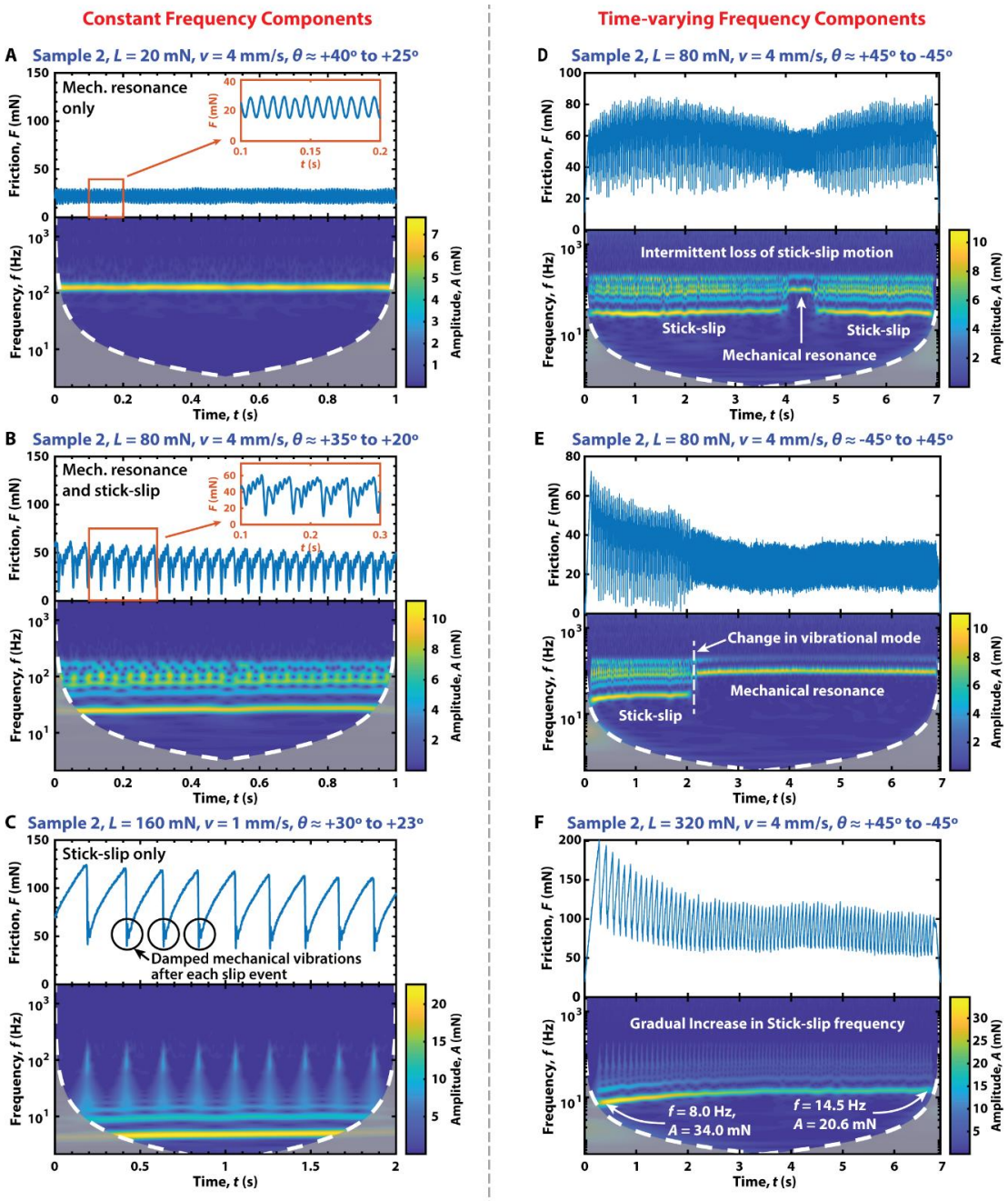

Figure 4.8 - Representative friction traces for Sample 2 and the corresponding wavelet transforms. displaying different frequency components at varied loads and velocities. Panels A-C depict smaller angle traces where system fluctuations are constant with time and Panels D-F show full 90° sweeps (~24 mm) with more complex time-dependent behavior. (Note: Panel E is the reverse sliding direction of Panel D for the same applied load, L = 80 mN, and velocity, v = 4 mm/s) A. (L = 20 mN, v = 4 mm/s) Pure mechanical resonance is observed at 125 Hz with no observable stick-slip. B. (L = 80 mN, v = 4 mm/s) Mechanical resonance of approximately 100 Hz is imposed on a saw-tooth (stick-slip) signal at 26 Hz. C. (L = 160 mN, v = 1 mm/s) A stick slip signal at approximately 5 Hz is clearly characterized by a horizontal band and prominent vertical spikes and overtones. Note the mechanical resonance which is seen at the instant the surfaces slip apart after each stick event. These vibrations are damped out within milliseconds of further sliding. D. The full trace from Panel B is shown. Between t = 4 and t = 5 s, the mode of sliding briefly changes to sinusoidal mechanical resonance before returning to stick-slip motion. E. The reverse sliding direction of Panel D shows a transition to mechanical resonance at approximately the same location as the transition at t = 5 s in Panel D (t = 2 s in Panel E

corresponds to the same rotation angle as t = 5 s in Panel D), however, the mode of sliding does not return to stick-slip when sliding in this direction. F. (L = 320 mN, v = 4 mm/s) A gradual increase in stick-slip frequency from f = 8.0 Hz to f = 14.5 Hz is observed accompanied by a decrease in stick-slip amplitude by approximately 11.5 mN.

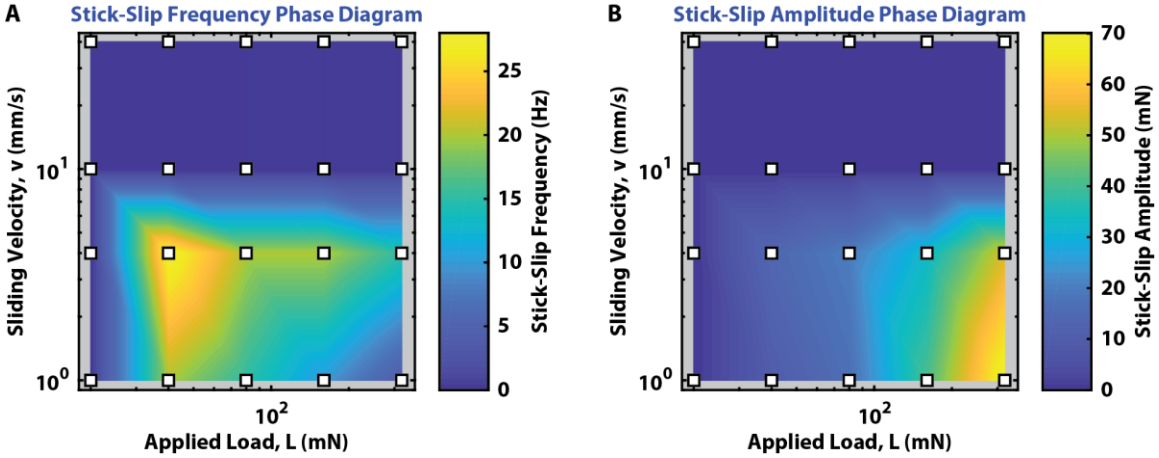

Figure 4.9 - Applied load vs. sliding velocity (L vs. v) phase diagrams for A. average stick-slip frequency response and B. stick-slip amplitude for experiments on Sample 2. White squares indicate the combinations of applied load and velocity measured to generate each phase diagram. Colored shading is generated by linearly interpolating between measured values.

A summary of the stick-slip response at different loads and velocities for Sample 2 is presented in Figure 4.9, showing both the fundamental stick-slip frequencies (Figure 4.9A), and the stick-slip amplitudes (Figure 4.9B). This summarizing stick-slip 'phase diagram' can be easily generated for any materials system by algorithmically interpreting the wavelet transforms of friction traces at various loads and velocities. Because stick-slip friction can cause damage and wear in lubricated and non-lubricated systems, this type of rapid analysis may prove to be important for quickly evaluating the efficacy of lubricants at varying sliding parameters.

4.5 Conclusions

Friction can exhibit complex behavior when examining different parameters such as load and velocity, especially when considering transient or dynamic effects. We have designed and created a rotating disk (ball on disk tribometer) attachment for the SFA that

allows for friction to be measured at velocities ranging from mm/s to m/s with applied loads from 0.1 mN to tens of newtons (corresponding to contact pressures of kilopascals to megapascals). Friction forces from 0.1 mN to tens of newtons can be measured with 0.1 mN sensitivity. Wavelet transforms were used to extract the rich, dynamic frequency response contained within the friction traces. The wavelet transform method for analyzing friction data allows for mechanical resonances to be rapidly and unambiguously differentiated from stick-slip sliding and can also measure other high-frequency transient effects. These combined techniques were used to study several complex fluids that exhibit viscous, stick-slip, smooth sliding, and mixed frictional behaviors. The rotating disk combined with wavelet analysis can be used for other applications involving high speed friction and dynamic adhesion, including damage and wear evaluation and sensory perception studies.

4.6 References

1. Luengo, G., Tsuchiya, M., Heuberger, M., Israelachvili, J., Thin Film Rheology and Tribology of Chocolate. *J. Food Sci.* 62, 767–812 (1997)

2. Kragel′skiĭ, I.V., Dobychin, M.N., Kombalov, V.S., *Friction and wear: calculation methods*. Pergamon Press (1982)

3. Sivamani, R.K., Goodman, J., Gitis, N. V., Maibach, H.I., Friction coefficient of skin in real-time. *Ski. Res. Technol.* 9, 235–239 (2003)

4. Nacht, S., Close, J.-A., Yeung, D., Gans, E., Skin friction coefficient: changes induced by skin hydration and emollient application and correlation with perceived skin feel. *J. Soc. Cosmet. Chem.* 32, 55–65 (1981)

5. Braun, O., Peyrard, M., Dependence of kinetic friction on velocity: Master equation approach. *Phys. Rev. E*. 83, (2011)

6. Ben-David, O., Fineberg, J., Static Friction Coefficient Is Not a Material Constant. *Phys. Rev. Lett.* 106, 254301 (2011)

7. Blau, P., The significance and use of the friction coefficient. *Tribol. Int.* 34, 585–591 (2001)

8. Masjuki, H., Maleque, M., Investigation of the anti-wear characteristics of palm oil methyl ester using a four-ball tribometer test. *Wear*. 206, 179–186 (1997)

9. Gallardo-Hernandez, E., Lewis, R., Twin disc assessment of wheel/rail adhesion. *Wear*. 265, 1309–1316 (2008)

10. Burris, D.L., Sawyer, W.G., Addressing Practical Challenges of Low Friction Coefficient Measurements. *Tribol. Lett.* 35, 17–23 (2009)

11. Godfrey, D., Friction oscillations with a pin-on-disc tribometer. *Tribol. Int.* 28, 119–126 (1995)

12. Ogletree, D.F., Carpick, R.W., Salmeron, M., Calibration of frictional forces in atomic force microscopy. *Rev. Sci. Instrum.* 67, 3298 (1996)

13. Stribeck, R., Characteristics of plain and roller bearings. *Zeit. Ver. deut. Ing.* 46, 1341–1348 (1902)

14. Jacobson, B., The Stribeck memorial lecture. In: Tribology International. pp. 781–789. Elsevier (2003)

15. Feeny, B., Guran, A., Hinrichs, N., Popp, K., A Historical Review on Dry Friction and Stick-Slip Phenomena. *Appl. Mech. Rev.* 51, 321 (1998)

16. Howe, R.D., Cutkosky, M.R., Sensing skin acceleration for slip and texture perception. In: Proceedings, 1989 International Conference on Robotics and Automation. pp. 145–150. IEEE Comput. Soc. Press

17. Sanahuja, S., Upadhyay, R., Briesen, H., Chen, J., Spectral analysis of the stick-slip phenomenon in “oral” tribological texture evaluation. *J. Texture Stud.* 48, 318–334 (2017)

18. Giasson, S., Israelachvili, J., Yoshizawa, H., Thin Film Morphology and Tribology Study of Mayonnaise. *J. Food Sci.* 62, 640–652 (1997)

19. Ibrahim, R.A., Friction-Induced Vibration, Chatter, Squeal, and Chaos—Part II: Dynamics and Modeling. *Appl. Mech. Rev.* 47, 227 (1994)

20. Tas, N., Sonnenberg, T., Jansen, H., Legtenberg, R., Elwenspoek, M., Stiction in surface micromachining. *J. Micromech. Microeng*. 6, 385–397 (1996)

21. Lee, D.W., Banquy, X., Israelachvili, J.N., Stick-slip friction and wear of articular joints. *Proc. Natl. Acad. Sci. U. S. A.* 110, E567-74 (2013)

22. Daubechies, I., The wavelet transform, time-frequency localization and signal analysis. *IEEE Trans. Inf. Theory*. 36, 961–1005 (1990)

23. Grossmann, A., Kronland-Martinet, R., Morlet, J., Reading and Understanding

Continuous Wavelet Transforms. In: Wavelets. pp. 2–20. Springer, Berlin, Heidelberg (1990)

24. Liang, J.W., Feeny, B.F., Wavelet analysis of stick-slip in an oscillator with dry friction. In: ASME Design Engineering Technical Conferences (1995)

25. Sadegh, H., Mehdi, A.N., Mehdi, A., Classification of acoustic emission signals generated from journal bearing at different lubrication conditions based on wavelet analysis in combination with artificial neural network and genetic algorithm. *Tribol. Int.* 95, 426–434 (2016)

26. Lowrey, D.D., Tasaka, K., Kindt, J.H., Banquy, X., Belman, N., Min, Y., Pesika, N.S., Mordukhovich, G., Israelachvili, J.N., High-Speed Friction Measurements Using a Modified Surface Forces Apparatus. *Tribol. Lett.* 42, 117–127 (2011)

27. Olhede, S.C., Walden, A.T., Generalized Morse wavelets. *IEEE Trans. Signal Process.* 50, 2661–2670 (2002)

28. Daubechies, I., Paul, T., Time-frequency localisation operators-a geometric phase space approach: II. The use of dilations. *Inverse Probl.* 4, 661–680 (1988)

29. Mallat, S., *A Wavelet Tour of Signal Processing*. London Academic Press (1999)

30. Reiner, M., The Deborah Number. *Phys. Today*. 17, 62–62 (1964)

31. Israelachvili, J.N., *Intermolecular and Surface Forces: Revised Third Edition*. Academic Press (2011)

32. Bowden, F.P., Tabor, D., *The friction and lubrication of solids*. Clarendon Press (2001)

33. Berman, A.D., Ducker, W.A., Israelachvili, J.N., Origin and Characterization of Different Stick−Slip Friction Mechanisms. *Langmuir*. 12, 4559–4563 (1996)

34. Yoshizawa, H., Israelachvili, J., Fundamental mechanisms of interfacial friction. 2. Stick-slip friction of spherical and chain molecules. *J. Phys. Chem.* 97, 11300–11313 (1993)

35. Brockley, C.A., Ko, P.L., Quasi-Harmonic Friction-Induced Vibration. *J. Lubr. Technol.* 92, 550 (1970)

36. Luengo, G., Israelachvili, J., Granick, S., Generalized effects in confined fluids: new friction map for boundary lubrication. *Wear*. 200, 328–335 (1996)

37. Börzsönyi, T., Szabó, B., Törös, G., Wegner, S., Török, J., Somfai, E., Bien, T., Stannarius, R., Orientational Order and Alignment of Elongated Particles Induced by Shear. *Phys. Rev. Lett.* 108, 228302 (2012)

5 Automated measurements of hair-hair single-fiber adhesion

5.1 Abstract

The adhesion force between individual hair fibers is measured by observing, with optical video microscopes, the natural bending and adhesive jumps out of contact of individual hair fibers interacting in a cross-hair geometry. The hair fibers' natural elastic responses, calibrated by measuring their natural resonant frequencies, were used to measure the forces. Using a custom-designed, automated apparatus to measure thousands of individual hair-hair contacts along millimeter length scales of hair, it was found that a broad, yet characteristic, spatially-variant distribution in adhesion force is measured on the 1 to 1000 nN scale for both clean and conditioner-treated hair fibers. Comparison between the measured forces and forces modeled from the hairs' surface topography (measured using confocal laser profilometry) are in good order-of magnitude agreement and have similar breadth and shape. The agreement between the measurements and the model suggests, perhaps unsurprisingly, that hair-hair adhesion is governed, under a first approximation, by the unique surface structure of the hairs' cuticles and, therefore, the large distribution in local mean curvature at the various individual contact points along the hairs' lengths. We posit, therefore, that hair care products could best control the surface properties (or at least the adhesive properties) between hairs by directly modifying hair microstructure via the controlled deposition of well-defined micro-/nanoparticles.

5.2 Introduction

Healthy, shiny, smooth, and soft hair is desired by many people in different cultures around the world. However, due to aging from mechanical and chemical damage, the

morphology and chemistry of the hair fibers' layered outer cuticles become non-uniform and deviate from their natural virgin properties [1, 2]. To mask or otherwise reverse the effects of this aging, hair products, such as conditioners and other chemical treatments, have been designed to modify hair surfaces with lipid monolayers or adsorbed polymers, such as silicones and waxes [3]. These surface-modifying layers can range in thickness from 1s to 100s of nanometers and function by changing the surface energy and/or normalizing the micro-/nano-structure of hairs' outer layers [4, 5]. Due to the biodiversity of human hair across various ethnicities, cultures, and age groups, formulating hair care products which can accomplish these tasks with similar efficacy, independent of the individual using the product, is a significant technological challenge [3]. It is also difficult to predict how surface treatments will influence the overall 'manageability' of an individual's unique head of hair.

Within the last 15 to 20 years, evaluating the efficacy of hair care products has involved correlating consumer surveys regarding the look and feel of untreated and treated hairs (both virgin and damaged) with the treatments' formulas and their effect on the hairs' surface properties, such as friction and adhesion [1, 2, 4–8]. Much of the previous work on characterizing the surface properties of hair, especially hair adhesion, has been conducted using asymmetrical systems whereby atomic force microscope (AFM) cantilevers with high (10s of nm radii) and low (10s of μm radii) curvature tips are rasterized around small areas of the hairs' surfaces [1, 2, 5, 6, 9–14]. From these experiments, the spatial variations in surface energies of treated and untreated, virgin and damaged hair can be calculated.

To use the information gained from conducting microscopic physical measurements in a more cost-effective and rapid way, it would be useful to somehow translate the physical information to accurate computer models, in which full heads of hair can be simulated and

altered according to damage and treatment. However, due to the complexity of the cuticle geometry, it is difficult to extrapolate these microscopic measurements to model the behavior of full heads of hair [15], with millions of individual fiber-fiber interactions, without explicitly defining such structure – a task that is computationally prohibitive. It is therefore necessary to symmetrically measure the forces between fibers, and not just between fibers and idealized probes, to gain a better understanding of how the nanoscopic surface properties of hair scale to the mesoscopic behavior of the physiologically relevant system.

Symmetrical hair-hair adhesion and friction experiments have previously been conducted by other research groups by affixing short segments of hair to the ends of tip-less AFM cantilevers [16–19]. Though this method can achieve ~10 pN normal and lateral force resolution, it requires painstakingly precise manipulation of small hair segments whose ends must be cut using either lasers [16] or focused ion beams [17–19] to avoid edge interactions within the AFM.

In this work, to overcome the limitations caused by this complicated sample preparation and the previously discussed minimal range-of-motion available in AFMs, we present an apparatus specifically designed for measuring the adhesion force between fibers, which uses one of the interacting fibers as the force probe (Figure 5.1A). Similar assays have been used to measure the friction and adhesion of natural fibers [20] and polymer fibers [21–23], but the natural fiber experiments have been limited to the use of carbon or polymer probes. In the present work, the probe hair fibers are calibrated using various methods – including i) simply hanging weights of known mass from the end of the probe fiber, ii) deflecting the fiber against another well-calibrated spring of known constant, and iii) measuring both the free mass and the natural resonant frequency of the probe fiber – which

all agree within < 10% variation. Sufficiently long (2 to 3 cm) probe fibers can achieve effective spring constants at their free ends in the ~1 mN/m (1 nN/μm) range, which is 10^6 and 10^2 times weaker than typical SFA and AFM cantilevers, respectively [24–26]. These weak spring constants allow for the measurement of adhesion forces as low as 1 nN by using a simple, low-resolution video microscope to measure the adhesive jumps-out of contact with ~1 μm resolution.

Adapting the above method for use in a traditional SFA Mark II (SurForce LLC) and taking advantage of the SFA's pre-existing ability to electronically actuate the motion and relative positions of both fibers with sub-micron accuracy, we can reproducibly measure the adhesion force between highly-localized contact regions on each hair and automatically sample thousands of individual contact locations to generate overall and spatially-resolved adhesion force distributions. The magnitudes, and to some extent the shapes, of these distributions are reproducible and are predicted in this work from a model leveraging a combination of surface-topography measurements using laser profilometry and surface energy measurements via fiber tensiometry [27]. The agreement between the measured and modeled adhesion forces suggests that surface topography is the main cause of the large distributions in adhesion force. We therefore suggest that future hair care products may take advantage of this phenomenon by strategically controlling the surface morphology of hair fibers by depositing well-defined layers of microparticles whose geometry has been tuned for a specific purpose.

5.3 Methods

5.3.1 The experimental apparatus

The experimental apparatus used for this work, dubbed the Hair Adhesion Force Apparatus (HAFA, Figure 5.1), uses the main chamber, coarse *z*-control, and friction device top mount from a standard SFA Mark II (SurForce LLC). The SFA has been modified to accommodate a manual motion assembly – including *y*- and *x*-translation stages and a θ_x rotational stage – to which the probe hair is mounted. Figure 5.1 shows both photos and a schematic of the HAFA and the mounted hairs, defining the coordinate system and specifying the directions which the probe and fixed hairs are automatically actuated. Also shown are the optical axes and views from the top- and side-view cameras.

The main premise of the HAFA technique, and the basis for the modifications to the SFA Mark II, is that a single, fairly-straight human hair fiber, when fixed at one end, functions as an elastic cantilever beam with elliptical cross-section (discussed further in Section 5.3.3). The free end of this 'probe hair' is allowed to interact with the surface of another fixed hair fiber in a crosshair configuration (angle between hair axes, $\theta \approx 90°$) and is viewed from the positive *z*- and *x*-directions, as defined in Figure 5.1A, during this interaction. After carefully calibrating the probe hair's spring constant (Section 5.3.3), the adhesion force between the fibers is calculated by measuring the jump-out distance between the hairs after they separate under tension following adhesive contact (Section 5.3.2).

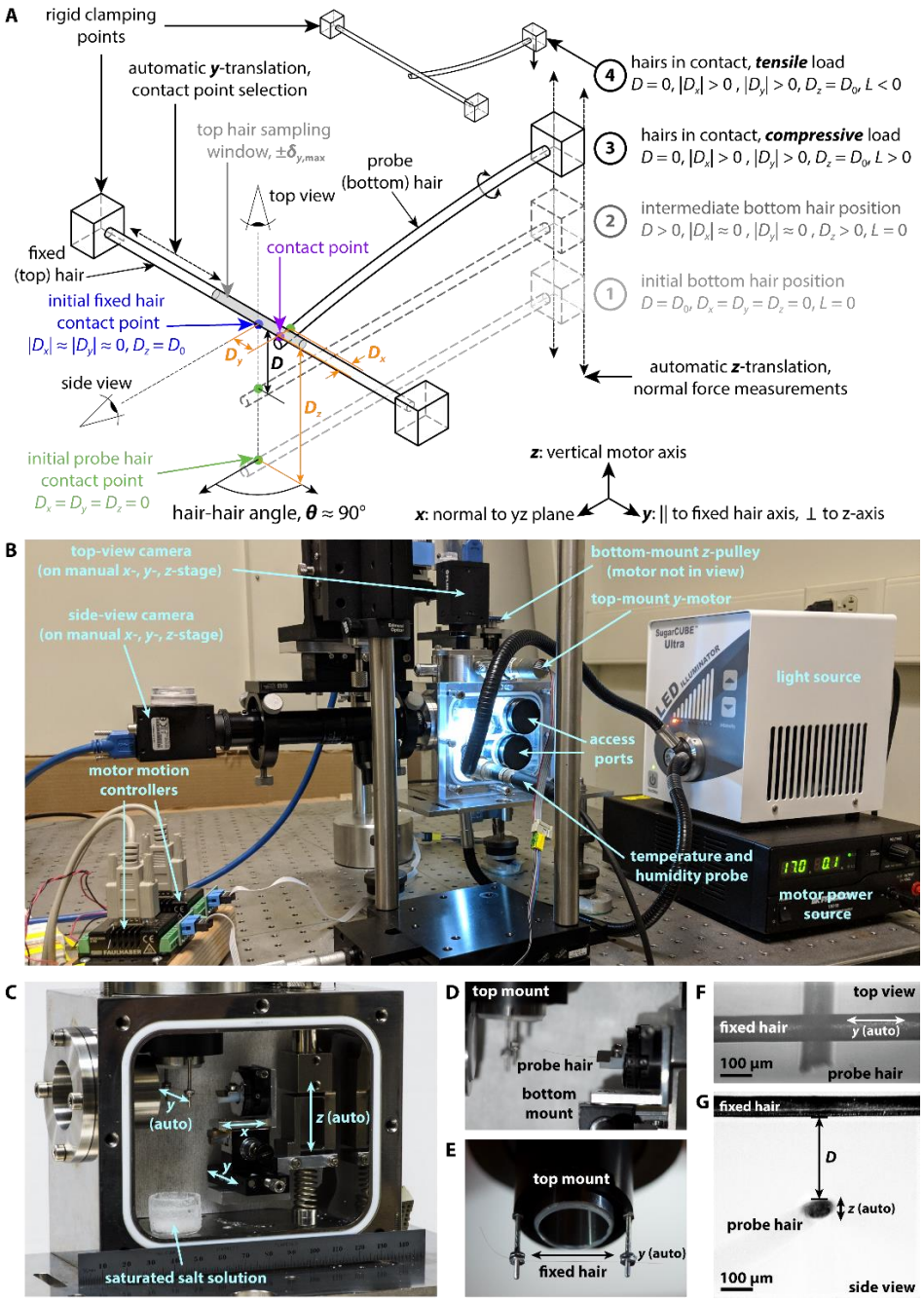

Figure 5.1 - Schematic and photos of experimental hair adhesion force apparatus. A) A schematic representation of the two interacting hair fibers on their respective mounts and translational stages. The probe hair is depicted in 4 states, 1) its initial position out of contact, 2) an intermediate position during approach towards contact, 3) under compressive load while in contact (the contact position on both the probe and fixed hair may have changed from the green and blue circles to the purple circle during compression), 4) under tensile load while in contact before an adhesive jump out. Also shown are the definitions for the coordinate system, the views from the top- and side-view cameras, and the definitions of the relative *x*-, *y*-, and *z*-positions, D_x, D_y, and D_z, of the probe hair with respect to its initial position, and the hair-hair separation distance, D. B) A labeled photograph of the overall HAFA setup. C) A photograph of the inside of the HAFA chamber depicting the various motion control components for the probe hair. D,E) Photographs of the bottom and top mounts with hairs affixed. F,G) Micrographs from the top- and side-view cameras depicting the probe and fixed hairs out of contact at some separation distance, D.

Discussed further in Sections 5.3.4-5.3.6, the HAFA also allows for control of various interaction timescales and velocities using computer controlled motors which move both the probe hair in the *z*-direction and the fixed hair in the *y*-direction. The HAFA, as with all SFAs, is enclosed in an environmentally controlled chamber whose temperature is equilibrated with a water-cooled experimental room and whose humidity is controlled using a saturated salt solution within the chamber. For the experiments presented in this chapter, the temperature and relative humidity were set at 25 °C and 65%, respectively, and monitored with a computer-connected Rotronic HCA2-S temperature and humidity probe.

5.3.2 Hair detection and distance measurements

Before assigning real-space distances to any objects in either microscope video feed, the microscopes must be calibrated at their focal planes. This was done for each microscope by focusing on a graticule with lines spaced at 100 μm and counting the average number of video pixels between the centers of the grating lines. For all experiments, the focal planes of the side- and top-view cameras are centered at the middle-most cross-section of the fixed hair perpendicular to the viewing direction. The calibrated and focuses video feeds are then auto-contrast adjusted so that the top and bottom 1% of all pixel values are saturated. Then, manually-selected values for an isotropic gaussian filter radius, oversaturation filter (essentially a multiplication factor), and Sobel edge detection threshold are applied, forming a binary image of 'kept' pixels which denote pixels near the edge of all objects (hairs) in the image. Distances between specified pixels in these binary images are then calculated (Figure 5.2).

In the side-view video stream, the bottom edge of the probe hair and the top edge of the fixed hair are found by averaging the positions of the pixels within specified *z*-distances

of the extreme top and bottom edges of the 'kept' pixels. The difference between these two locations is tracked with time and is represented in Figure 5.2A. The distance between the hairs, *D*, is therefore taken as this difference minus the minimum value of this difference. The *y*-position of the probe is taken as the average *y*-position of the pixels near the extreme bottom edge of the probe (Figure 5.2A).

In the top-view video stream, a similar image processing algorithm is applied. The *x*-position of the probe is taken as the average *x*-position of the pixels near the free tip of the probe relative to the average *x*-position of the pixels at the far side (negative *x*) of the fixed hair. The *y*-position of the probe is taken as the average *y*-position of the same pixels used to calculate the *x*-position in the top-view camera. Tracking the position of the probe hair in this manner allows for real-time tracking of the probe hair in all three spatial dimensions, thus fully defining its motion.

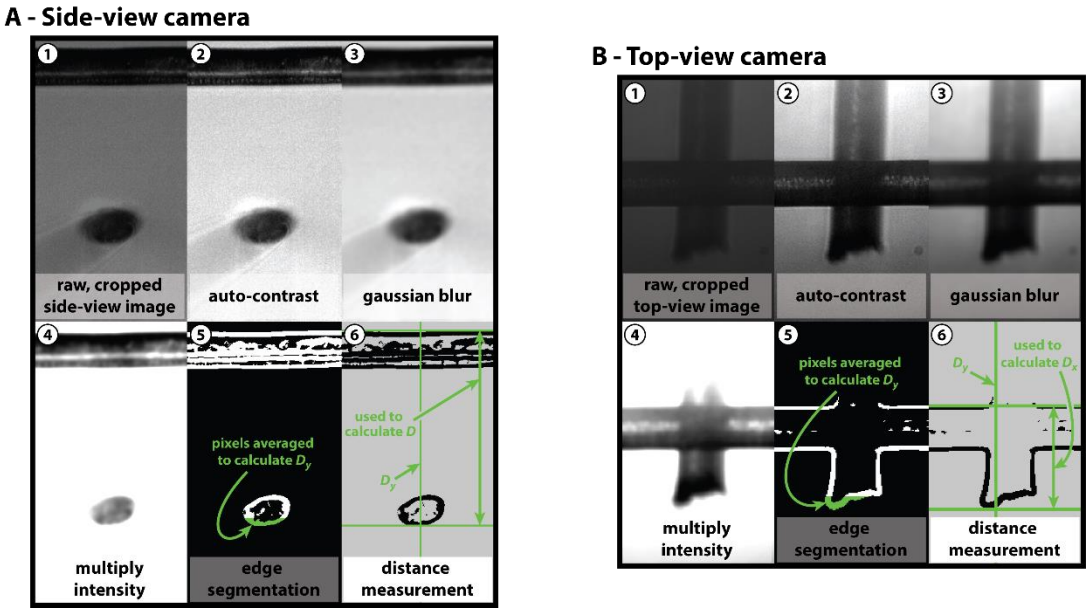

Figure 5.2 – Image processing and distance measurements. Image processing steps (1-6) and distances calculations performed on A) side-view and B) top-view video frames.

5.3.3 Hair spring constant calibration methods

Treating the bottom free hair fiber as a simple cantilever beam with elliptical cross-section whose minor axis is parallel to the *z*-direction, the deflection of the tip of the beam in the *z*-direction, Δz, is related to the force, *L*, applied to or by the cantilever to achieve that deflection by the relationship:

$$L = k\Delta z \tag{5.1}$$

where *k* is the effective spring constant of the hair normal to the direction of deflection at the point where the force is being applied. If the force is applied very near the tip of the hair, then *k* is related to the dimensions and elastic properties of the cantilever by the relationship:

$$k = E\left(\frac{3\pi}{4}\right)\left(\frac{a^3 b}{l^3}\right) \tag{5.2}$$

where *E* is the elastic modulus of the hair, *a* and *b* are the minor and major radii of the elliptical cross-section, respectively, and *l* is the free length of the hair fiber.

Previous experiments [17] have measured the adhesion force between hair fibers to be of the order 100 nN. Therefore, to measure subtle variations in adhesion force, a force resolution of ~1 nN is necessary. A simple 10x microscope objective with a numerical aperture (NA) of 0.25 has an optical resolution of ~1 μm when paired with a camera having sufficiently small pixels. Therefore, the spring constant, *k*, of the free hair must be ~1-10 nN/μm, or ~1-10 mN/m, to measure these subtle forces using the adhesive jump-out distances from contact, D_{jump}. For a typical Caucasian hair fiber, $a \approx$ 20-40 μm, $b \approx$ 30-50 μm, and $E \approx$ 1-10 GPa. Therefore, to achieve a spring constant of ~1 nN/μm, the hair length must be between 1 to 3 cm. As such, the experimental apparatus has been designed so that the manual *x*-translation stage to which the probe hair is mounted can accommodate hairs between 1 and 4 cm in length.

Using these guidelines to design the system insures the probe hairs are close to the appropriate spring constant, however each fiber must be physically calibrated before the adhesion force can be measured. The three methods for determining the spring constant employed in this work, which are internally consistent within roughly 10% variance, are detailed below. Because of the similarities between each method, for most of the experiments presented in this work, the 'resonant frequency' method in Section 5.3.3.3 was used.

5.3.3.1 Suspended masses

The most conceptually straight-forward way of calibrating the spring constant of the probe hair is by hanging from its end small weights of known mass. Small coils of 96-μm-diameter Nylon fishing line of various total lengths were used for this purpose and were massed using a Mettler Toledo UMX2 microbalance (±0.1 μg). The slope of the best fit line, passing through the origin, of the deflection of the probe hair, D_z, vs. the weight of the masses, w, is taken as the spring constant. This method is however the most difficult to implement in practice. Figure 5.11 in Appendix A, Section 5.7, shows the calibration of a hair used to validate this method as well as a nylon and PVC reference spring used for the calibration method described in the next section.

5.3.3.2 Reference spring

Alternatively, the hair may be calibrated against a reference cantilever of known spring constant (which can be calibrated by either of the methods described above or below). This method involves moving the probe hair at a constant z-velocity while tracking both the z-position of the probe hair and the z-position of the reference spring. It is straightforward to show that the spring constant of the probe hair is given by:

$$k = k_{ref} \frac{v_{a,c}}{v_a - v_{a,c}} \tag{5.3}$$

where k_{ref} is the spring constant of the reference spring, $v_{h,free}$ is the free velocity of the probe hair out of contact with the reference spring, and $v_{h,contact}$ is the velocity of the probe hair (and subsequently the reference spring) in contact. Two reference springs were used in these experiments: i) a segment of the same nylon fishing line used to fashion the hanging masses in the previous section, ii) a shim of poly(vinyl chloride) (PVC) measuring approximately 50 μm thick, 500 μm wide, and 18 mm long. The reference springs were calibrated using the 'suspended masses' method and their calibration curves and spring constants are given in Figure 5.11.

This method, though reproducible, is greatly affected by the relative orientations of the probe hair and the reference spring and could potentially damage the contact region of the probe hair due to sliding between the hair and reference spring during loading and unloading. It is also limited by the accuracy with which the reference spring has been calibrated.

5.3.3.3 Fundamental resonant frequency

Finally, the method used for most of the presented adhesion force measurements involves using a high-speed camera (~300 frames per second) to measure the fundamental resonant frequency of the probe hair as it freely vibrates after an adhesive jump out. Treating the probe hair as a cantilever beam with a uniform elliptical cross-section (a rough approximation, discussed above), this fundamental frequency is related to the spring constant of the probe hair by:

$$f_0 = \frac{C}{2\pi}\sqrt{\frac{k}{0.24m}} \tag{5.4}$$

where f_0 is the fundamental resonant frequency of the probe hair, C is a shape constant which depends on the mode of vibration, and m is the mass of the entire free length of the probe

hair. For these experiments, given that the probe hair is resonating freely and is not being driven by a resonating actuator, the mode of vibration is the first harmonic (or mode 1, with zero nodes) and, therefore, $C = 1$.

The mass of the free length of the fiber is determined by first massing the un-mounted fiber on a Mettler Toledo UMX2 microbalance (± 0.1 μg) and measuring its length with a standard metric ruler (± 0.25 mm). The ratio of mass/length, ρ_l, is assumed constant for the fiber. After mounting the fiber and cutting it to the appropriate length for the measurement (~15 to 30 mm), the free length, l_{free}, is measured and the free mass is assumed to be $m = \rho_l \cdot l_{\text{free}}$.

To determine the resonant frequency of the probe hair, several high-speed videos (~300 frames per second) of individual adhesive jumps out are recorded and the inter-hair distances are measured for each according to the procedure detailed in Section 5.3.2. The continuous wavelet transform of $D(t)$, giving its temporally-localized frequency response, is then computed using MATLAB's built-in Wavelet Toolbox. The fundamental frequency of the probe fiber is computed as the frequency component of the wavelet transform with the highest power, or amplitude, in the temporal vicinity of the adhesive jump out (Figure 5.3) associated with the 'ring-down' frequency of the underdamped spring system. When computed for several videos, we find this frequency determination to be highly reproducible.

Table 5.1 lists the spring constants for the hairs presented in this study and demonstrates, where applicable, that the 'reference spring' and 'resonant frequency' methods are in good agreement.

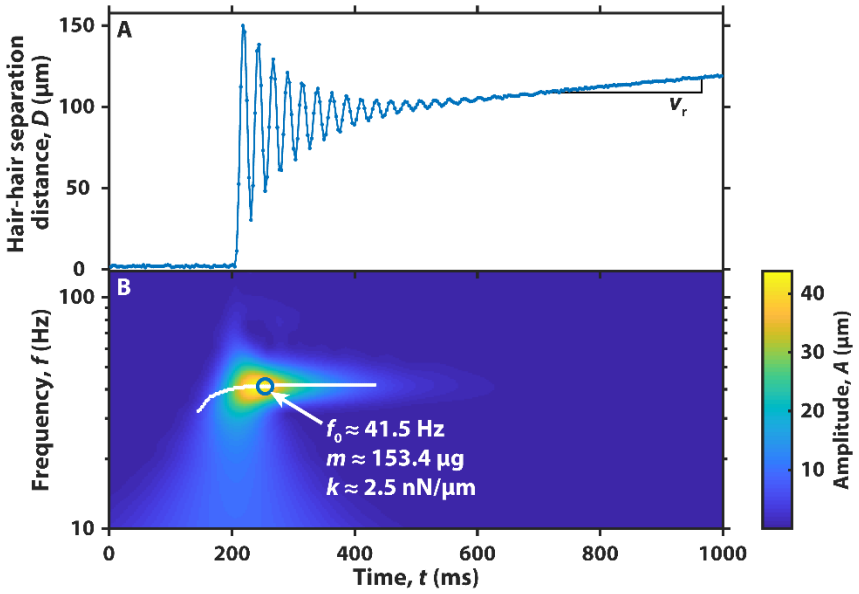

Figure 5.3 – Resonant frequency calibration method. A) Hair-hair separation distance, D, as a function of time, t, for an adhesive jump out of the probe hair segment of 'Treated Hair 1'. The characteristic 'ring-down' of the under-damped system is clearly visible between 200 and 600 ms. B) Frequency spectra of $D(t)$ computed using a continuous wavelet transform. The fundamental frequency, f_0, is indicated by the open circle and is determined by averaging points along the white peak amplitude trace near where it levels off. The free mass of the probe hair segment, m, and the calculated spring constant, k, for this measurement are also indicated.

Table 5.1 – Probe hair spring constants obtained via resonant frequency and reference spring methods (where applicable). Intervals on each k and f_0, v_a, and $v_{a,c}$ are 95% confidence bounds; intervals on l, ρ_l, and m are instrument resolution.

	Resonant frequency method					*Reference spring method* (k_{ref} = 51.5 ± 3.7 nN/μm)		
Hair specimen	l ± 0.2 (mm)	ρ_l ± 0.05 (μg/mm)	m ± 0.1 (μg)	f_0 (Hz)	***k*** **(nN/μm)**	v_a (μm/s)	$v_{a,c}$ (μm/s)	***k*** **(nN/μm)**
Clean Hair 1	22.0	7.38	162.4	71.5 ± 3.1	**7.3 ± 0.7**	–	–	–
Clean Hair 2	17.5	6.64	116.2	56.4 ± 1.0	**3.51 ± 0.13**	30.8 ± 0.3	2.03 ± 0.02	**3.6 ± 0.3**
Clean Hair 3	21.0	9.63	202.2	48.1 ± 0.1	**4.44 ± 0.02**	–	–	–
Clean Hair 4	18.0	5.66	101.9	52.6 ± 0.2	**2.67 ± 0.02**	–	–	–
Clean Hair 5	21.0	7.13	149.8	49.6 ± 0.2	**3.50 ± 0.02**	29.7 ± 0.2	1.98 ± 0.03	**3.7 ± 0.3**
Clean Hair 6	24.0	5.18	124.2	33.4 ± 1.0	**1.31 ± 0.02**	–	–	–
Clean Hair 7	19.5	10.16	198.2	75.5 ± 0.6	**10.7 ± 0.2**	–	–	–
Clean Hair 8	20.5	4.72	96.7	37.0 ± 1.0	**1.25 ± 0.02**	–	–	–
Treated Hair 1	21.2	7.24	153.4	41.3 ± 0.5	**2.48 ± 0.02**	32 ± 0.1	1.54 ± 0.02	**2.6 ± 0.2**
Treated Hair 2	23.5	7.42	174.3	36.2 ± 0.1	**2.16 ± 0.06**	31.7 ± 0.1	1.34 ± 0.03	**2.3 ± 0.2**

5.3.4 Control of experimental parameters

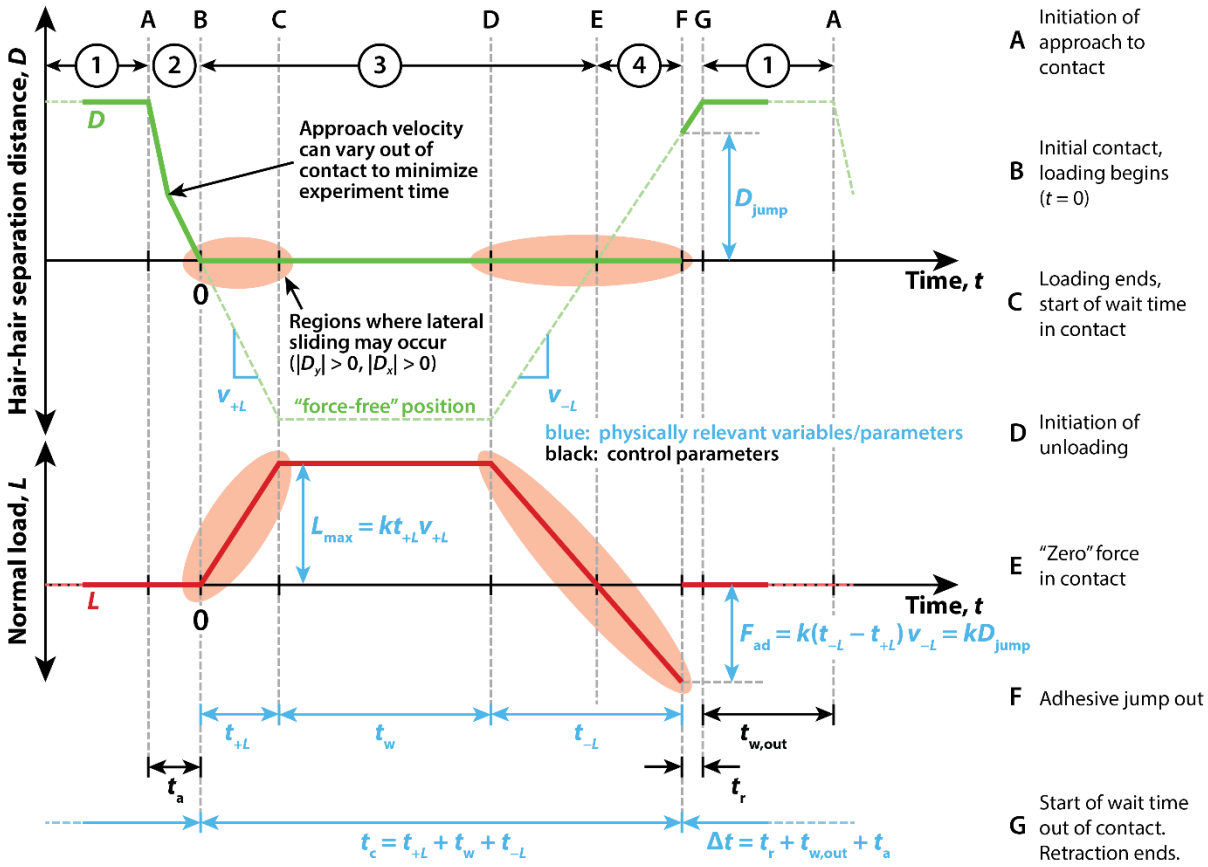

Figure 5.4 – Schematic representation of hair-hair distance, D, and normal load, L, as a function of time, t, for a typical adhesion force measurement. The numbered time intervals correspond to the same numbered illustrations in Figure 5.1. The lettered time points depicted as gray dashed vertical lines correspond to the specific events indicated in the right column of labels. Parameters and variables are labeled as follows: approach/loading velocity, v_{+L}; retraction/unloading velocity, v_{-L}; approach time, t_a; loading time, t_{+L}; waiting time in contact, t_w; unloading time, t_{-L}; retraction time, t_r; waiting time out of contact, $t_{w,out}$; total time in contact, $t_c = t_{+L} + t_w + t_{-L}$; total time between experiments, $\Delta t = t_r + t_{w,out} + t_a$; maximal load, $L_{max} = kt_{+L}v_{+L}$; adhesive jump-out distance, D_{jump}; force of adhesion, $F_{ad} = k\cdot(t_{-L} - t_{+L}) = kD_{jump}$.

For a given adhesion force measurement, several physical parameters may be important, including: the approach/loading velocity, v_{+L}, the retraction/unloading velocity, v_{-L}, the total time in contact, t_c, the maximal load, $L_{max} = kv_{+L}t_{+L}$, and the time between the jump-out of the last adhesion experiment at the same location and the initial contact time of the current adhesion experiment, Δt. These parameters (except for t_c) are controlled using a pair of Faulhaber MCDC3006 micro motion controllers. Figure 5.4 summarizes the relevant

controllable parameters and measurable variables associated with the normal motion, loading, unloading, and adhesive jumps out of the probe fiber.

5.3.5 Local adhesion force measurements

To measure the adhesion force between two hair fibers at a given contact location, the fibers are first brought into contact at some loading velocity, v_{+L}. They are then loaded for an amount of time, t_{+L}, such that the compressive force between the surfaces reaches some maximum load, $L_{max} = kv_{+L}t_{+L}$. After this time, the fibers are kept in contact, without loading or unloading, for an additional amount of waiting time, t_w. The hairs are then separated at some unloading velocity, v_{-L}, until they finally jump apart. The total time in contact, t_c, is calculated as the amount of time between the first instant of contact between the fibers and the time of jump out. The fibers are separated after the jump at v_{-L} for an additional retraction time, t_r, and then held out of contact for an out-of-contact wait time, $t_{w,out}$, after which another adhesion force measurement can take place.

The values for the parameters used in the experiments presented in this work, which were kept constant for all measurements, are given in Table 5.2. Though not explored here, these parameters can be systematically varied to determine the dependence of the adhesion force on time and velocity, allowing us to consider relaxation processes, for example.

Table 5.2 – Motion parameters used for adhesion force experiments.

v_{+L} (μm/s)	v_{-L} (μm/s)	L_{max} (nN)	t_w (s)	t_r (s)	$t_{w,out}$ (s)	$\delta_{y,max}$ (μm)
30 ± 2	30 ± 2	500 ± 20	3 ± 0.1	3 ± 0.1	3 ± 0.1	500

5.3.6 Spatially resolved adhesion force measurements

Due to the characteristic spatial variations in the microscopic surface structure of human hairs, caused by the semi-periodic cuticle scale geometry, there is a broad distribution

in the local shape of contact points at which an adhesion measurement could take place. The adhesion between any two surfaces is also known to intimately depend on the interacting geometry. Therefore, to sufficiently sample all possible contact geometries, and therefore all possible measurable adhesion values, between a pair of hair fibers, it is important to systematically vary the relative positions of the interacting hair fibers. Given a large enough variance in the geometry, the number of measurements necessary to fully-sample this distribution could be (and perhaps always is) too large to sample manually.

Therefore, for the purposes of this study, we have developed a routine to automatically perform individual adhesion experiments, according to input parameters specifying v_{+L}, v_{-L}, L_{max}, t_w, t_r, and $t_{w,out}$ while simultaneously repositioning the fibers between experiments. We define here δ_y as the overall displacement of the top (fixed) hair relative to its starting position for a series of adhesion force measurements. The algorithm for repositioning the fixed hair takes as an input half the length of the fixed hair to be sampled, $\delta_{y,max}$. Starting at the initial contact location of the first adhesion measurement in a series ($\delta_y = 0$, $D_y = D_y(t_{contact})$), the algorithm randomly chooses the direction and distance to move the fixed hair along its axis according to a random walk with a variable step size. The step distance is selected from a uniform distribution between 0 and $½\delta_{y,max}$. If the step would take the random walk outside of the range $\pm\delta_{y,max}$, it is reflected back into the allowed range by the remainder of the step which exceeds the maximum interval. This repositioning algorithm is repeated between each adhesion force measurement. For a given adhesive jump, the position of the probe hair along the fixed hair's axis upon separation relative to the probe hair's initial contact location on the fixed hair for the first

adhesion force measurement is therefore the sum of each fibers' relative displacement, $\delta_y + \Delta D_y$, where $\Delta D_y = D_y(t_{jump}) - D_y(t_{contact})$.

This method of repositioning the hairs was chosen because as the number of experiments, *N*, goes to infinity, a random walk with variable step size has a uniform distribution within a given interval (as opposed to the Gaussian or truncated-Gaussian distribution of a random walk with a uniform step size) but also maintains a small and predictable time between individual experiments when considering that repositioning the hairs is not instantaneous in practice. The random step size also insures that there is no unintended correlation between the chosen step size and the average feature size of the hair surface. The random position selection can only automatically reposition the *fixed* hair in the presented assay, however. Repositioning both hairs is more likely to fully sample the distribution of contact geometries (discussed further in Section 5.4.3).

5.3.7 Measuring surface topography with laser profilometry

To estimate the effect of the hairs' surface topography on the measured adhesion force, an Olympus LEXT OLS4000 laser confocal microscope was used to obtain surface height profiles of extended regions of the hairs' surfaces containing the same regions that were contacted during the adhesion force measurements. The microscope uses laser interferometry to measure surface height with approximately 0.5 to 2 nm vertical resolution and 125 nm lateral resolution.

Each 1024x1024 pixel image from the microscope, at 100x magnification (0.95 NA), is a square measuring 128 μm on a side. The microscope uses an imaging wavelength of

405 nm to obtain *z*-stacks of interferograms, containing 300 to 700 images each, with a pitch of 60 nm. These *z*-stacks are used to compute a single height map at each lateral position. The microscope was programmed to acquire a series of partially overlapping height maps which, in total, cover multiple millimeters along the hairs' axes (2.6 mm for the top hairs and 0.55 mm for the bottom hairs). Using automatic feature detection, matching, and registration, and affine image transformations contained in the MATLAB Image Processing Toolbox, the acquired set of height maps was stitched together into a continuous height profile with vertical and lateral resolution equal to that of the individual images. These stitched images were further processed using an anisotropic median filter to reduce pixel spot noise and sharp features, thereby eliminating erroneously-large curvatures from the topographical maps.

5.3.8 A simple adhesion force model based on hair surface topography

Using the surface profile data acquired from laser profilometry for each pair of hairs as a function of lateral position, we define the height, *z*, at any lateral position, *x* and *y* as $z = S(x,y)$. Therefore, the local mean curvature, *H*, of each height profile is calculated using the relationship:

$$
\begin{aligned}
2H &= -\nabla \cdot \left(\frac{\nabla(z - S)}{|\nabla(z - S)|} \right) \\
&= \nabla \cdot \left(\frac{\nabla S - \nabla z}{\sqrt{1 + |\nabla S|^2}} \right) \\
&= \frac{\left(1 + \left(\frac{\partial S}{\partial x}\right)^2\right)\frac{\partial^2 S}{\partial y^2} - 2\frac{\partial S}{\partial x}\frac{\partial S}{\partial y}\frac{\partial S^2}{\partial x \partial y} + \left(1 + \left(\frac{\partial S}{\partial y}\right)^2\right)\frac{\partial^2 S}{\partial x^2}}{\left(1 + \left(\frac{\partial S}{\partial x}\right) + \left(\frac{\partial S}{\partial y}\right)\right)^{3/2}}
\end{aligned}
\tag{5.5}
$$

Figure 5.5 shows the surface profile of a hair segment, colored with the local mean curvature. Positive curvature (yellow) indicates convex curvature relative to the surface normal, and

negative curvature indicates concave curvature relative to the surface normal. The mean curvature of the difference in height, *d*, between two super-imposed sections of each hair is calculated in a similar fashion and is depicted in Figure 5.6. The curvature of this difference surface at its minimum point, d_{min}, for a given pair of superimposed sections of hair is taken as $H_{eff} = 1/R_{eff}$ for the contact between the hairs at that point. This effective radius corresponds to the radius of a 'sphere-on-flat' contact which would exhibit equivalent adhesion force (given the same conditions of temperature, pressure, humidity, separation velocity, etc.). A first approximation, the adhesion force is therefore given by:

$$F_{ad} = -4\pi R_{eff}\gamma \tag{5.6}$$

where F_{ad} is the force of adhesion between the two surfaces at a given contact point (negative forces are adhesive, positive forces are repulsive), and γ is the average surface energy of the hair, which has been measured previously using a fiber tensiometer [8, 27]. For the purposes of this model, we will assume $\gamma = 26$ mJ/m^2, as measured for clean hair [8, 27]. The treatment used for the treated hairs in this study is not known to dramatically change the surface energy, and therefore $\gamma = 26$ mJ/m^2 is used for these experiments as well. Models of other treatments may require a different surface energy to best fit the measured adhesion force data.

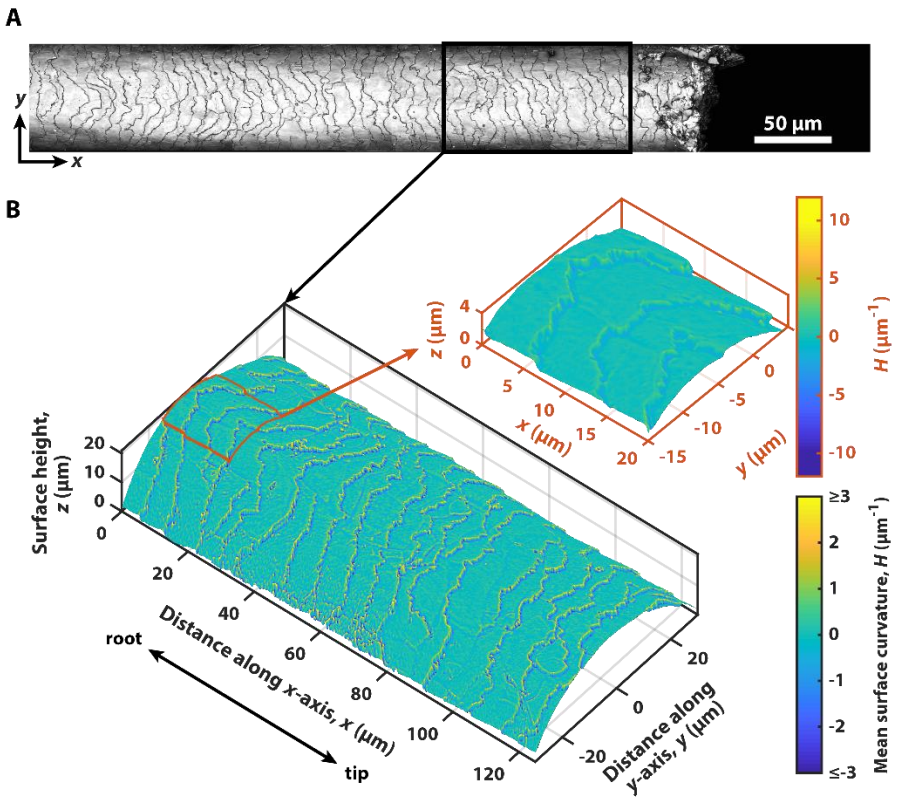

Figure 5.5 – Hair surface topography from laser confocal microscopy. A) Optical micrograph from laser confocal microscope depicting ~400 µm near the tip of the probe hair segment of Clean Hair 8. B) The larger plot shows the ~125 µm long surface height map from the boxed region of the image in panel A) with the coloration corresponding to the local mean curvature at each point. The color scale in the larger image is saturated at both positive and negative curvature to give higher contrast to the surface features. The zoomed orange inset corresponds to the outlined region on the larger plot and has a full color scale with no saturation.

Using this simplified model, the spatial and overall distribution of randomly sampled adhesion forces has been calculated for selected sub-regions of the imaged hair surfaces by calculating F_{ad} for each possible relative lateral position. The dimensions of the sub sections used to calculate each modeled adhesion force distribution correspond to the real physical dimensions of the adhesion force measurements. For example, if the fixed hair was automatically translated within a 1 mm sampling range during the adhesion force measurements, and the probe hair was observed to translate 15 µm along its axis due to its own natural bending, then the simulated adhesion distributions would be calculated by

comparing each permutation of the two hair images within 1 mm on the top hair and 15 μm on the bottom hair.

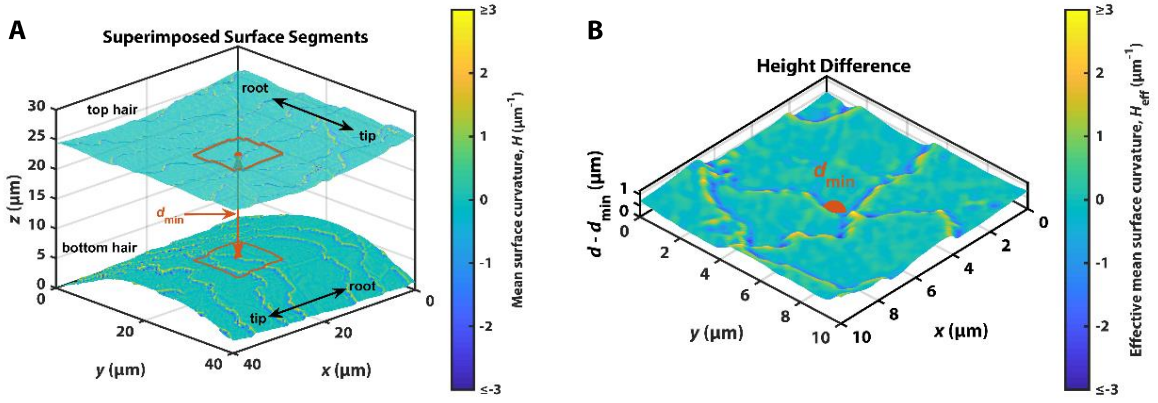

Figure 5.6 – Schematic demonstration of calculating R_{eff} using differential geometry. A) Two surface height maps, colored by their local mean curvature, H, from sections of two separate hairs superimposed with their root-to-tip axes oriented at 90°. The external surfaces of the hairs are facing each other, therefore the 'top hair' height data has been rotated 180° about the y-axis after acquisition. The point of closes approach, d_{min}, is indicated with an orange circle on each hair and an orange double arrow. The difference in height, d, within the orange, outlined regions on each surface is shown in B). B) Surface plot of the difference in height between the top and bottom hair, colored by local mean curvature of this difference surface, H_{eff}, within a region near the point of closest approach, d_{min}. $H_{eff}(d_{min})$ is assumed to be the effective 'sphere-on-flat' curvature at the point of closest approach, used to model the force of adhesion between the hairs at that point. The model computes this curvature for thousands of different relative positions of the top and bottom hairs.

5.4 Results and Discussion

5.4.1 Reproducibility of local adhesion force measurements

By following the protocol detailed in Section 5.3.5, the adhesion force between two hair fibers has been repeatedly measured within the same approximate contact region (±2 to 5 μm) along each fiber's axis. From these localized experiments, the measured adhesion force may either be highly reproducible and approximately single-valued, or exhibit several distinct, reproducible modes. This is best demonstrated in Figure 5.7 which shows six replicate adhesion force measurements, acquired during HAFA development and testing, whose jump distances (and therefore adhesion forces) modulate between two distinct values.

Each of the two jump distances is highly reproducible, shown in Figure 5.7A, and correspond to specific lateral positions, D_y, along the fixed hair (Figure 5.7B).

To explain the observed multi-modal behavior in adhesion force, we note that, due to non-idealities in the probe hair's shape – including variations in diameter, ellipticity, twist angle, internal composition, cuticle thickness, and cuticle density – it is challenging, if not impossible, to determine a single major bending mode for a given fiber. Therefore, upon application of increased compressive force (L) between the hair fibers after contact, the position of the probe hair along the axis of the fixed hair (D_y) relative to its initial contact position may change. This allows the probe hair to sample different areas of the fixed hair during loading and unloading. We believe, therefore, that the differences in the modes of adhesion force correspond to the different geometries of different local minima in the overlapping hairs' surface structures in which the probe hair may get trapped within its sliding path during unloading. These different local geometries have different effective radii of contact, R_{eff}, assuming a single-asperity model, and, given the cuticle structure of hair fibers, can result in orders of magnitude variations in adhesion force, F_{ad}, for a single pair of fibers (even if the surface energy of the hair, γ, is assumed to be spatially invariant).

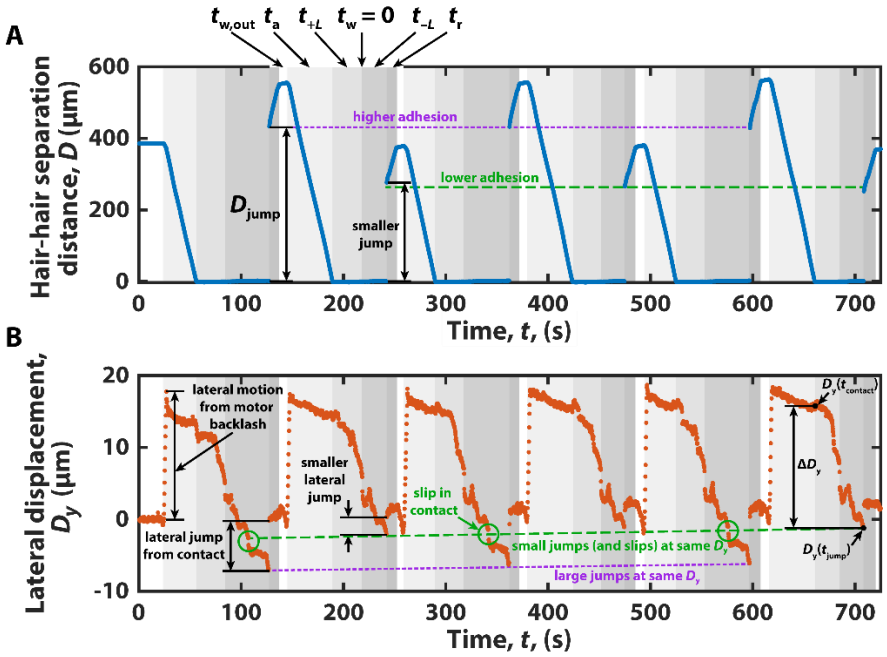

Figure 5.7 – Characteristic D and D_y traces during a series of adhesion force measurements. A) Hair separation distance, D, plotted as a function of time, t. The particular automation segments, labeled with their respective time intervals, are indicated in various shades of gray. There are two distinct modes of D_{jump} (and therefore adhesion force) present during this experiment, labeled with black double arrows and classified by the purple and green dashed lines. B) The lateral displacement of the probe hair segment, D_y, plotted as a function of time, t, for the same trace in A). Lateral jumps of the probe hair upon jump out are labeled with black arrows. The lateral location corresponding to the two different modes in D_{jump} are reproducible and also indicated with purple and green dashed lines. Lateral slips in the D_y traces during the higher-adhesion cycles are circled in green and align with the lateral jumps of the lower-adhesion cycles.

When sampling small enough areas of hair, like in the case where the relative hair positions are not intentionally varied between measurements, the effect of surface topography will result in few distinct modes in the adhesion force histogram associated with the small set of local adhesive minima available to the probe hair in that area.

5.4.2 Effect of contact location on adhesion force

Given the multi-modal nature of the adhesion force between the hair fibers and the assumption that these modes arise from heterogeneities in the surface structure (and chemistry) of both the probe and fixed hairs, in order to fully characterize the adhesion force between two fibers, it is necessary to randomly sample, with thousands of individual measurements, the local adhesion force over large lengths of hair (> 500 μm). This is

accomplished by repositioning the top fiber along its cylindrical axis between individual measurements (discussed further in Section 5.3.6). Because of the loosely-correlated nature of the cuticle edge separation distance along the axes of hair fibers, the new position of the fiber after a given adhesion force measurement is chosen using a random walk with variable step size. This choice limits the potential for over-sampling the same type of location, be it cuticle edge or cuticle flat, along the hair fiber, which could be common if a uniform step size was chosen which correlates well with the average inter-cuticle distance.

This series of adhesion measurements for a given pair of hairs, in combination with simultaneous tracking of the relative positions of the probe and fixed fibers, allows us to develop overall (Figure 5.8) and spatially-resolved (Figure 5.9) adhesion force histograms which fully characterize the expected probability distribution of adhesion forces within the length of hair measured. The overall distributions in Figure 5.8, though somewhat varied in their shape, are all within the same range of forces (0 to ~1500 nN) and have similar breadths. It is also universal, regardless of the overall shape, for each distribution to have at least one mode in the 100 to 200 nN range, with additional modes, like those seen in Clean Hairs 6 and 7, potentially extending above 500 nN.

We observe a mostly uniform adhesion force distribution with space, however, there are regions in which a particular mode of adhesion force may dominate. This spatial modality is most easily observed for Clean Hair 7 (Figure 5.9A). The lower and higher modes in the overall adhesion distribution are localized in space between -400 and -200 μm and between 100 and 400 μm, respectively. Other more subtle spatial variations are observed in the distributions in Figure 5.9B-C. Though not depicted here, changing the contact region on the probe hair by manually translating it along its axis between a series of experiments causes

subtle changes in the overall adhesion distribution. Because of this effect, we believe that future implementations of the HAFA should include the ability to automatically translate the probe hair as well. The adhesion force model presented in Sections 5.3.8 and 5.4.3 further corroborates this conclusion.

This rich information allows for confident course-graining of the adhesion distribution and can be applied in models of full heads of hair [15] by selecting a random sample of adhesion forces from the measured distribution for each simulated hair-hair contact.

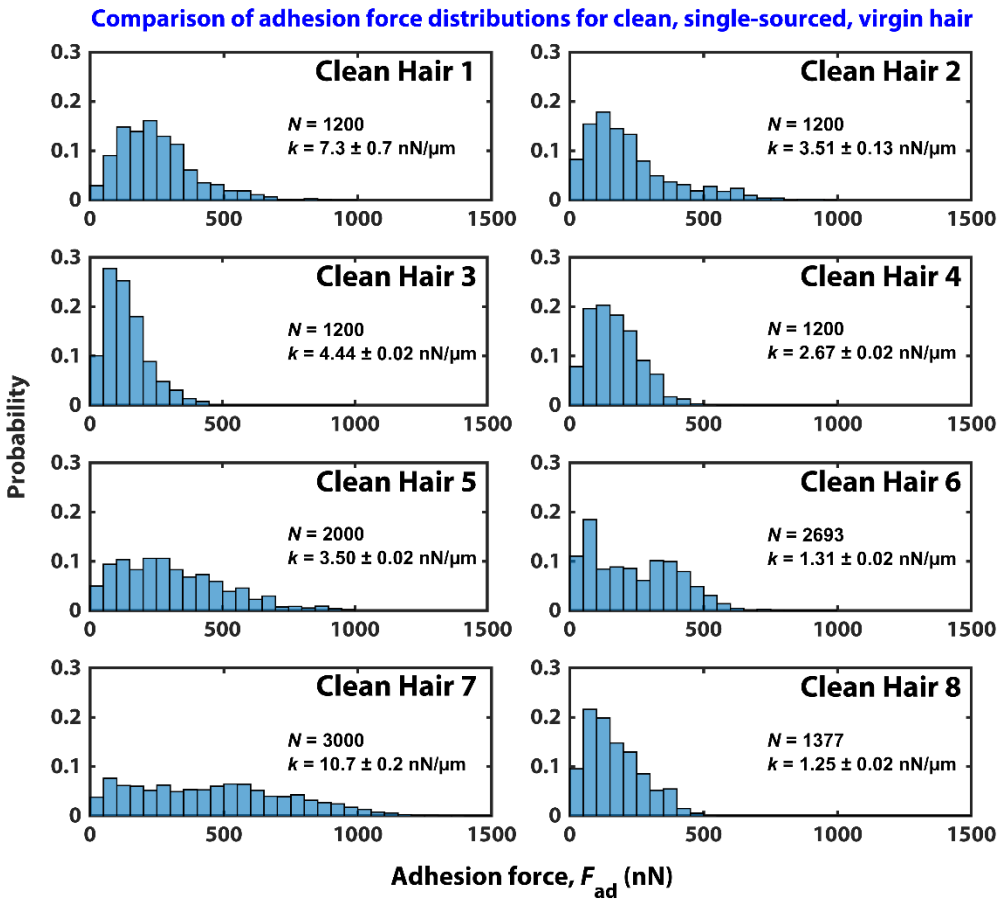

Figure 5.8 – Overall adhesion force histograms for eight pairs of clean, single-sourced, virgin hairs. All experiments were conducted at ~62% relative humidity and ~24 °C with motion parameters given in Table 5.2.

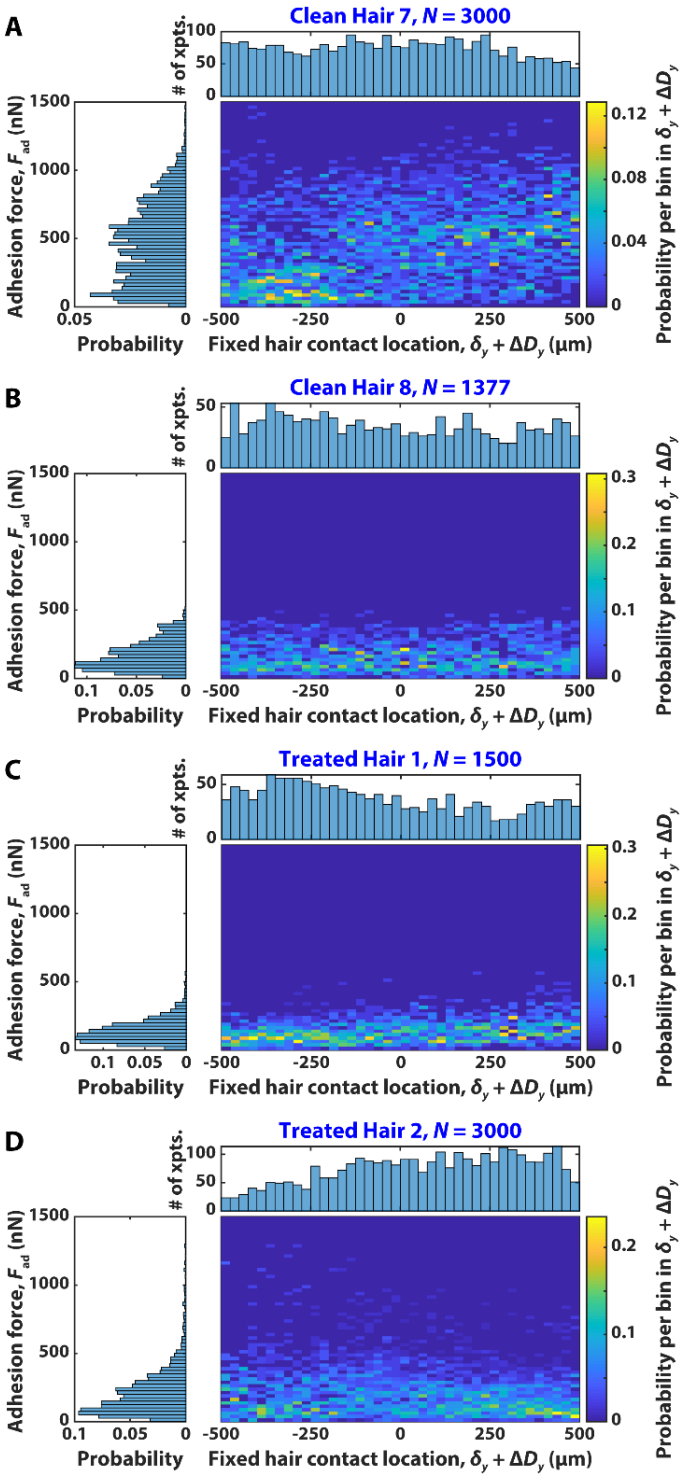

Figure 5.9 – Spatially resolved adhesion force distributions for A,B) clean and C,D) treated hair specimens. The 2D histogram plots the probability of measuring a particular adhesion force (vertical bins) within a range of locations along the fixed hairs length (horizontal bins). The top bar chart of each panel shows how many individual ahdesion measurements were conducted within a particular horizontal bin. The left, rotated, 1D histogram in each panel shows the overall probability, avarged along the fixed hairs length, of measuring a particular adhesion force for the given pair of hairs.

5.4.3 Comparing measured and modeled adhesion force distributions

The surface topography of the HAFA contact regions of each of the four pairs of hair segments presented in Figure 5.9 has been measured *ex situ* according to the procedure detailed in Section 5.3.7. With this topographical information, the adhesion force between the probe and fixed fiber segments has also been modeled according to the procedure in Section 5.3.8. The resulting overall adhesion force histograms calculated by superimposing the *full* image range of the model are presented in orange in the top plots Panels A-D in Figure 5.10. The full image range from the topographical data over-represents the length-scales measured in the HAFA, but already begins to reproduce the main features of the empirical adhesion force distributions. For example, the overall range in forces, from approximately 1 to 1000 nN is well represented in the model. The tails the full-image model distributions extend to very high forces and are effectively asymptotic. This asymptotic behavior is impossible to fully reproduce in the physical experiments with such small *N*, but the measurements do suggest an extended, high-adhesion force tail would be observed. The model histograms also have major peaks around 100 to 200 nm in all cases, which is in good agreement with the measured distributions. And have similar spatial variations in adhesion force, as demonstrated in the righthand panels of Figure 5.21-Figure 5.24.

Finally, the model distribution for ‘Clean Hair 7’ in Figure 5.10A reproduces a large shoulder, extending to > 350 nN. We believe this shoulder, observed in both the measured adhesion force distribution and the model distribution, is due to the fact that the cross section of Clean Hair 7 was in fact more bean-shaped than elliptical. This is most readily noticeable from the horizontal hair image in Figure 5.13 in Appendix B, Section 5.8. Along the entire length of the top hair, there is a macroscopically concave feature, not only giving the hair low

curvature within that feature, but also causing there to be two separate convex curvature regions for any given position along the hair's axis. This complex morphology might be characteristic in a given individual's head of hair, and we believe that instead of avoiding non-ideal geometries due to their difficulty to measure, it is best to characterize all possible manifestations of the hair system. Both the HAFA technique and the adhesion model can capture these complexities equally well.

To even better represent the measured histograms using the surface topography model, the model distributions have been sub-sectioned into relevant lengths scales of each hair fiber (1000 μm along the top hair and 10-35 μm on the bottom hair). When subdividing the "full image range" distributions into smaller sections, we can compute for each subsection's overall histogram a statistical parameter, "Y^2" [28], which captures the goodness of fit between two randomly-sampled, binned distributions (the model and HAFA adhesion force distributions in this case). The statistical parameter is a modified version of Karl Pearson's χ^2 parameter for determining goodness of fit between categorical distributions, which has been adapted to better represent comparisons between histograms which have some bins with counts ≤ 10. For a two-sample test [29] of multinomial distributions (like the data we have generated with the HAFA and the model), the parameter takes the form:

$$Y^2 = \nu + \sqrt{\frac{2\nu}{2\nu + \left[\frac{(R+S)^2}{RS} - 6\right]\sum_{i=1}^{N_B}\frac{1}{R_i+S_i}}} \cdot \left(\sum_{i=1}^{N_B} \frac{\left(\sqrt{\frac{S}{R}}R_i - \sqrt{\frac{R}{S}}S_i\right)^2}{R_i+S_i} - \nu \right) \tag{5.7}$$

where N_B is the total number of bins containing > 0 counts for both distributions, R_i and S_i are the histogram counts in the ith bin for each distribution, and ν is the number of degrees of

freedom, which is equal to $N_B - 1$ for this system having no fitting parameters. Finally R and S are the total number of counts in each distribution:

$$R = \sum_{i=1}^{N_B} R_i \qquad S = \sum_{i=1}^{N_B} S_i \tag{5.8}$$

Computing the Y^2 parameter also allows for the calculation of a p-value between the two distributions to determine whether they are significantly different. However, given the size of the distributions (R > 1000 for the measured distributions and S > 400,000 for the model distributions), the p-value always reports that the distributions are different. Nevertheless, we can still use the calculated Y^2 for each physically relevant spatial sub-section of the model distribution to find the "best-fit" sub-section where the model and measured data agree most strongly. This "best-fit" sub-section will reside where Y^2 is at its minimum. Figure 5.13-Figure 5.16 in Appendix B, Section 5.8 plot the Y^2 parameter as a function of location along the hair images for each of the four hairs studied in this work. The minimum Y^2 parameter is indicated and the overall adhesion force distribution associated with this minimum Y^2 parameter is plotted in the bottom panels of Figure 5.10A-D.

The "best-fit" distributions better represent the shapes of the measured distributions. We believe this is due to the fact that they are sampled from physically-relevant lengths of hair. The most striking resemblance is found again for Clean Hair 7 in the bottom panel of Figure 5.10A. The shoulder from the model distribution almost perfectly matches the second mode in the measured distribution, though the lower forces are still over-represented in the model. The agreement between the "best-fit" modeled and measured distributions, though encouraging, does not imply that we have found, using this model, the true location along the probe and fixed hairs from which the measured distributions have been sampled. We can

conclude, however, that the model verifies the notion that there exists a combination of surface topographies for a given pair of hair segments which can, using no free fitting parameters (the surface energy, γ, of 26 mJ/m^2 is fixed), predict the general shape and magnitude of the measured distributions.

We have also compared the measured adhesion force distributions to the modeled distributions from *different* hair surfaces to study if similar results can be obtained for models which could not have contained the same surface topographies as the lengths of hair studied in the HAFA. The results from these 'cross-comparisons' are shown in Figure 5.10E-H, and Figure 5.17-Figure 5.20 and Figure 5.25-Figure 5.28 in Appendix B, Section 5.8. These plots are all identical to the direct comparisons described above, however the pairing of modeled to measured distributions has been switched (comparing HAFA data from Clean Hair 7 to the surface topography model from Clean Hair 8, for example). The major conclusion from this 'cross-comparison' study is that "best-fit" model distributions tend to sacrifice overall shape for better agreement with the mean of the distribution. After obtaining these cross-comparisons, it is most useful to compare the bottom "best-fit" panels to their direct-comparison counterparts (comparing Figure 5.10A to E, B to F, C to G, and D to H). For all cross-comparisons but the one between measured Clean Hair 7 and modeled Clean Hair 8, it is difficult from inspection to determine whether the direct- or cross-comparison is a better fit for the HAFA data. However, again, the complicated shape of the Clean Hair 7 morphology caused the HAFA adhesion for distribution to only be best represented by the model distribution obtained from the same hairs. Though the "best-fit" model distribution from Clean Hair 8 for the measured distribution from Clean Hair 7 (Figure 5.10E, bottom panel)

has an extended tail, it cannot capture the shape of the higher mode of adhesion from the HAFA measurements.

Because the model and measurements agree well when applied over the same length scales of hair, it is satisfying to assume that if the probe hair, in addition to the fixed hair, were randomly and automatically translated along its axis between individual adhesion force measurements, the measured adhesion force distributions would converge to the "full-image range" model distributions, given enough replicate measurements. However, a few caveats remain in this assumption: i) the surface topography model treats all surface features as infinitely rigid asperities, ii) if the surfaces contact at a very high curvature, localized asperity (like that associated with a contaminant or a highly-raised cuticle edge), the model does not allow for the surfaces to readjust their positions to slide past the asperity, iii) similarly, though each surface is locally planarized with respect to the *x*-*y* plane preceding each R_{eff} calculation, the height maps are not planarized with respect to one another, iv) the surfaces are not allow to translate laterally until they find the closes local minimum in surface curvature for a given R_{eff} calculation. These caveats preclude the model from perfectly representing the measured distributions, and in effect cause the model to over-represent lower radius (lower adhesion force, higher energy) contacts. Future work to account for these limitations would prove useful.

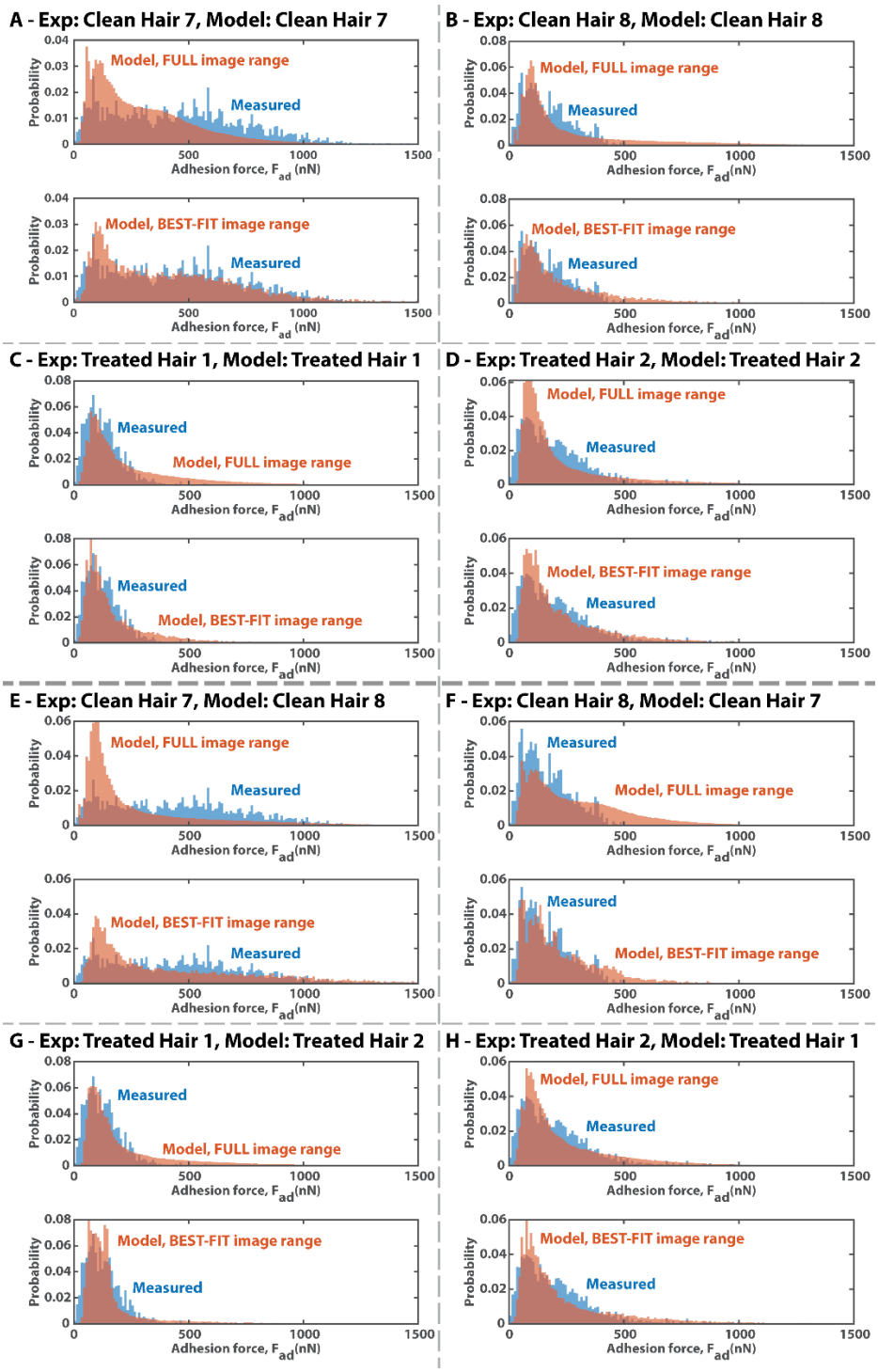

Figure 5.10 – Comparison of experimentally measured adhesion forces using HAFA (Exp:) and modeled adhesion forces using surface topography (Model:) for the four hair samples studied in this work (clean, A,B,E,F; treated C,D,G,H). For each main panel A-H, the top sub-panel shows the model histogram calculated using the full range of acquired profilometry data, while the bottom sub-panel shows the model histogram calculated using the best-fit sub sections of each fixed/probe hair which correspond to the physically-relevant lengths of hair measured during the HAFA experiments. Panels A-D show comparisons where the HAFA and profilometry data come from the same hairs while panels E-F compare experiment/model data from dissimilar hairs to demonstrate the robustness of the model.

5.5 Conclusions

Using a specially-designed modification to an SFA Mark II, dubbed the "hair adhesion force apparatus" we can measure the overall and spatial distributions in adhesion force between individual human hair fibers with ~1 nN force resolution and ~1 μm spatial resolution (in one dimension). The technique is the first example of using the hair fibers themselves to determine the surface forces. This approach is easier to implement than similar AFM-based adhesion force measurements and allows the hairs to bend naturally with the forces that would be present in the native environment within a head of hair. We find that, universally, for the clean and treated samples measured in this study, which do not have significant surface modifications compared to a natural hair surface, there exists at least one mode of adhesion force within 100-300 nN (or corresponding to local curvatures of ~1-2 μm). Additional modes may also be present, depending on the surface geometry of the hair.

Making only a single assumption about the surface energy of the hair fibers, an adhesion force model, which considers the *ex situ*-determined surface topography of the hairs measured in the HAFA, can predict the magnitude, range, and shape of the measured adhesion force distributions. More careful statistical considerations allow for the model to capture subtleties in the distributions with adequate fidelity. The combination of these two techniques gives further insight into just how important the surface features of hair fibers can be in modulating the adhesion within a full head of hair. Perhaps from these experiments, novel hair care products which attempt to control surface morphology using the intentional deposition of micro-scale particles of specific geometries can be developed. Finally, the distributions obtained in this work may provide a foundation for more complex models of

full heads of hair which can coarse-grain these phenomena by sampling from distributions with similar shapes.

5.6 References

1. Chen, N., Bhushan, B.: Morphological, nanomechanical and cellular structural characterization of human hair and conditioner distribution using torsional resonance mode with an atomic force microscope. J. Microsc. 220, 96–112 (2005)

2. Latorre, C., Bhushan, B.: Nanotribological effects of hair care products and environment on human hair using atomic force microscopy. Cit. J. Vac. Sci. Technol. A. 23, 1034 (2005)

3. Gray, J.: Hair care and hair care products. Clin. Dermatol. 19, 227–236 (2001)

4. Bhushan, B.: Biophysics of Human Hair. Springer Berlin Heidelberg, Berlin, Heidelberg (2010)

5. Bhushan, B.: Nanoscale characterization of human hair and hair conditioners. Prog. Mater. Sci. 53, 585–710 (2008)

6. LaTorre, C., Bhushan, B.: Nanotribological characterization of human hair and skin using atomic force microscopy. Ultramicroscopy. 105, 155–175 (2005)

7. Wei, G., Bhushan, B., Torgerson, P.M.: Nanomechanical characterization of human hair using nanoindentation and SEM. Ultramicroscopy. 105, 248–266 (2005)

8. Lodge, R.A., Bhushan, B.: Wetting properties of human hair by means of dynamic contact angle measurement. J. Appl. Polym. Sci. 102, 5255–5265 (2006)

9. Seshadri, I.P., Bhushan, B.: Effect of ethnicity and treatments on in situ tensile response and morphological changes of human hair characterized by atomic force microscopy. Acta Mater. 56, 3585–3597 (2008)

10. Bhushan, B., Chen, N.: AFM studies of environmental effects on nanomechanical properties and cellular structure of human hair. Ultramicroscopy. 106, 755–764 (2006)

11. Seshadri, I.P., Bhushan, B.: In situ tensile deformation characterization of human hair with atomic force microscopy. Acta Mater. 56, 774–781 (2008)

12. Wei, G., Bhushan, B.: Nanotribological and nanomechanical characterization of human hair using a nanoscratch technique. Ultramicroscopy. 106, 742–754 (2006)

13. LaTorre, C., Bhushan, B.: Investigation of scale effects and directionality dependence on friction and adhesion of human hair using AFM and macroscale friction test apparatus. Ultramicroscopy. 106, 720–734 (2006)

14. Bhushan, B., Wei, G., Haddad, P.: Friction and wear studies of human hair and skin. Wear. 259, 1012–1021 (2005)

15. Michels, D.L., Mueller, J.P.T., Sobottka, G.A.: A physically based approach to the accurate simulation of stiff fibers and stiff fiber meshes. Comput. Graph. 53, 136–146 (2015)

16. Max, E., Häfner, W., Wilco Bartels, F., Sugiharto, A., Wood, C., Fery, A.: A novel AFM based method for force measurements between individual hair strands. Ultramicroscopy. 110, 320–324 (2010)

17. Luengo, G.S., Mizuno, H., Rutland, M.W.: Hair-Hair Contact Dynamics and Interactions Studied with Atomic Force Microscopy. Springer International Publishing, Cham (2017)

18. Mizuno, H., Luengo, G.S., Rutland, M.W.: Interactions between crossed hair fibers at the nanoscale. Langmuir. 26, 18909–18915 (2010)

19. Mizuno, H., Luengo, G.S., Rutland, M.W.: New Insight on the Friction of Natural Fibers. Effect of Sliding Angle and Anisotropic Surface Topography. Langmuir. 29, 5857–5862 (2013)

20. Adams, M.J., Briscoe, B.J., Wee, T.K.: The differential friction effect of keratin fibres. J. Phys. D. Appl. Phys. 23, 406–414 (1990)

21. Adams, M.J., O'Keefe, E., Briscoe, B.J., Kremnitzer, S.L.: A study of the friction and adhesion of polyethylene-terephthalate monofilaments in liquid media. J. Phys. D. Appl. Phys. 16, L9–L15 (1983)

22. Briscoe, B.J., Kremnitzer, S.L.: A study of the friction and adhesion of polyethylene-terephthalate monofilaments. J. Phys. D. Appl. Phys. 12, 505–516 (1979)

23. Pascoe, M.W., Tabor, D.: The Friction and Deformation of Polymers. Proc. R. Soc. A Math. Phys. Eng. Sci. 235, 210–224 (1956)

24. Israelachvili, J., Min, Y., Akbulut, M., Alig, A., Carver, G., Greene, W., Kristiansen, K., Meyer, E., Pesika, N., Rosenberg, K., Zeng, H.: Recent advances in the surface forces apparatus (SFA) technique. Reports Prog. Phys. 73, 036601 (2010)

25. Torii, A., Sasaki, M., Hane, K., Okuma, S.: A method for determining the spring constant of cantilevers for atomic force microscopy. Meas. Sci. Technol. 7, 179–184 (1996)

26. Cumpson, P.J., Hedley, J., Zhdan, P.: Accurate force measurement in the atomic force microscope: a microfabricated array of reference springs for easy cantilever calibration. Nanotechnology. 14, 918–924 (2003)

27. Wortmann, F.J., Wortmann, G., Schulze zur Wiesche, E.: Spatial Probing of the

Properties of the Human Hair Surface Using Wilhelmy Force Profiles. Langmuir. 26, 7365–7369 (2010)

28. Lucy, L.B.: Hypothesis testing for meagre data sets. Mon. Not. R. Astron. Soc. 318, 92–100 (2000)

29. Press, W.H., Teukolsky, S.A., Vetterling, W.T., Flannery, B.P.: Numerical recipes in C. Cambridge university press, Cambridge (1982)

5.7 Appendix A: Spring Constant Calibrations

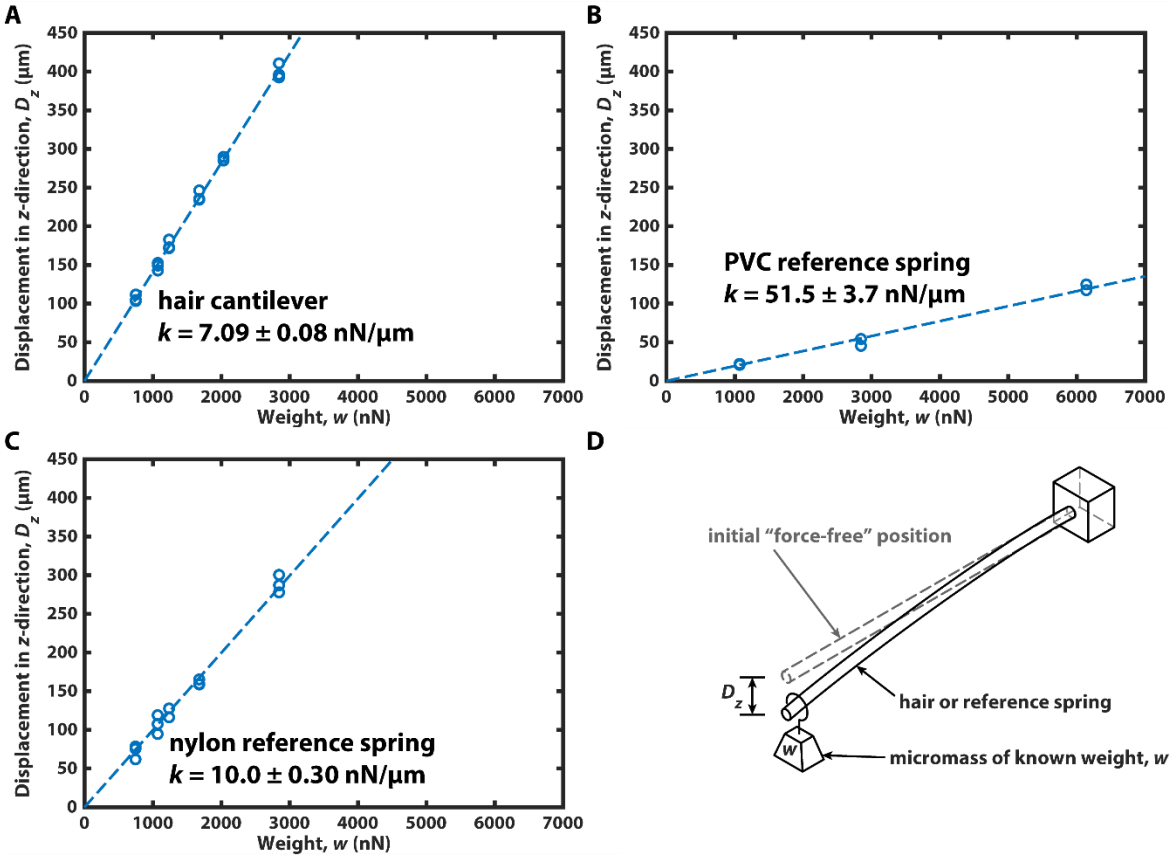

Figure 5.11 – 'Suspended mass' method spring constant calibration curves for A) a hair cantilever used during validation, B) a PVC reference spring, and C) a nylon reference spring. Error ranges are 95% confidence intervals for the dashed best-fit lines. D) A schematic representation of the hanging mass method showing the cantilever before (gray, dashed) and after (black, solid) a hanging weight, w, is positioned at its free end. D_z is the displacement of the tip of the cantilever between the "force-free" position and the position with the hanging mass.

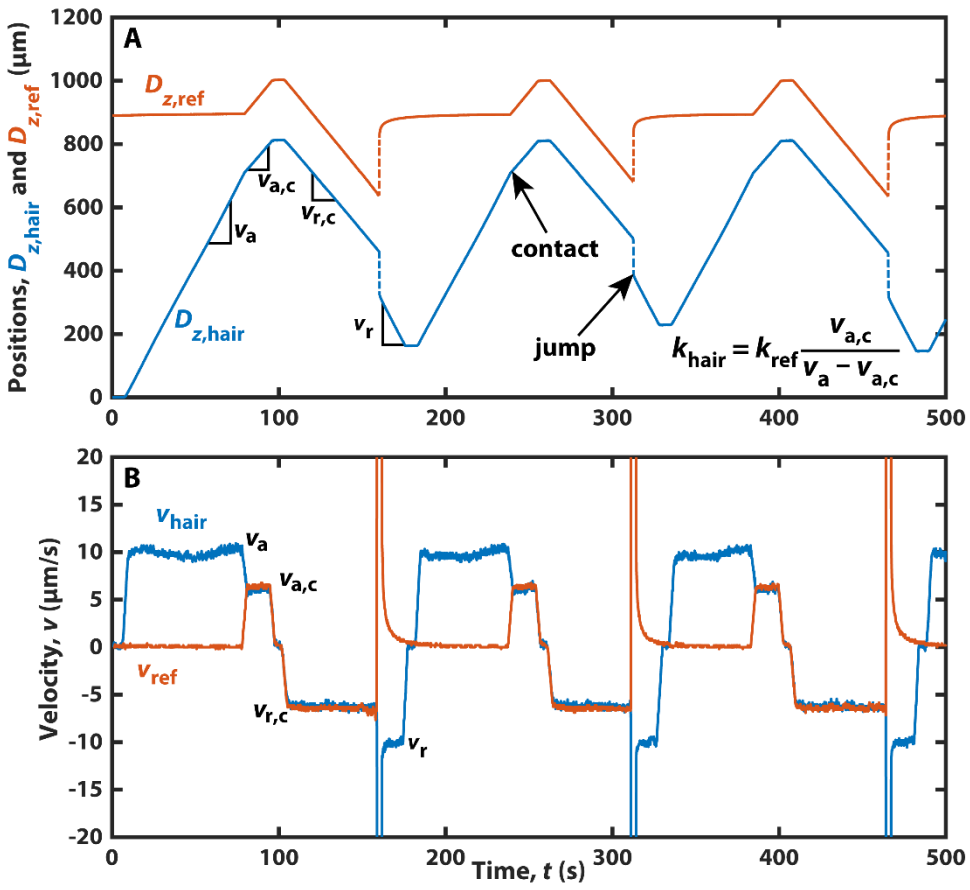

Figure 5.12 – Reference spring calibration method. The position A) and velocity B) traces for both a hair cantilever (blue) and nylon reference spring (orange) used to validate the reference spring constant calibration method. Three separate loading and unloading cycles are shown, from which the hair's spring constant is calibrated. For this experiment, $k_{ref} = 10.0 \pm 0.3$ nN/µm (Figure 5.11C), $v_a \approx 10.0$ µm/s, $v_{a,c} \approx 6.0$ µm/s; therefore, $k_{hair} \approx 15.0 \pm 0.5$ nN/µm.

5.8 Appendix B: Goodness-of-fit maps comparing measured and modeled adhesion force distributions

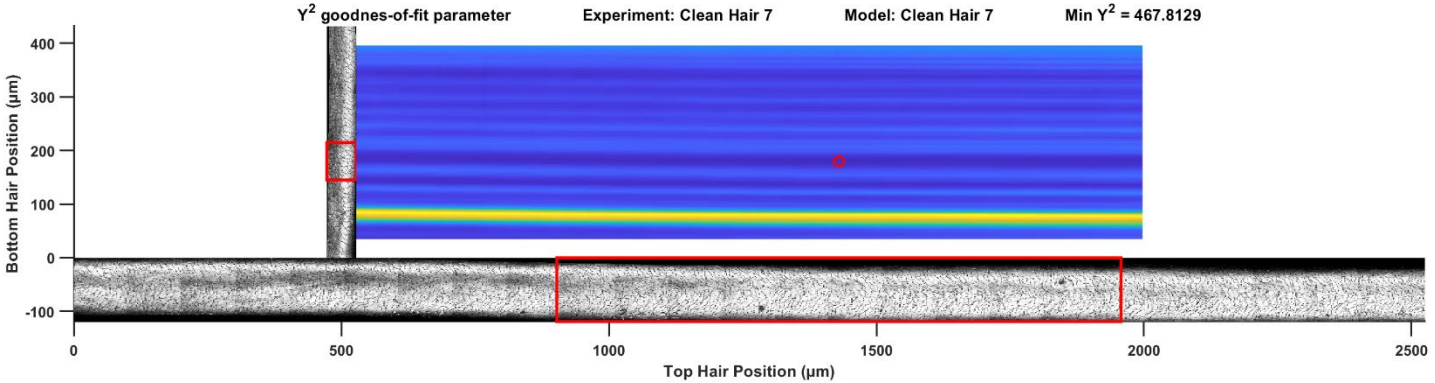

Figure 5.13 – Goodness of fit map between measured adhesion forces from Clean Hair 7 and surface profilometry model from Clean Hair 7. Corresponds to the histograms in Figure 5.10A. Y^2 increases from blue to yellow. Approximately 400 µm of the probe hair (bottom hair) and approximate 2.5 mm of the fixed hair (top hair) are shown and are aligned to scale with the vertical and horizontal axes, respectively. The Y^2 goodness-of-fit parameter is calculated for the overall adhesion force distribution modeled using an overall translation of 1 mm of the top hair and 15 µm of the bottom hair centered at each point in the goodness-of-fit map. The open red circle on the goodness-of-fit map indicates the minimum Y^2 parameter which was calculated from the segments of hair within the red boxes.

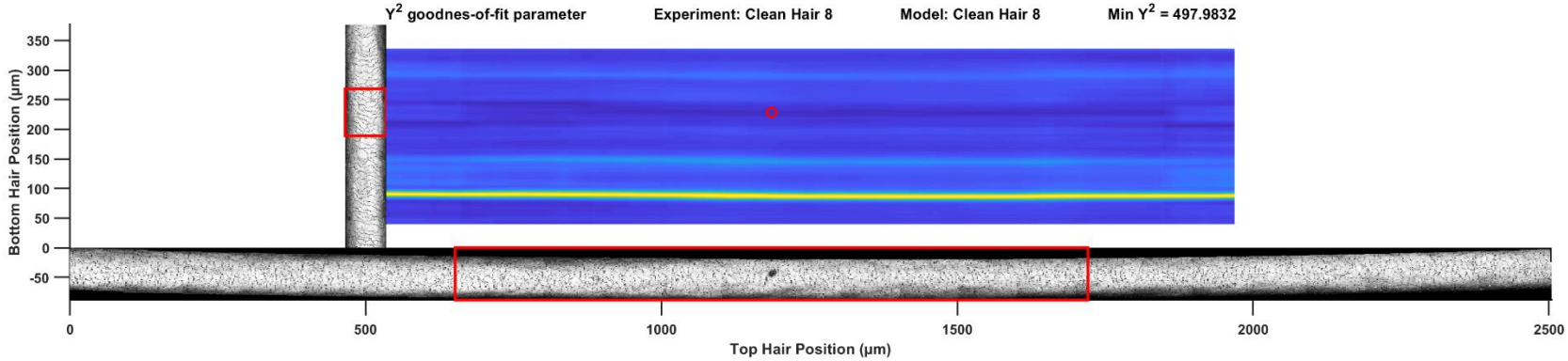

Figure 5.14 – Goodness of fit map as in Figure 5.13 but for measured adhesion forces from Clean Hair 8 and surface profilometry model from Clean Hair 8. Corresponds to the histograms in Figure 5.10B. Translation distance used for the top hair segment in the model was 10 µm.

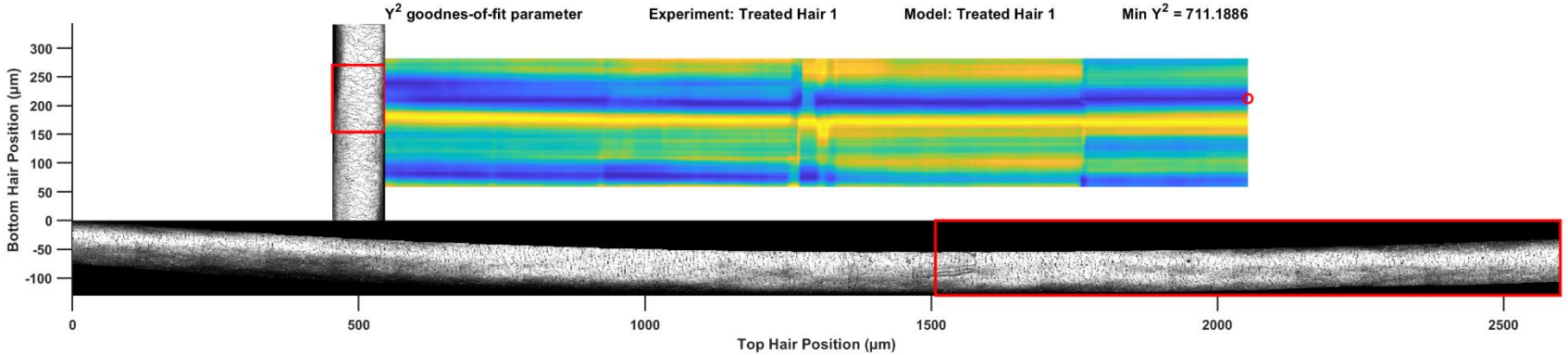

Figure 5.15 – Goodness of fit map as in Figure 5.13 but for measured adhesion forces from Treated Hair 1 and surface profilometry model from Treated Hair 1. Corresponds to the histograms in Figure 5.10C. Translation distance used for the top hair segment in the model was 25 µm.

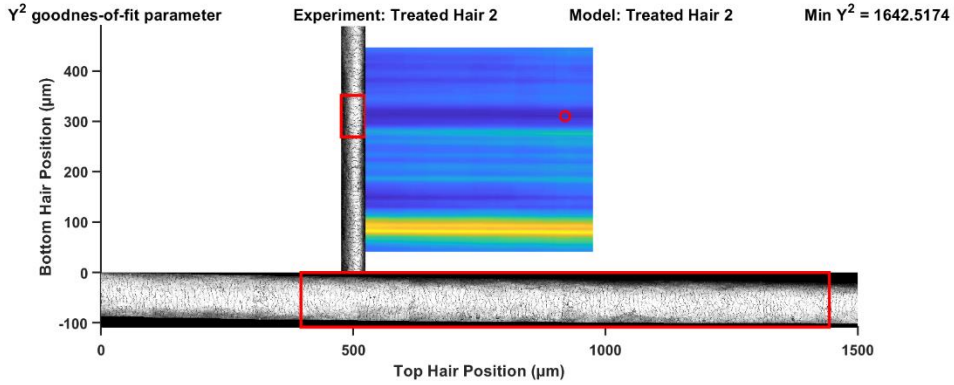

Figure 5.16 – Goodness of fit map as in Figure 5.13 but for measured adhesion forces from Treated Hair 2 and surface profilometry model from Treated Hair 2. Corresponds to the histograms in Figure 5.10D. Translation distance used for the top hair segment in the model was 35 µm.

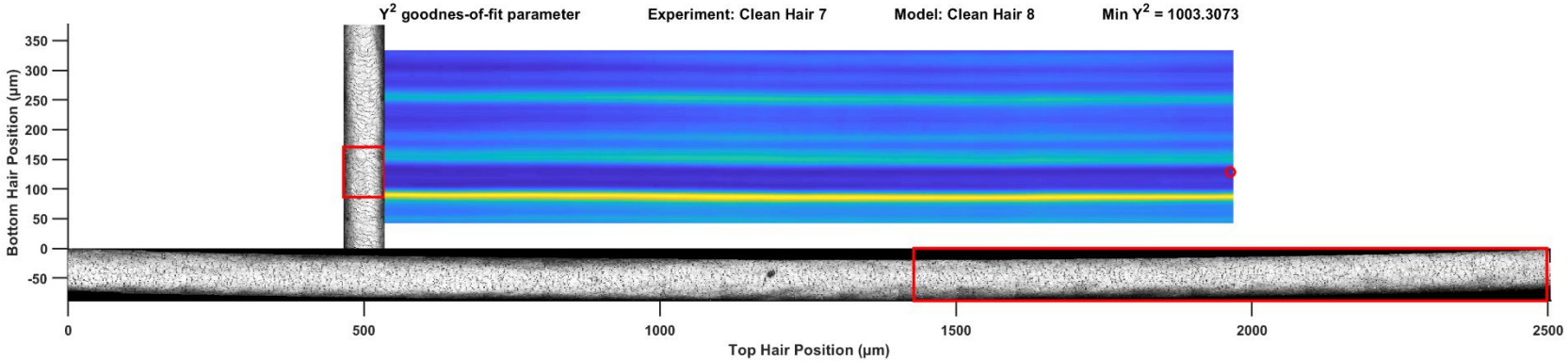

Figure 5.17 – Goodness of fit map as in Figure 5.13 but for measured adhesion forces from Clean Hair 7 and surface profilometry model from Clean Hair 8. Corresponds to the histograms in Figure 5.10E. Translation distance used for the top hair segment in the model was 10 µm.

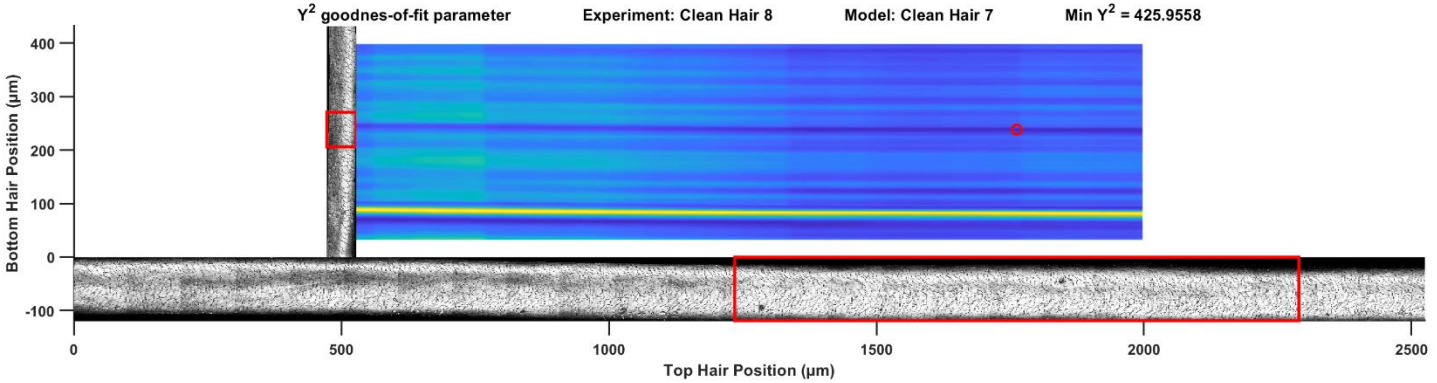

Figure 5.18 – Goodness of fit map as in Figure 5.13 but for measured adhesion forces from Clean Hair 8 and surface profilometry model from Clean Hair 7. Corresponds to the histograms in Figure 5.10F. Translation distance used for the top hair segment in the model was 15 µm.

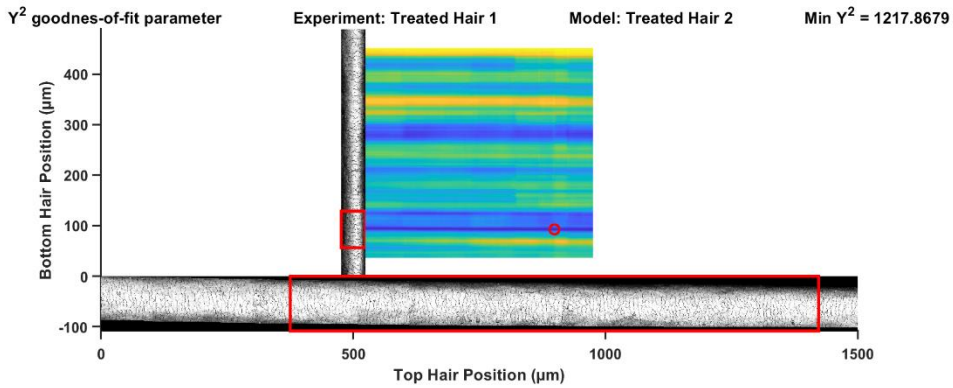

Figure 5.19 – Goodness of fit map as in Figure 5.13 but for measured adhesion forces from Treated Hair 1 and surface profilometry model from Treated Hair 2. Corresponds to the histograms in Figure 5.10G. Translation distance used for the top hair segment in the model was 35 µm.

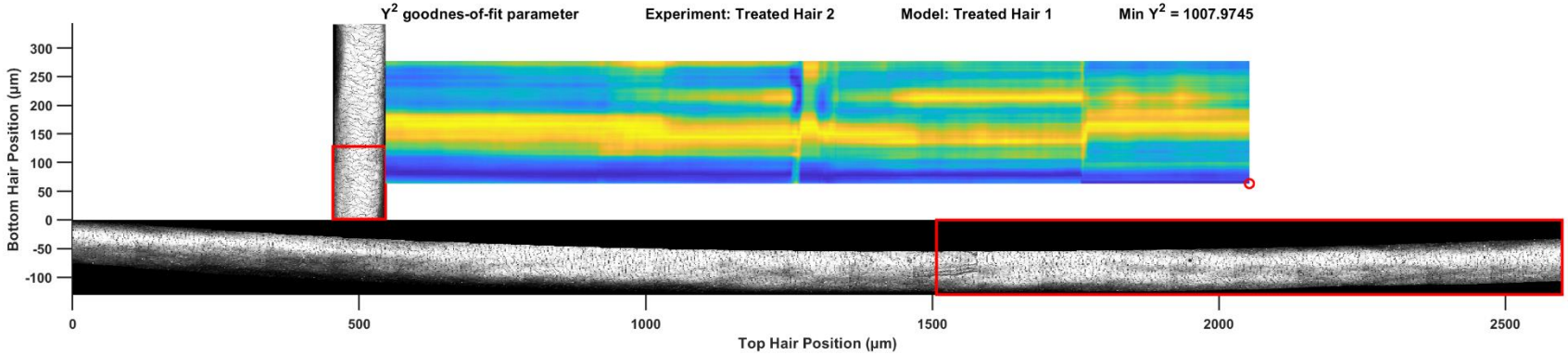

Figure 5.20 – Goodness of fit map as in Figure 5.13 but for measured adhesion forces from Treated Hair 2 and surface profilometry model from Treated Hair 1. Corresponds to the histograms in Figure 5.10H. Translation distance used for the top hair segment in the model was 25 µm.

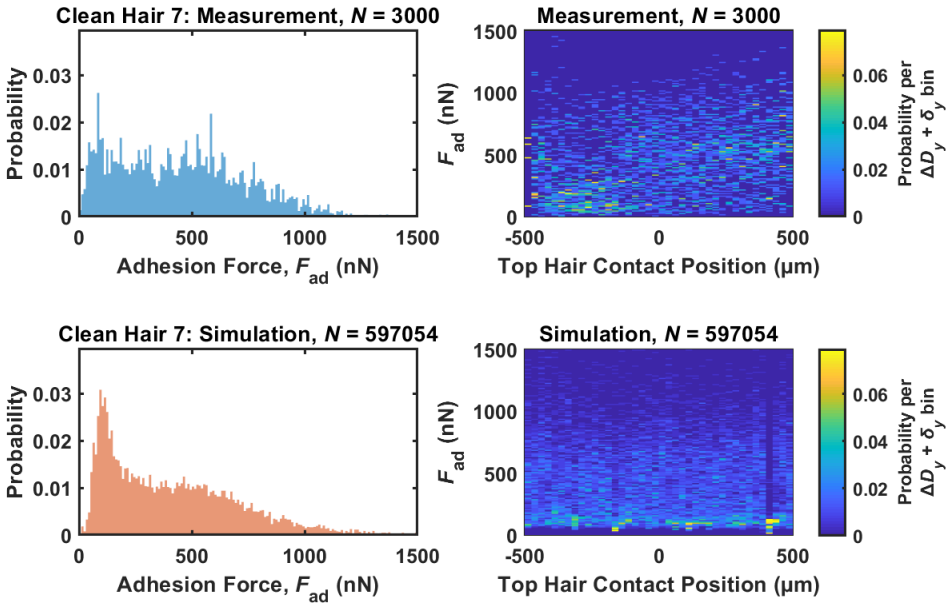

Figure 5.21 – Overall (left) and spatially resolved (right) adhesion force distributions corresponding to the measured adhesion force from Clean Hair 7 (top) and the modeled forces for Clean Hair 7 from its surface topography (bottom). The modeled forces use the sections of the top and bottom hair segments boxed in red in Figure 5.13 corresponding to the minimum Y^2 parameter. Top hair contact locations for both measured and modeled data are relative to the center of the total interval.

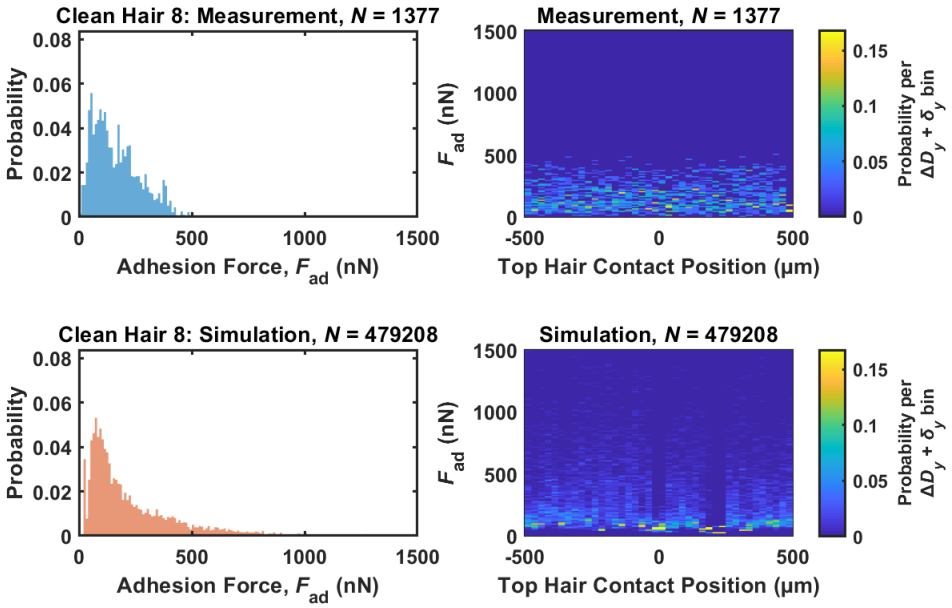

Figure 5.22 – Adhesion distributions as in Figure 5.21 but for measurements from Clean Hair 8 and modeled forces from Clean Hair 8. Modeled distributions correspond to the red boxed regions in Figure 5.14.

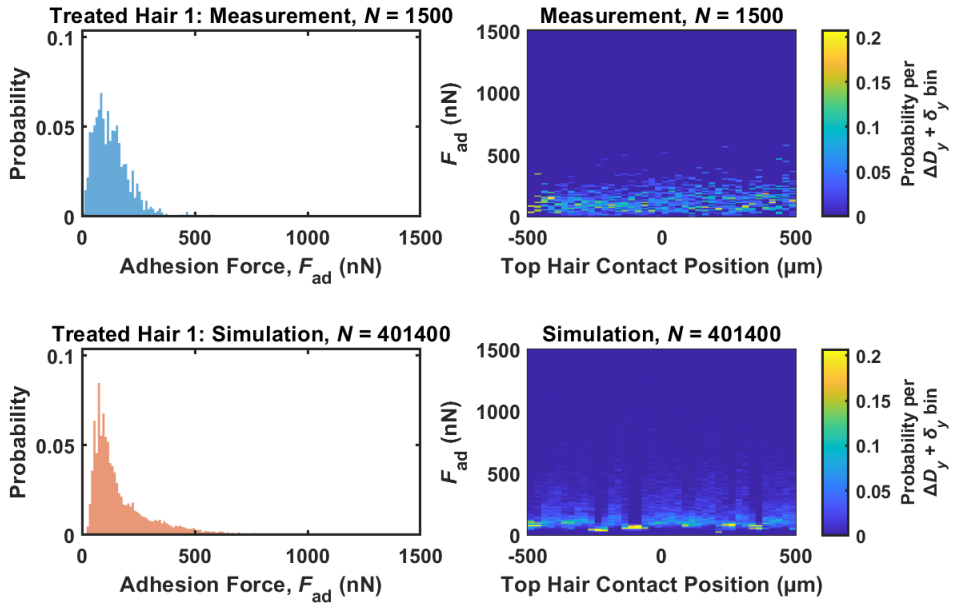

Figure 5.23 – Adhesion distributions as in Figure 5.21 but for measurements from Treated Hair 1 and modeled forces from Treated Hair 1. Modeled distributions correspond to the red boxed regions in Figure 5.15.

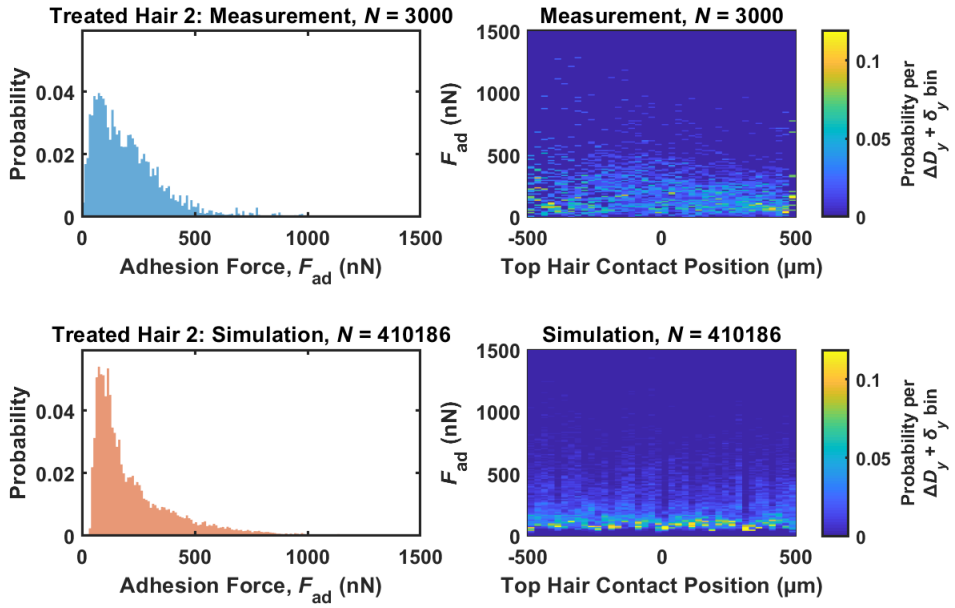

Figure 5.24 – Adhesion distributions as in Figure 5.21 but for measurements from Treated Hair 2 and modeled forces from Treated Hair 2. Modeled distributions correspond to the red boxed regions in Figure 5.16.

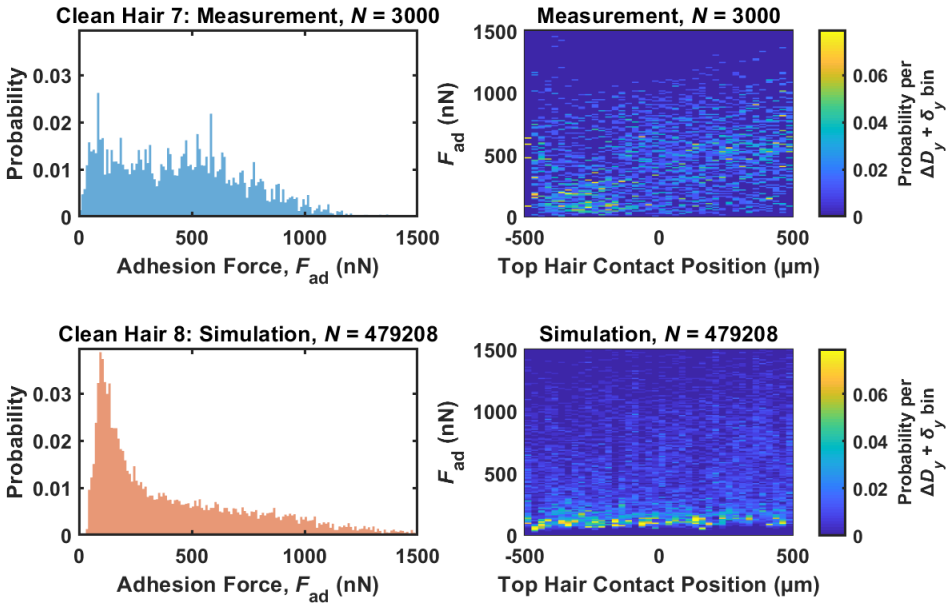

Figure 5.25 – Adhesion distributions as in Figure 5.21 but for measurements from Clean Hair 7 and modeled forces from Clean Hair 8. Modeled distributions correspond to the red boxed regions in Figure 5.17.

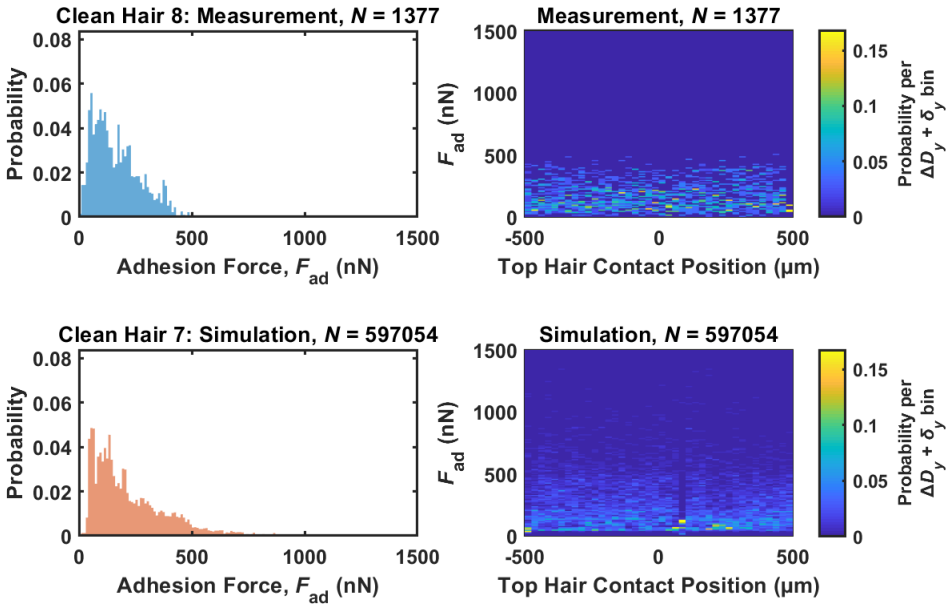

Figure 5.26 – Adhesion distributions as in Figure 5.21 but for measurements from Clean Hair 8 and modeled forces from Clean Hair 7. Modeled distributions correspond to the red boxed regions in Figure 5.18.

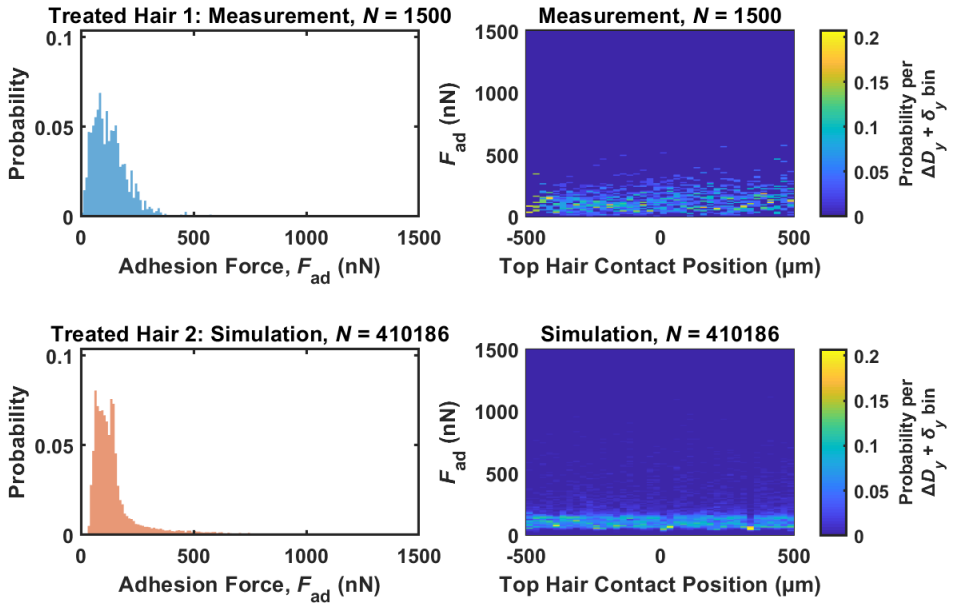

Figure 5.27 – Adhesion distributions as in Figure 5.21 but for measurements from Treated Hair 1 and modeled forces from Treated Hair 2. Modeled distributions correspond to the red boxed regions in Figure 5.19.

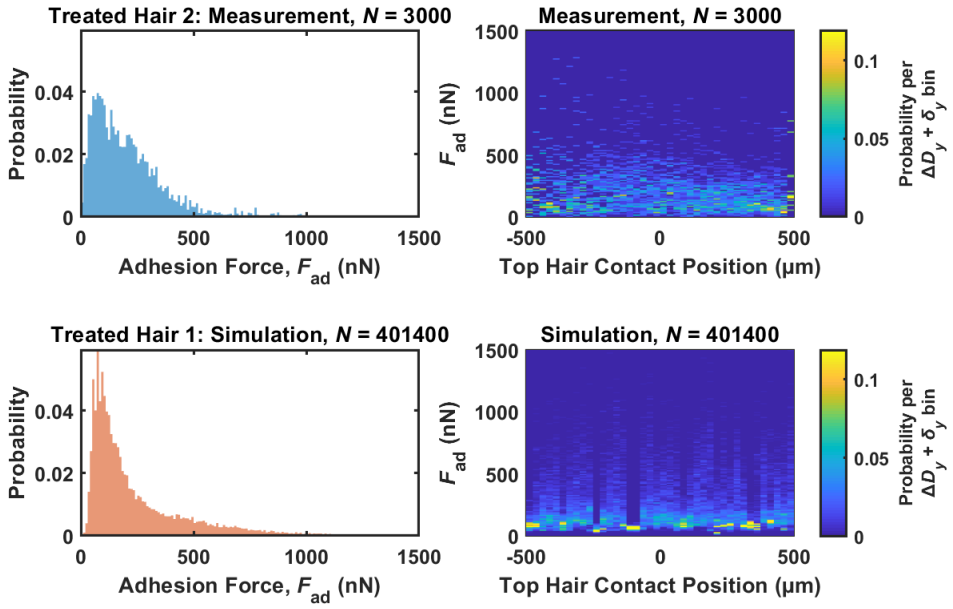

Figure 5.28 – Adhesion distributions as in Figure 5.21 but for measurements from Treated Hair 2 and modeled forces from Treated Hair 1. Modeled distributions correspond to the red boxed regions in Figure 5.20.